

NAVAL POSTGRADUATE SCHOOL

MONTEREY, CALIFORNIA

DISSERTATION

STUDY OF UNIFIED FAILURE CRITERIA

by

Stanley Defisher

December 2023

Dissertation Supervisor: Young W. Kwon

Approved for public release. Distribution is unlimited.

THIS PAGE INTENTIONALLY LEFT BLANK

REPORT DOCUMENTATION PAGE	*Form Approved OMB No. 0704-0188*

Public reporting burden for this collection of information is estimated to average 1 hour per response, including the time for reviewing instruction, searching existing data sources, gathering and maintaining the data needed, and completing and reviewing the collection of information. Send comments regarding this burden estimate or any other aspect of this collection of information, including suggestions for reducing this burden, to Washington headquarters Services, Directorate for Information Operations and Reports, 1215 Jefferson Davis Highway, Suite 1204, Arlington, VA 22202-4302, and to the Office of Management and Budget, Paperwork Reduction Project (0704-0188) Washington, DC, 20503.

1. AGENCY USE ONLY *(Leave blank)*	**2. REPORT DATE** December 2023	**3. REPORT TYPE AND DATES COVERED** Dissertation

4. TITLE AND SUBTITLE STUDY OF UNIFIED FAILURE CRITERIA	**5. FUNDING NUMBERS**
6. AUTHOR(S) Stanley Defisher	
7. PERFORMING ORGANIZATION NAME(S) AND ADDRESS(ES) Naval Postgraduate School Monterey, CA 93943-5000	**8. PERFORMING ORGANIZATION REPORT NUMBER**
9. SPONSORING / MONITORING AGENCY NAME(S) AND ADDRESS(ES) N/A	**10. SPONSORING / MONITORING AGENCY REPORT NUMBER**

11. SUPPLEMENTARY NOTES The views expressed in this thesis are those of the author and do not reflect the official policy or position of the Department of Defense or the U.S. Government.

12a. DISTRIBUTION / AVAILABILITY STATEMENT Approved for public release. Distribution is unlimited.	**12b. DISTRIBUTION CODE** A

13. ABSTRACT (maximum 200 words)

Modeling composites structures with fidelity sufficient to provide increased utility to the design community depends on a robust predictive capability that is accurate across as wide of a range of scenarios as possible. Such a model should provide an equally accurate capability to predict the failure of anisotropic composite structures as simpler isotropic ones. Additionally, the accurate prediction of failure should be possible in a variety of scenarios ranging from pri samples up to and including specimens with cracks or other stress concentrating features. Any truly satisfactory model should also span the range of strain rates and apply with equal accuracy from low-rate quasi-static strain rates near 10E-4 s^-1 up to high-rate dynamic impacts at 10^5 s^-1. As a result of their inherently complex structure, any accurate composite failure theory necessitates a multi length scale perspective. As a result, the accurate modeling and prediction of failure for heterogeneous and anisotropic composites has been, thus far, an elusive goal. The work outlined here is an attempt to unite some of the previously separate theories of failure and to extend a newly developed, more unified failure theory, to a broad range of brittle materials. Although this is intended to be particularly useful for composite materials, the enhanced accuracy of such a theory will be shown to apply equally well to homogeneous, isotropic materials as heterogeneous, anisotropic ones.

14. SUBJECT TERMS composite failure, unified failure theory, brittle failure	**15. NUMBER OF PAGES** 175
	16. PRICE CODE

17. SECURITY CLASSIFICATION OF REPORT	**18. SECURITY CLASSIFICATION OF THIS PAGE**	**19. SECURITY CLASSIFICATION OF ABSTRACT**	**20. LIMITATION OF ABSTRACT**
Unclassified	Unclassified	Unclassified	UU

NSN 7540-01-280-5500

Standard Form 298 (Rev. 2-89)
Prescribed by ANSI Std. 239-18

THIS PAGE INTENTIONALLY LEFT BLANK

Approved for public release. Distribution is unlimited.

STUDY OF UNIFIED FAILURE CRITERIA

Stanley Defisher
Civilian, Department of the Army
BSME, University of Central Florida, 2000
MSME, Stevens Institute of Technology, 2005
MS, Stevens Institute of Technology, 2010

Submitted in partial fulfillment of the
requirements for the degree of

DOCTOR OF PHILOSOPHY IN MECHANICAL ENGINEERING

from the

NAVAL POSTGRADUATE SCHOOL
December 2023

Approved by:

Young W. Kwon
Department of Mechanical
and Aerospace Engineering
Dissertation Supervisor
Dissertation Chair

Jarema M. Didoszak
Department of Mechanical
and Aerospace Engineering

Joseph P. Hooper
Department of Physics

Christopher M. Brophy
Department of Mechanical
and Aerospace Engineering

Garth V. Hobson
Department of Mechanical
and Aerospace Engineering

Approved by:

Brian S. Bingham
Chair, Department of Mechanical and Aerospace Engineering

Joseph P. Hooper
Vice Provost of Academic Affairs

THIS PAGE INTENTIONALLY LEFT BLANK

ABSTRACT

Modeling composites structures with fidelity sufficient to provide increased utility to the design community depends on a robust predictive capability that is accurate across as wide of a range of scenarios as possible. Such a model should provide an equally accurate capability to predict the failure of anisotropic composite structures as simpler isotropic ones. Additionally, the accurate prediction of failure should be possible in a variety of scenarios ranging from pri samples up to and including specimens with cracks or other stress concentrating features. Any truly satisfactory model should also span the range of strain rates and apply with equal accuracy from low-rate quasi-static strain rates near 10E-4 s^-1 up to high-rate dynamic impacts at 10^5 s^-1. As a result of their inherently complex structure, any accurate composite failure theory necessitates a multi length scale perspective. As a result, the accurate modeling and prediction of failure for heterogeneous and anisotropic composites has been, thus far, an elusive goal. The work outlined here is an attempt to unite some of the previously separate theories of failure and to extend a newly developed, more unified failure theory, to a broad range of brittle materials. Although this is intended to be particularly useful for composite materials, the enhanced accuracy of such a theory will be shown to apply equally well to homogeneous, isotropic materials as heterogeneous, anisotropic ones.

THIS PAGE INTENTIONALLY LEFT BLANK

Table of Contents

1 Background **1**

1.1 Introduction 1

1.2 Literature Review 2

1.3 Objectives 7

2 A Unified Failure Theory **9**

2.1 Failure Theories for Pristine Composites 9

2.2 Fracture Mechanics Based Failure. 13

2.3 Cohesive Zones 15

2.4 Theory of Critical Distances 16

2.5 Unified Failure Theory 21

3 Isotropic Specimens **35**

3.1 PMMA Modeling and Testing 36

3.2 Hardened Cement Paste (HCP) Modeling and Testing 44

3.3 Results 52

4 Anisotropic Specimens **55**

4.1 PLA Sample Preparation 55

4.2 PLA Test Results 64

4.3 CFC Sample Preparation 71

4.4 Modeling Setup and Methods 75

5 High Strain Rate Modeling and Testing **87**

5.1 Background 89

5.2 SHPB Test Sample Preparation 90

5.3 SHPB Test Results 93

5.4 Explosive Sample Preparation and Testing 101

5.5 Conclusions 130

6 Conclusions and Future Work **131**
6.1 Conclusions 131
6.2 Future Work 132

Appendix A Additional Contributions and Lessons Learned **137**
A.1 CFC Winding Related Issues. 137

List of References **143**

Initial Distribution List **155**

List of Figures

Figure 1.1 RVE multi-length scale model 6

Figure 2.1 Elliptical hole geometry 13

Figure 2.2 Normalized hole toughness for different theory of critical distances (TCD) methods 20

Figure 2.3 Tensile surrogate model 27

Figure 2.4 Surrogate model nodes of interest 28

Figure 2.5 Nodal stress and gradient 29

Figure 2.6 Normalized gradient without extrapolation to hole edge 32

Figure 2.7 Gradient at hole edge as a function of extrapolation technique . . 33

Figure 3.1 polymethyl methacrylate (PMMA) specimen geometry 37

Figure 3.2 Instron test machine 38

Figure 3.3 Change in PMMA stress with element count 40

Figure 3.4 Job speedup vs core count 41

Figure 3.5 6mm PMMA slot S22 stress 42

Figure 3.6 Comparison between theoretical and experimental PMMA data . 43

Figure 3.7 Half symmetric hardened cement paste (HCP) beam with mesh and boundary conditions 46

Figure 3.8 Simulated crack face in HCP 47

Figure 3.9 Node sets along HCP crack tip for stress/gradient analysis 48

Figure 3.10 Node set stress at three different positions along HCP crack . . . 49

Figure 3.11 Nodal stress gradient at three different positions along the HCP crack 50

Figure 3.12 Curve fit for the generating stress intensity factor (SIF) 51

Figure 4.1 Ultimaker unidirectional printing poly lactic acid (PLA) dogbone 56
Figure 4.2 Unidirectional PLA dogbone w/3mm hole 58
Figure 4.3 MTS testing of unidirectional PLA dogbone w/3mm hole 60
Figure 4.4 PLA dog bone model w/3mm hole and with BCs 62
Figure 4.5 PLA dogbone model with 3mm hole S22 stress distribution . . . 63
Figure 4.6 Brittle PLA tensile specimen failure 65
Figure 4.7 Typical failure initiation for a 6mm PLA hole 66
Figure 4.8 3mm PLA hole damage away from the edge of the hole 67
Figure 4.9 3mm PLA hole evolution 67
Figure 4.10 unified failure criteria (UFC) conditions for a 3mm PLA hole . . 69
Figure 4.11 UFC conditions for a 6mm PLA hole 70
Figure 4.12 Waterjet induced delamination in CFC 74
Figure 4.13 Comparison of UFC with quasi-isotropic (QI) experimental data 79
Figure 4.14 Comparison of UFC with cross ply (CP) experimental data 80
Figure 4.15 Micromechanics unit-cell model 82

Figure 5.1 Strain rate spectrum 87
Figure 5.2 SHPB schematic 89
Figure 5.3 SHPB setup with closeup sample view 91
Figure 5.4 Waterjet cut SHPB test samples 92
Figure 5.5 CFC SHPB test frames 93
Figure 5.6 SHPB raw data 94
Figure 5.7 SHPB CFC stress vs time for parallel fiber orientation 95

Figure 5.8 SHPB CFC stress vs time for perpendicular fiber orientation . . . 96
Figure 5.9 SHPB CFC strain rate vs time for parallel fiber orientation 98
Figure 5.10 Closeup of Figure 5.7 100
Figure 5.11 X-Winder 4-axis CFC filament winding machine in operation . . 103
Figure 5.12 Small diameter CFC tube 104
Figure 5.13 Large CFC cylinder experimental setup 105
Figure 5.14 Strain gauge voltage vs time (2 large CFC samples) 108
Figure 5.15 Small diameter CFC experimental set up and PDV probes 111
Figure 5.16 Three high speed video frames of explosively driven CFC 112
Figure 5.17 CFC cylinder approximately 15μs after initiation 113
Figure 5.18 Raw photonic doppler velocimetry (PDV) trace of a CFC cylinder with steel trace inset 115
Figure 5.19 Abaqus and experimental CFC wall at approximately 15 μs . . . 118
Figure 5.20 PDV and Abaqus generated velocities 119
Figure 5.21 Closeup of hypothesized failure times from Figure 5.20 120
Figure 5.22 PDV and Abaqus generated velocities 121
Figure 5.23 PDV and Abaqus strain comparison 122
Figure 5.24 CFC cylinder and ply stack plot 124
Figure 5.25 Untransformed and transformed stresses for upper PDV location . 125
Figure 5.26 Untransformed and transformed stresses for lower PDV location . 126
Figure 5.27 Experimental and theoretical failure - position comparison 128
Figure 5.28 Experimental and theoretical failure - strain comparison 129

Figure A.1 CFC winding machine mandrel end 138

Figure A.2 CFC tubes with fiber capture collar 139

List of Tables

Table 2.1 Stress gradient linear extrapolation accuracy 31

Table 2.2 Stress gradient extrapolation method 34

Table 3.1 PMMA sample geometries 36

Table 3.2 Experimentally measured properties of PMMA 38

Table 3.3 HCP properties from Karihaloo 45

Table 3.4 Theoretical and experimental failure loads 53

Table 4.1 Printed PLA tensile samples 57

Table 4.2 CFC Test specimen geometry 72

Table 4.3 DragonPlate CFC specifications 73

Table 4.4 CFC failure loads and stresses 75

Table 4.5 CP and QI CFC properties 78

Table 4.6 Unidirectional CFC sample tests 84

Table 5.1 SHPB and explosive test sample CFC properties 88

Table 5.2 Maximum stress for SHPB compression testing 97

Table 5.3 Composition C4 JWL Parameters 106

Table 5.4 Fiber failure stresses and times 127

THIS PAGE INTENTIONALLY LEFT BLANK

List of Acronyms and Abbreviations

AM	additively manufactured
CFC	carbon fiber composites
CFRC	continuous fiber reinforced composites
CFRP	carbon fiber reinforced polymers
CNC	computer numerical control
CP	cross ply
CZM	cohesive zone model
DIC	digital image correlation
DOD	Department of Defense
DOE	Department of Energy
EBW	exploding bridge wire
EPFM	elastic plastic fracture mechanics
FEM	finite element method
FDM	fused deposition modeling
FFF	fused filament fabrication
FFM	finite fracture mechanics
GFRP	graphite fiber reinforced composites
HCP	hardened cement paste
HSC	high strength concrete

HSV	high speed video
ICM	imaginary crack method
LEFM	linear elastic fracture mechanics
MKL	math kernel library
NPS	Naval Postgraduate School
PDV	photonic doppler velocimetry
PLA	poly lactic acid
PMMA	polymethyl methacrylate
PMC	polymer matrix composites
QI	quasi-isotropic
RUC	repeating unit cell
RVE	representative volume element
SHPB	split Hopkinson pressure bar
SHTB	split Hopkinson tensile bar
SIF	stress intensity factor
TCD	theory of critical distances
UFC	unified failure criteria
UMAT	user material
WWFE	World Wide Failure Exercises

Acknowledgments

I would like to thank my advisor, Dr. Young Kwon. Without his vision, persistence, and unparalleled patience, I never would have been able to complete this research. I am indebted to him for his mentorship and willingness to guide me through the process.

I would be remiss if I didn't mention my superiors and colleagues at Picatinny Arsenal, both past and present, who helped me along in various ways. Dr. Ernest Baker was not only a tremendous source of inspiration and leadership but he also motivated me to be willing to take the risk of attempting to complete this effort. Art Daniels and Steve Nicolich also supported my attendance at NPS in a number of ways and encouraged me to finish. To my colleagues Brian Peltzer, Alex Rydzewski, Sean Swaszek, Caleb Owens, Nick Lavigne, Pasquale Carlucci, Leon Moy, and Jared Einstein, all of whom either supported testing or assisted with modeling, I am also grateful.

Lastly, I couldn't have done this without the patience, encouragement, and continuous support of my loving wife Jennifer, my young son Alex, and my mother Mary. Although my mother long ago planted the seed of pursuing my education it was my wife who nurtured and supported me along the way and my young son who, although too young to understand why his father couldn't play soccer with him as often as he would have liked, tolerated it in the hopes that one day soon I would be able to join him. I recognize that my undertaking this process was not without significant discomfort to yourselves. You had faith in me that I didn't have in myself and for your sacrifice, patience, encouragement, and support, this is as much your achievement as it is mine.

THIS PAGE INTENTIONALLY LEFT BLANK

CHAPTER 1:
Background

1.1 Introduction

The reasons for using composite materials are as numerous as the different types of composites themselves. Since their inception, what makes their use so appealing is their high strength and stiffness with a surprisingly low density. These factors have contributed to making them attractive replacements for many traditional engineering materials. Their benefits are not limited to high strength to weight ratios alone however. Other aspects that make them attractive are their tailorable performance, corrosion resistance, ease of manufacturability, thermal and electrical resistance, electromagnetic transparency and dimensional stability among other factors. These materials are not perfect however, and there are some negative aspects associated with their use. Depending on their composition and geometry, they are often expensive and may suffer from degradation from ultraviolet radiation. Inspection of damage in composite structures that can lead to catastrophic failure is often impossible to conduct using traditionally employed inspection techniques such as magnetic particle testing or liquid penetration testing. Traditionally, they also suffer from poor impact resistance. Furthermore, by their very nature, they are anisotropic. While not a negative aspect of their behavior in and of itself, anisotropic behavior can prohibit their use in environments where the applied loads change directions, are alternating, or are otherwise complex. Perhaps one of the biggest problems associated with their use however, particularly with the use of the class of composites known as carbon fiber reinforced polymers (CFRP) of carbon fiber composites (CFC), is their tendency to exhibit brittle fracture. Consistently predicting the fracture of a brittle, anisotropic, heterogeneous stricture such as CFC has been a goal that has eluded researchers for quite some time.

The need to achieve higher performance composite systems requires pushing the survivability of the materials from which they are comprised. Engineering higher performance in such systems requires complicated and expensive testing and sophisticated, computationally expensive modeling. The financial costs and time necessary to conduct testing alone are prohibitive but perhaps more importantly, do not offer designers an opportunity to predict

failure outside of a relatively narrow range of geometry, loading conditions, and composite composition. As a result, consistently and accurately predicting brittle composite failure through modeling is an absolute necessity.

The mechanics of composite failure are well known and generally agreed upon at the microscopic level. Fiber failure, matrix failure, and fiber to matrix delamination are the commonly stated microscopic failure types that result from a combination of shear, tension, or compression or even one single isolated type of stress. But after three World Wide Failure Exercises (WWFE), countless papers, and theories, there is surprisingly little agreement regarding the development of a single macroscopic model for predicting composite failure, let alone one model that connects the microscopic and macroscopic perspectives. The lack of such agreement speaks to the tremendous difficulty and complexity of attempting to reach a more broadly applicable theory.

1.2 Literature Review

The three broad categories of failure theories documented in the literature include two macroscopic failure categories and one micromechanical one. One category of macroscopic failure can loosely be categorized as those that predict the failure of samples with uniform cross sections. These types of specimens, otherwise referred to as "pristine" samples are those that do not possess any features that cause local stress concentrations or gradients. The second macroscopic failure theory treats the aforementioned types of specimens where holes, notches, or cracks are present and result in high stress concentrations or gradients in the immediate vicinity of the feature. Lastly, the final category of composite failure includes micromechanical failure theories.

1.2.1 Failure in Samples with Uniform Cross Sections

Failure model for isotropic specimens without geometric variations provide reasonable agreement with experimental data over a very narrow range of loading, geometry, and strain rate. The lack of a failure model which is able to consistently predict macroscopic failure leaves designers to determine the likelihood that they are using the correct model for the given situation [1], [2]. The potential subjectivity of having to make such a choice is far less ideal than a more broadly applicable theory and leaves potential for misapplication if

the user lacks the required understanding of the most appropriate theory or the scenario of interest is not simple or straightforward. Predicting failure for these types of specimens has necessitated an appeal to a strength of materials type of approach that is well documented within the scientific literature [3]–[6]. Sun [7] et al. do an excellent job of laying out what they broadly categorize as three separate failure criterion including the limit criteria, interactive criteria, and separate mode criteria. These have been similarly categorized by a number of other researchers [8]–[14].

As Sun et al. point out, *limit criteria* approaches attempt to predict the load that will induce failure by comparing stresses in the lamina, namely σ_{11} (longitudinal stress), σ_{22} (transverse stress) and τ_{12} (shear stress), where interactions occurring between any two or more stresses, or strains, are ignored. They go on to define *interactive criteria* as those which predict the load at failure by using a single polynomial equation that includes all of the stress or strain components. And lastly, they categorize *separate mode* criteria as ones in which the failures of the fiber and matrix are treated distinctly and which may or may not depend on one or more of the aforementioned stress components. Of the three broad categories of failure models, separate mode criteria, predict the most accurate failure at the lamina level, while the limit criteria do a better job at predicting failure at the laminate level, at least for laminates that are predominately fiber dominated. This fact makes it extremely difficult for a designer to predict the failure of a CFC structure because it requires them to have a very intimate understanding of how, where, when, and why a particular failure model is accurate and when it is being used beyond its range of validity. The requirement to possess this level of knowledge is far from ideal.

1.2.2 Failure in Specimens with Stress Concentrating Features

Even when macroscopic failure of a pristine laminate sample can be accurately predicted, such a theory is, in and of itself, insufficient if it is also necessary to quantify the behavior of a similar sample with a stress localization of some sort. In other words theories which are accurate and applicable to predict failure in a pristine sample do not apply with equal accuracy to predicting failure in a specimen with a hole, notch, or crack that extends completely through its thickness. To accurately predict failure in those types of configurations, an appeal to a fracture mechanics based approach is necessary [15]–[17]. When this technique is used, one introduces other material constant parameters like fracture toughness.

Researchers working to predict failure as a result of these types of features generally take one of two paths, either the calculation of effective stress gradients in the vicinity of such features [17], [18] or the more traditional prediction of stress in the plastic zone at the crack tip [19]–[22]. Although explicit modeling of the microstructure of composite behavior and failure is still computationally prohibitive, i.e. meshing individual fibers separate from the matrix in each lamina comprising a laminate structure, previous efforts have successfully incorporated means of accounting for damage at the microstructural level. This damage is then coupled to larger length scales to predict macroscopic failure via the approach of Kwon et. al. [23]–[25].

1.2.3 Micromechanical Failure Theories

Accurately predicting composite failure at the laminate level is highly dependent on a variety of factors and features that occur at a much smaller length scale. These models are commonly referred to as *micromechanics* models since they are based on the properties of a composite microstructure [26]. As Kwon and numerous others have previously described, micromechanical failure initiates at the constituent level in CFRP and include fiber failure, matrix failure, and both inter-layer as well as fiber to matrix delamination or debonding [26]–[30]. To what extent these types of failure occur depend on a number of factors including fiber composition, size, orientation, and type as well as matrix type and the relative volume fraction among others. It is important to point out that although there have been at least some attempts to account for phenomenological behavior of sub continuum features, namely those derived from an atomistic or molecular dynamics (MD) approach [17], [27], [31] explicitly doing so is still computationally prohibitive for problem sizes that are typically of interest to designers today. To overcome the inability to explicitly model fiber bundles, individual fibers, matrix material, and small inclusions, homogenization techniques were developed.

The micromechanical level is where cracks or delamination are widely agreed to initiate and propagate through the lamina, or across them, and is heavily dependent on the mechanical and thermal properties of individual constituents and their quality. Using this technique allows a heterogeneous structure to be modeled as a homogeneous material with equivalent properties based on some knowledge or theory about the behavior of the smaller length scale components. As Barbero points out, there are a variety of homogenization schemes and they can loosely be categorized as empirical, semi-empirical, analytical, or numerical

techniques [26]. An important caveat with respect to such modeling is that as a result of the high number of fibers, fiber bundles, and numerous interfaces, pre-existing damage and porosity, failure can be highly statistical in nature and as a result, beyond the predictive capability of a deterministic code. It is important to note that no appeal has been made to using statistical methods here as necessary as that may ultimately prove to being able to more accurately predict failure.

Historically a variety of homogenization techniques have been used in an attempt to model heterogeneous behavior. The exact type of homogenization scheme used depends on a number of factors including, but not limited to, whether or not the material is periodic, i.e. its structure is consistently repeating at the micromechanical level and whether or not voids, inclusions, or damage are present and if so, to what degree. Some of the earliest techniques that fall into the aforementioned category of analytical homogenization sought to bound the problem and the pioneers Reuss and Voight assumed uniform strain or stress respectively, i.e. laminate stress or strain is the same in the fiber and matrix [26], [32]–[34]. Other techniques at bounding the solution for samples containing voids or inclusions include variational methods like that developed by Hashin and Shtrikman [35]. Often times these early models were based on the volume fractions or rule of mixtures of the physical constituents. In addition, variations of Eshelby's method by researchers such as Mori and Tanaka have also used been used successfully to account for the coalescence and interaction of inclusions in heterogeneous materials [36] where they have been understood to play an important role. Other methods based on equivalent eigenstrain [26], [37], [38] have attempted to predict failure in a similar manner. For problems exhibiting sufficient periodicity, e.g. consistent or regular composites, then Fourier series based analyses have be used to estimate the composite stiffness tensor [39]–[42].

Of particular interest for this work is the numerical homogenization method that uses the representative volume element (RVE), sometimes described as the repeating unit cell (RUC). This numerical homogenization approach has several decades of use in modeling behavior derived from the micromechanical length scale of periodic composites [7], [23], [25], [34], [43]–[45]. Figure 1.1 shows the type of volume commonly used to provide data to the macroscopic level.

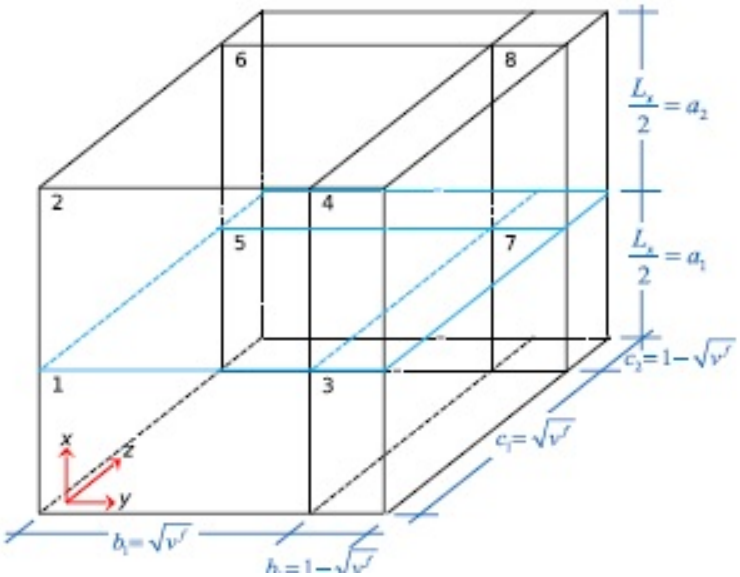


Figure 1.1. RVE for multi-length scale model Source: [25]

Although the use of an RVE does not explicitly account for micromechanical behavior, it is currently the most viable solution for incorporating input based on behavior occurring at the micromechanical level. What is novel about the use of the RVE homogenization scheme as it has been developed by previous researchers [23], [25], is that it predicts behavior at the fiber/matrix level, i.e. micro stresses and strains rather than at the macro level as is far more commonly done. This technique has recently demonstrated success at accurately predicting failure in a variety of different sample geometries [15], [46]–[48].

1.2.4 The Problem of Multiple Theories

The problems with using the aforementioned approaches to predicting failure is that one theory applies to scenarios where the uniformity of sample cross section results in no stress gradient and an entirely different theory is used when there is some feature that induces a high stress gradient. The former approach is based on the macroscopic strength of materials where failure stress is determined by whether or not a sample exceeds the tensile strength, for example, of a material over some region. The latter approach however, appeals to linear elastic fracture mechanics (LEFM) where the theoretical infinite stress that occurs in the

vicinity of a crack of infinitesimal proportions has to be assumed to be blunted in the plastic zone in order to rationalize how failure does in fact occur. Even after appealing to LEFM however, additional techniques are necessary when the crack or feature geometry veers towards a feature of finite and measurable dimensions like an elliptical or circular hole. In these types of scenarios one must appeal to the theory of critical distances in order to develop a solution that satisfactorily explains the failure. Having a different theory for each different geometry is unsatisfactory and inelegant even if within some narrow range they seem to work for distinct conditions. If however, there were a single theory which through a variation parameters could accurately predict a continuum of failure ranging from that which occurs in pristine samples to that which occurs in samples containing stress concentrating factors with high gradients then it would likely be a far simpler explanation of the phenomenology of failure. This is why we have undertaken the development and maturation of a more unified theory in this work.

1.3 Objectives

The goals of this effort are twofold. The first is to interrogate the accuracy of this newly developed phenomenological unified theory, altering where necessary, to more accurately predict composite failure. Like many of the other failure criteria currently in use, it would be desirable to be able to test a single lamina specimen of unidirectional orientation and to be able to accurately extrapolate predictions of failure to other layups with different orientations. This would appreciably minimize testing and provide accuracy beyond which is currently achievable in a much less expensive and time consuming manner. The second goal is the extension of this more unified theory so that failure may be accurately predicted over a wider range of strain rates. The hope is that this theory and approach will provide greater accuracy at predicting much higher strain rate failure of CFC than is currently possible.

THIS PAGE INTENTIONALLY LEFT BLANK

CHAPTER 2:
A Unified Failure Theory

As the use of polymer matrix composites (PMC) and continuous fiber reinforced composites (CFRC) have grown as an alternative to more traditional engineering materials, researchers have looked for a single theory that adequately describes their failure and provides the opportunity to predict when that might occur so it can be avoided. Many of the earliest composite failure theories applicable to modern PMCs trace their inception back to the early to mid 1960s to work done by Tsai and Pagano and Gol'denblat and Kopnov among others [49]–[52]. The earliest theories were analytical in nature but with the advancement and proliferation of digital computers and FEM software, their transition to computational models was an expected advancement. To understand why a new, more unified theory is of value, it is first necessary to understanding something about the existing failure theories that have been developed thus far. These theories can be categorized in three groups as follows; The first group is those that are applicable to "pristine" samples without any holes, cracks, notches, or other features which concentrate stress and/or result in a high stress gradient. The second group includes theories which accurately predict failure in samples with smooth and continuous features such as circular holes characterized by a large but finite stress localizations. The final group is one for samples containing sharp features such as low angle notches or infinitesimal cracks which are described by locally infinite stresses.

2.1 Failure Theories for Pristine Composites

The types of theories used to categorize failure in pristine composites are based on a homogenization or averaging of the constituent characteristics of composite lamina. Accounting for the behavior of the individual lamina elastic properties in addition to the fiber thickness, orientation, and ply stacking sequence is generally what is meant by "meso-scale" modeling. Although it is phenomenological in nature, since the properties at the lamina level are informed, albeit not explicitly, by the behavior and properties of the fiber and matrix one can consider these types of models as being derived from micro-scale characteristics. There is, however, another way to predict failure and the type of model that does this attempts to do so from knowledge of the constituent properties in a more bottom up type of approach. These

are known as micro-scale failure models. Although both types of models attempts to achieve accurate results through different levels of fidelity, neither the fibers nor the matrix are explicitly modeled in either technique as that is still a computationally prohibitive endeavor. The heterogeneity of composites by their very nature means that predicting failure requires a multi-length scale perspective. It is necessary to understand the limitations associated with the different length scales as each has its own associated level of complexity, computational cost, and advantages. Both meso and micro scale failure theories will be discussed.

Before proceeding, it is important to point out that there are somewhat subtle distinctions between *failure theories* and *damage models*. In general failure theories predict the initial occurrence of failure in a lamina but do not possess the capability of tracking the propagation of lamina failure that leads to more general failure of the laminate structure. Predicting the evolution of incipient failure, and the associated reduction in laminate stiffness however, is an entirely different model that has to be handled through some mechanism that provides additional parameters to account for the evolution of reduced strength that occurs as a result of cumulative damage. While damage models will not be discussed here, the different failure theories that apply to pristine samples are the limit, interactive, and separate mode criteria [7].

2.1.1 Limit Criteria

This category of composite failure theories is perhaps the simplest of their kind and builds upon a linear elastic model. The limit failure theories, sometimes referred to as noninteractive theories, are ones in which the various failure modes are predicted at the lamina level based on a comparison between the maximum stress, or strain, experienced relative to the strength of the material in a corresponding principal direction. When that directional strength is exceeded then failure is deemed to have occurred. Typically the limiting value is determined experimentally although this is not necessarily the case. An important simplification that gives this category its name is that there is no consideration of any interaction between the different elements of stress or strain. They are considered wholly on their own without any participation with the other stress components. There are a number of theories in this section including those of Prager, Stowell-Lin, and Kelly-Davies, in addition to maximum shear stress, and maximum stress and strain. In general these are all characterized by Equation 2.1;

$$\left(\frac{\sigma_i}{X_i}\right)^2 = 1 \quad \text{or} \quad \left(\frac{\epsilon_i}{X_i}\right)^2 = 1 \tag{2.1}$$

to allow for either compressive or tensile stresses. Here σ_i is the stress occurring in the i^{th} direction, ϵ_i is the strain in that direction, and X_i is simply the maximum tolerable compressive or tensile stress or strain the material can tolerate in direction i before failure occurs.

Although useful, one of the largest drawbacks of this type of theory is it is specific to a particular composition and fiber orientation. If it is necessary to predict the failure stress for a different fiber orientation and matrix, then an entirely different experiment needs to be conducted to to determine the failure stress for that orientation and composition of fiber and matrix. This is a limiting capability of this type of theory and diminishes its more general predictive capability.

2.1.2 Interactive Criteria

Unlike the simpler maximum stress and strain failure theories, the *interactive* set of criteria are ones that use some sort of polynomial equation, often in the form of a quadratic or other higher order polynomial, to predict failure. In contrast to the aforementioned failure criteria, they do so by allowing a more full interaction between the components of stress or strain. These techniques include many theories attributed to Hill, Marin, Hoffman, Tsai-Wu, and Hill-Tsai among numerous others.

The coupling of stress elements can clearly be seen in the Tsai-Wu failure criterion as stated in Equation 2.2.

$$F_1\sigma_{11} + F_2\sigma_{22} + F_{11}\sigma_{11}^2 + F_{22}\sigma_{22}^2 + 2F_{12}\sigma_{11}\sigma_{22} + F_{66}\tau_{12}^2 = 1 \tag{2.2}$$

In this theory, failure occurs when the left hand side of 2.2 reaches 1. This theory is a similar theory to Gol'denblat and Kapnov's general failure theory for anisotropic materials and is a generalization of the Tsai-Hill theory.

2.1.3 Separate Mode Criteria

Separate mode failure criterion separate the criteria for matrix and fiber failure. This separation provides somewhat of a mix between limit criteria. This is because if only a single stress component is considered, then like the limit criteria previously described, the failure direction corresponds to this stress. If there are several participating stresses, then the default is an equation wherein the strength and stress are compared and if they are determined to reach some critical value, then failure is assumed to occur.

The theories most often associated with this category are Hashin-Rotem and the Hashin criteria. The Hashin-Rotem criterion is stated in Equation 2.3.

$$\left(\frac{\sigma_{11}}{X}\right) = 1 \quad \text{and} \quad \left(\frac{\sigma_{22}}{Y}\right)^2 + \left(\frac{\tau_{12}}{S}\right)^2 = 1 \tag{2.3}$$

2.1.4 Micro-scale Failure Modeling

One similarity shared by all of the previous failure models has been that they predict failure at the lamina or laminate level. An alternative is to consider failure of the composite at the fiber and matrix level. Although the techniques of various types of micromechanical failure models differ, more or less they are all an attempt to account for sub-continuum features that are generally believed to be the primary participants involved in incipient lamina and laminate failure. Most commonly, this amounts to the prediction of stress in strain in the fiber and matrix itself.

Although not explicitly micromechanical in nature, the method of homogenization where laminate properties such as strength and failure strain are developed from experimental data might be considered a crude attempt to account for sub-continuum properties albeit implicitly. It is a useful technique owing to its simplicity although accurate prediction of the internal stresses is unlikely owing to the lack of physical fidelity.

More commonly, the technique of using RVE or RUC are what is generally meant when one thinks of micro-mechanical failure models. An RVE was used here for multi-length scale modeling using the finite element method (FEM) which is discussed in greater detail in Section 4.4.2

2.2 Fracture Mechanics Based Failure

The failure of isotropic specimens with features such as sharp notches or cracks that induce high stress concentrations is well covered in scientific literature and many modern texts on fracture mechanics [53]–[55]. It has been shown that the solution for a crack of finite width in a direction orthogonal to the loading direction and infinitesimal thickness in the direction of loading is achieved when the dimension b, shown in Figure 2.1, tends to 0. Figure 2.1 is a generalization of scenarios where the theory of sharp cracks applies to the failure of isotropic specimens and will serve as the basis for composites with the same type of feature.

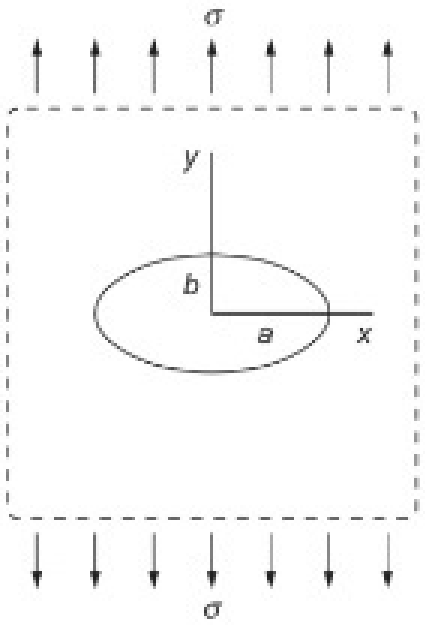


Figure 2.1. Elliptical hole geometry

When a specimen has a feature like this there is a stress singularity that occurs in the undamaged material at the crack edge. For the idealized scenario where the crack can be assumed to be elliptical in nature with a characteristic length perpendicular to the direction of loading of 2a and that in the direction of loading of 2b then the theoretical peak stress provided by the Inglis solution [56] is given by

$$\sigma_{max} = \sigma_0 \left(1 + 2\sqrt{\frac{a}{\rho}}\right) \quad \text{or} \quad K_t = \frac{\sigma_{max}}{\sigma_0} \tag{2.4}$$

where σ_0 is the nominal stress and ρ is the radius of curvature of the ellipse and is equal to $\sqrt{\frac{b^2}{a}}$. It is easy to see that as the crack length in the loading direction approaches zero, i.e. as b tends to zero, the crack tends to a straight line where the radius of curvature becomes infinitesimal. This equation is often framed with respect to the concept of a stress concentration factor K_t which is classically defined as the ratio of maximum stress, σ_{max}, to nominal stress, σ_0, and is found simply by rearranging the right hand side of the equation. As the shape of the ellipse tends to that resembling a crack, i.e. as the minor axis b becomes infinitesimal, mathematically the maximum stress tends to a physically unrealistic value of infinity. This is physically dissatisfying, however, because it is impossible even though modern prevailing theories state that the *plastic zone* ahead of the crack functions to effectively blunt the radius of curvature so that the maximum stress remains finite. It would be impossible to predict this behavior using a standard strength of materials approach because although it does a good job with estimating failure of samples that do not possess such stress concentrating features, that is not the case here. And furthermore, it is even insufficient for predicting failure in the vicinity of features like a hole that although they lack the stress singularity do have an appreciable concentration of stress at the hole edge.

Griffith [57] originally developed the concept of critical energy release rate G_c which is the rate at which energy that is liberated upon opening up new fracture surfaces. It is a type of reaction balancing step that states if the energy supplied to a crack tip does not surpass the amount of energy that is dissipated as a result of the formation of new surfaces, then the crack will not propagate. Conversely if some *critical* energy is surpassed then crack propagation does in fact occur. Later Irwin [58] developed the stress intensity factor K_{1C} in mode 1 opening, not to be confused with the stress concentration factor K_t discussed previously. This situation occurs when a crack propagates in a direction perpendicular to the axis of loading and provides a means of comparing the critical energy release rate and the stress intensity factor. This relationship is shown in Equation 2.5.

$$G_c = \frac{K_I^2}{E} \quad \text{and} \quad K_I = \sigma\sqrt{\pi a} \tag{2.5}$$

Here E is Young's modulus, σ is the applied load and a is half of the crack length. The form of the latter equation is appealing because as the crack length grows, i.e. as a gets larger, our intuition says that it should become easier to completely fracture the specimen. This clearly shows up as an increase in the stress intensity at the crack tip as expected. The form of this equation changes slightly based on whether the loading experienced is tensile or compressive but regardless of the nature of the load, the general form remains the same.

Although the theory of LEFM is incredibly useful, it does suffer from a few shortcomings. First, it is unable to predict failure in a specimen with a geometric feature that does not resemble a sharp crack or if, in fact, it has no crack at all. So if the analysis of a blunt notched specimen or smooth circular hole is necessary, a user must appeal to a different methodology than those offered by LEFM. In addition, the stress singularity itself is clearly a physically unrealistic solution. Any material would fail well before reaching an infinite value so although this is the end result of the mathematics of the problem as posed, it is not a physically realizable value and thus to the extent that it is a solution, is unrealistic. In order to overcome the shortcoming of LEFM in dealing with blunt notches, the concept of cohesive zones or the cohesive zone model was developed.

2.3 Cohesive Zones

This alternative phenomenological model, developed separately during the 1960s by D.S. Dugdale and G.I. Barenblatt, is also a method used to simulate cracks and to overcome the shortcomings of LEFM [59]–[61]. It can be considered a more general model that in some sense, is capable of accurately describing a wide range of behaviors including cracking in pristine or uncracked structures as well as blunt notches and sharp cracks in addition to interface delamination in composite laminae. This is in contrast to the previous method of LEFM which, as mentioned, breaks down when attempting to predict the behavior of materials with blunted features that resemble notches more so than cracks [62]–[64]. Although the precise details of the method vary with the implementation, in general the cohesive zone model (CZM) centers around the use of what is commonly called a traction-separation constitutive equation or often, simply a constitutive equation. These relationships which govern the interaction of cohesive elements are based on different bases including both potential based as well as nonpotential based interaction models. Although the CZM

is not subjected to some of the limitations of other LEFM methods, the accuracy of the result is highly dependent upon the user's choice of the traction-separation model and its more general basis. This method has been used quite accurately with the appropriate choice of model, but as an ancillary focus of this effort was the development of a more general unified failure criteria (UFC), this technique was avoided in the interest of developing a model agnostic of any user chosen constitutive equations and their subsequent potential for failure.

2.4 Theory of Critical Distances

The theory of critical distances (TCD) is the name given to a broad grouping of theories that can be used for both fatigue and fracture prediction [17], [18], [65]–[67]. Although originally developed to predict fatigue failure in metals, it has also been shown to accurately predict failure in ceramics and polymers [68]. In all of these types of materials it provides an alternative method to predict brittle failure in the vicinity of a stress concentration. It does so by considering the material in the immediate vicinity of a crack rather than simply at the crack tip where the stress may be, at least theoretically, infinite. The idea, similar to the limit criteria discussed previously for predicting failure in otherwise pristine samples, suggests that failure occurs when the maximum value of stress or strain reaches a critical value. Unlike the limit criteria discussed previously, of importance to TCD is a *location* where the limiting stress is reached. This method includes a variety of techniques to predict where that critical value occurs. The different subcategories of TCD include the point, line, area or volume that surround the crack tip. The benefit of this methodology is that it limits the infinite stress (the point at which this occurs is commonly referred to as the "hot spot") which results from an appeal to the method of fracture mechanics as predicted by Inglis' solution.

TCD requires that some length scale L, the nominal fracture stress, which varies as a function of crack length a, equals the critical stress at which failure occurs. This length scale is shown in Equation 2.6.

$$L = \frac{1}{\pi}\left(\frac{K_c}{\sigma_u}\right)^2 \tag{2.6}$$

Here K_c is the fracture toughness and σ_c is ultimate tensile strength. Two of the methods previously mentioned, namely the point and the line method, are based on the stress while the remaining two are based on the stress intensity. There are others including the area and volume method which similarly average stress over an area or volume, respectively, in the vicinity of the crack, but those will not be discussed here as they are essentially extensions of the point or line methods. It is important to note that as previously pointed out, since TCD is applicable to both fatigue and fracture, any user must ensure the right parameters are chosen based on the nature of their problem. The methods are described individually below.

2.4.1 The Point Method

The Point Method (PM) was the first method used under the theory of critical distances and is the simplest of all of the TCD categories. It is based on an assumption of linear elasticity and assumes that rate independent failure occurs when the stress σ equals a critical value σ_c at a distance $\frac{L_0}{2}$ from the root of the notch. For a circular hole subject to uniaxial tension the polar equation shown in Equation 2.7, shows the relationship between stress and critical stress as a function of a specific distance and angle.

$$\sigma = \sigma_c \left(r_c = \frac{L_0}{2}, \theta = 0 \right) \tag{2.7}$$

More generally however, this simply states that at the distance $\frac{L}{2}$ from the root of any notch, failure occurs when the stress σ is equal to some critical value σ_c as shown in Equation 2.8.

$$\sigma \left(\frac{L}{2} \right) = \sigma_c \tag{2.8}$$

As long as the elastic stress field in the immediate vicinity of whatever the stress concentrating factor is then this technique can be utilized. This type of information is readily available from any FEM software so this straightforward and simple procedure lends itself to coupling with any modern computational analysis tool.

2.4.2 The Line Method

This TCD method is only slightly more complicated than the Point Method discussed previously. It is stated, here without proof, in polar coordinates, as Equation 2.9.

$$\sigma_c = \frac{1}{d} \int_0^d \sigma_r(r, \theta = 0)\, dr \tag{2.9}$$

The value of d is given by Equation 2.10.

$$d = \frac{2}{\pi} \left(\frac{K_c}{\sigma_0} \right)^2 \tag{2.10}$$

Since d is simply $2L$ and we know that the region of interest lies along the line $\theta = 0$, this simply an equation which averages stress along a line originating from the root of the notch or crack and can be stated more succinctly in Equation 2.11.

$$\sigma_c = \frac{1}{2L} \int_0^{2L} \sigma_r\, dr \tag{2.11}$$

This is in contrast to the point method discussed previously where failure was stated to occur at a distance of $\frac{L}{2}$. Comparing Equation 2.8 with Equation 2.11 it can be shown that both of these methods predict the same answer assuming the crack length is long. If it is short however, then there is no guarantee that the two answers given by these different formula will be equal. It is stated without proof that although this may be the case, the differences are almost always so small that either is an adequate method for predicting failure away from the notch root.

2.4.3 Imaginary Crack Method

Unlike the two previous approaches that were based on stress, the imaginary crack method (ICM) is based on the concept of stress intensity factor K_c and is born of they types of approaches used in standard fracture mechanics theory. In this theory an unreal or "imaginary" crack is postulated to exist and starts at the root of the actual crack or notch. When the stress intensity of the imaginary crack reaches the value of K_c then failure is

predicted to occur. When the characteristic length again equals L away from the crack root then failure occurs. This theory was attractive because it avoided the shortcoming of another of Taylor's TCD methods, the 'introduced crack method' wherein the theory could not be used if the length of the crack was on the order of magnitude of the distance L [69].

The variable L cannot be known before hand but rather must be determined experimentally. Whether or not there is any physical significance to the value of L depends entirely on the problem size but generally for composites, there does not seem to be any correlation to any physical property [19].

2.4.4 Finite Fracture Mechanics Method

This method is the newest of the aforementioned subset of TCD methods. Like the ICM it too is based on stress intensity vice stress [17], [67]–[70]. It is similar to the method developed by Griffith wherein he stated that a crack tends to propagate when potential energy, which is reduced as a result of crack growth, is greater than or equal to the increase in surface energy that results from the generation of new free surfaces. Like that method, the finite fracture mechanics (FFM) is also applicable to elastic materials that exhibit brittle fracture. The Griffith fracture criterion states that the brittle fracture strength σ_f is described by Equation 2.12.

$$\sigma_f = \sqrt{\frac{G_c E}{\pi a}} \tag{2.12}$$

The TCD FFM method states this in slightly different form.

$$\sigma_f = \sqrt{\frac{G_c E}{\pi \left(a + \frac{\Delta a}{2}\right)}} \tag{2.13}$$

In this method the relationship between stress intensity K_c and the characteristic length L is given by Equation 2.14.

$$\int_0^{2L} K^2 \, da = K_c^2 * 2L \tag{2.14}$$

Here, da is the change in crack length and, like the line method discussed previously, the correct length scale of the distance from the crack root at which failure occurs is $2L$.

This is similar to the integral of the critical energy release rate shown in Equation 2.15.

$$\int_0^{2L} G \, da = G_c * 2L \tag{2.15}$$

Regardless of the exact method of TCD used, they are all in reasonable agreement with one another. Figure 2.2 from Taylor [71] shows the general agreement for normalized toughness for a sample containing a long thin notch as a function of the radius of the notch root.

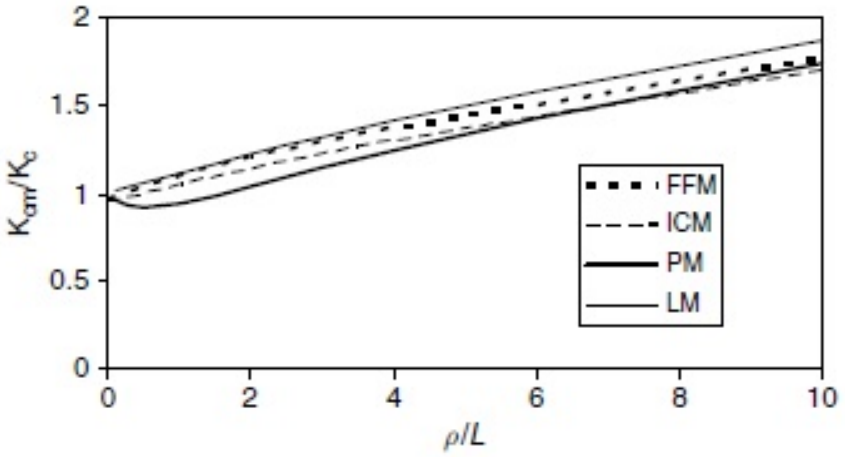


Figure 2.2. Normalized toughness for different TCD methods Source: [71]

As a result of such little difference, the choice of which method to use is left up to the reader and may vary with the circumstances.

As useful as the various formulations of TCD are for predicting brittle failure however,

their use is not without shortcomings. The first shortcoming this group of theories suffer from is that they only applies to specimens that have a notch that generates a stress gradient of sufficient magnitude and not what have been previously categorized here as "pristine" samples. That is problematic in that not all geometries of interest possess stress concentrating features so this effectively excludes the user from predicting the failure of an entire class of problems, i.e. undamaged specimens, based on nothing more than an overly restrictive range of applicability owing to how TCD was developed. Even when there is a crack that induces a high stress gradient however, the various instantiations of TCD require some knowledge of the crack length a be known and that the stress that induces failure is less than the maximum stress that occurs at some critical distance from the notch. Often times it is difficult, if not impossible, to know something more about the stress and subsequent critical distance, particularly under the case of combined loading. Although these theories may be accurate within a narrow range of specimen parameters, they are not motivated by phenomenological arguments nor can you reach an accurate conclusion of why the stress and length are chosen based on the fundamental mechanics of failure. For these reasons, researchers looked for a more capable and broadly applicable theory to be used for the prediction of the failure of brittle materials.

2.5 Unified Failure Theory

Although the micromechanical approach for predicting failure should be more accurate owing to the fact that this is the length scale where initial failure is believed to occur, the use of homogenization or laminate modeling schemes that predict more global macroscopic failure are traditionally used to predict global composite failure.

For the scenario where the central feature is elliptical hole in a plate subjected to uniaxial tension, the general expression for the peak stress that occurs at the edge of the hole is given by Inglis' solution [56] and is of the form

$$\sigma_{max} = \sigma_0 \left(1 + 2\frac{a}{b}\right) \tag{2.16}$$

where the value of a is half the length of the major axis and the value of b is half of the value of the minor axis. In the special case where the major and minor axes are identical,

this reduces to the well known solution where the maximum stress equals $3\sigma_0$ where σ_0 is the nominal stress or the stress that occurs far away from the stress concentration. For the scenario where the major and minor axes are not identical, the situation is much different. In this case, as the length of the major axis grows and the length of the minor axis shrinks, the ellipse more closely resembles a crack rather than an ellipse and again, as predicted albeit by the theory of fracture mechanics discussed in Section 2.2, the stress at the edge of the hole tends to infinity.

For the case of a circular hole however, the value of stress in the vicinity of this geometric feature is given by Kirsch's solution, the most general form of which is given in Equation 2.17.

$$\sigma_r = \frac{\sigma_0}{2}\left(\left(1 - \left(\frac{a}{r}\right)^2\right) + \left(1 + \frac{3a^4}{r^4} - \frac{4a^2}{r^2}\right) cos(2\theta)\right) \tag{2.17}$$

Here σ_r is the stress in the radial direction and θ ranges from 0° in the direction of loading to 90° perpendicular to the direction of loading. At 90° this equation defaults to the well known solution where σ_{max} is equal to $3\sigma_0$ at the edge of the hole.

Clearly the solutions for elliptical and circular holes are different from each other but in addition, their accurate use requires entirely different theories developed from fracture mechanics and idealized scenarios (e.g. infinite plates). Not only do these theories apply only to very specific geometric features, but they do so within very narrow ranges of loading conditions as well. To accurately predict the maximum stress resulting from biaxial or combined loading scenarios would necessitate the alteration of these theories in order to accurately predict failure. That is unsatisfactory from the perspective that it requires not only a relatively simple loading case but a priori knowledge from anyone attempting to determine when failure occurs. A more satisfying theory would default to the various scenarios without requiring a user to understand before hand that the geometric and loading conditions are close enough to those for which idealized solutions have previously been generated. It is for this reason that this work was initially undertaken.

This work builds on a previous multi-length scale approach developed by Kwon et al [23], [24], [46], [72] and it incorporates a new, two-part, failure theory that is believed to more

accurately predict composite failure. It was done in an attempt to extend the predictive capability of a single solution methodology to a more broad class of problems. This new, more "unified" theory merges two approaches to make it more accurate at predicting failure over a more diverse set of sample types. One part of the theory incorporates a strength of materials approach that accurately predicts failure in pristine, brittle, samples while the other one was developed from fracture mechanics to make the prediction of failure possible for samples with geometric features that cause high stress gradients or stress singularities. Both parts of this new, unified theory must be satisfied if failure is to be assessed to occur. Although this unified theory is phenomenological, because it is built on a multi-length scale approach using RVEs it also incorporates as much of the information from the micro length scale as is practical, including the prediction of failure at the micro-scale vice macroscopic failure as is most commonly predicted by composite failure models. The two parts of this theory, which hereafter will be referred to as the UFC, are described by Equations 2.18 and 2.19.

$$\sigma_{eff} \geq \sigma_{fail} \tag{2.18}$$

and

$$\sigma_{eff} \geq \left(2E \left| \frac{d\sigma_{eff}}{ds} \right| \kappa_{fail}\right)^{\frac{1}{3}} \tag{2.19}$$

Equation 2.18 simply states that whatever the maximum relevant stress is, it needs to be greater than or equal to the failure strength of the tensile test specimen derived failure stress while 2.19 states that in order for failure to occur, the maximum effective stress needs to be greater than the product contained in parenthesis. The product in parenthesis consists of E, Young's modulus, the gradient $\frac{d\sigma_{eff}}{ds}$, i.e. the change in stress in the direction of failure, and lastly the parameter κ_{fail}. The latter value is a material property proportional to the fracture toughness and critical energy release rate with the dimensions of $Pressure \cdot length$ the units of which are $Pa \cdot m$. The first criterion speaks to the failure location of a specimen while the second speaks to the path or direction along which failure occurs.

To determine the quality of agreement between the newly developed unified theory and experimental and modeling results, a simple material was chosen for initial efforts. Using a

material free from the complications of heterogeneities and anisotropy allowed us to interrogate the failure of samples tested in a simplified manner to what would be required for testing heterogeneous composites like graphite fiber reinforced composites (GFRP) or CFRP. For the initial experimentation, because the material was inexpensive, readily available, and easily machined, the transparent, thermoplastic polymer, polymethyl methacrylate (PMMA) was chosen as a baseline.

2.5.1 Stress Gradient Analysis

While not a failure theory in and of itself, in order to interrogate the accuracy of the newly developed unified failure model, it was first necessary to be able to accurately compute the stress gradient. The necessity of measuring the stress gradient is easily seen by examining the right hand side of Equation 2.19, the second of the two unified failure theory equations. The mathematical analysis associated with pristine samples is more straight forward. This is easily understood when looking at Equation 2.18. In the case where the test specimen lacks any features such as a hole or crack, the stress is uniform and the stress gradient is zero. In this case it is impossible for σ_{eff} to not be greater than σ_{fail} after the failure stress is exceeded so Equation 2.3 is the dominant equation of the two since Equation 2.4 is always satisfied and no calculation of the stress gradient was necessary.

The case where there is a stress concentration is however, far more interesting as Equation 2.19 was the driving scenario. As a result, it was necessary to computationally determine the stress gradient $d\sigma_{eff}/ds$. In this scenario both the stress and the gradient were needed but the location of the stress gradient, as per the previous discussion, meant that it had to be calculated in the vicinity of whatever features was inducing a high stress gradient. For the purpose of testing this theory, circular holes were not only easily manufactured for testing, but they were easily modeled with gradients that occurred in consistent and easily determined directions. The values of the stress were readily available and were interrogated using the FEM program Abaqus to model uniaxial test specimens of varying composition. The subsequent results were analyzed using Matlab to generate the stress gradient. Fortunately there is a canonical problem of a hole in an isotropic plate that gives us a path forward with respect to the solution.

The theoretical solution for the stress around a finite hole in an infinite plate is a well

documented problem [73]–[75]. This solution, often dubbed as "Kirsch's problem" provides a closed form analytical solution for the stress at the edge of the hole in both the r and θ directions of the form

$$\sigma_r = \frac{\sigma_0}{2}\left(\left(1 - \frac{a}{r^2}\right) + \left(1 + \frac{3a^4}{r^4} - \frac{4a^2}{r^2}cos(2\theta)\right)\right) \tag{2.20}$$

and

$$\sigma_\theta = \frac{\sigma_0}{2}\left(\left(1 + \frac{a}{r^2}\right) + \left(1 + \frac{3a^4}{r^4}cos(2\theta)\right)\right) \tag{2.21}$$

At the edge of the hole perpendicular to the loading direction, when $a = R$ and $\theta = 0$ radians this 2.20 reduces to

$$\sigma_{\theta=0} = \frac{1}{2}\left(1 + \frac{R}{r^2}\right) + \left(1 + \frac{3R^4}{r^4}\right) \tag{2.22}$$

If this expression for σ is then differentiated with respect to r it yields

$$\left|\frac{\partial\sigma}{\partial r}(r = R)\right| = \frac{7}{R} \tag{2.23}$$

Upon rearranging 2.18 to be of the form

$$\frac{\sigma^3}{2E}\left|\frac{d\sigma}{ds}^{-1}\right| \geq \kappa_{fail} \tag{2.24}$$

where κ_{fail} is the material parameter discussed previously, we see that the beginning of failure is governed by an equation of the form $\sigma \propto R^{\frac{-1}{3}}$ [15].

The theory predicts that the maximum stress $\sigma_{\theta,max} = 3\sigma_0$. When the concept of stress concentrations are introduced, it is important to understand that they are used to compare numerical solutions to those predicted by theory. This θ_{max} will be calculated using FEM and

compared to theory. The concept of stress concentration is commonly used when discussing stress in the vicinity of geometric features or irregularities. In general, this can be reduced to an equation of the form

$$k = \frac{peakstress}{nominalstress} \tag{2.25}$$

where k is known as the stress concentration factor and the peak stress is that experienced at the edge of the hole and the nominal stress is that which the sample experiences at a distance sufficiently removed from the stress concentrating feature.

Although this solution is theoretical and ideal, i.e. it applies to an infinite, homogeneous, isotropic plate, the process can still be applied for conditions that are close enough to ideal. There are however, some subtleties that apply depending on whether the sample is finite and/or a composite laminate. Those details will be discussed in later relevant sections.

The application of FEM was critical to being able to generate the stress gradient for the various scenarios of interest. The FEM tool used for all analyses was Dassault Systèmes Abaqus ® Complete Abaqus Environment (CAE) standard solver. Except where noted the standard, i.e. implicit, solver was used owing to the generally low strain rate at which the scenarios of interest were tested. Where possible, quarter symmetric conditions were used but when this was not the case, a full model that was not reduced to take advantage of symmetry planes was used. The models were small enough that the additional computation time this required was brief.

In order to generate a model for the purpose of comparing the unified theory with the infinite plate theoretical scenario discussed previously, a surrogate model had to be created. Any model had to be large enough to minimize deviations from the infinite scenario. A 60cm x 60cm PMMA plate with a 1mm hole in the center was determined to be sufficiently large, i.e. with a diameter to edge ratio of .0167, so that variations between this less than infinite plate would be minimal when compared to the theoretical, but impossible to model, infinite plate solution. The model with boundary conditions and load is shown in Figure 2.3.

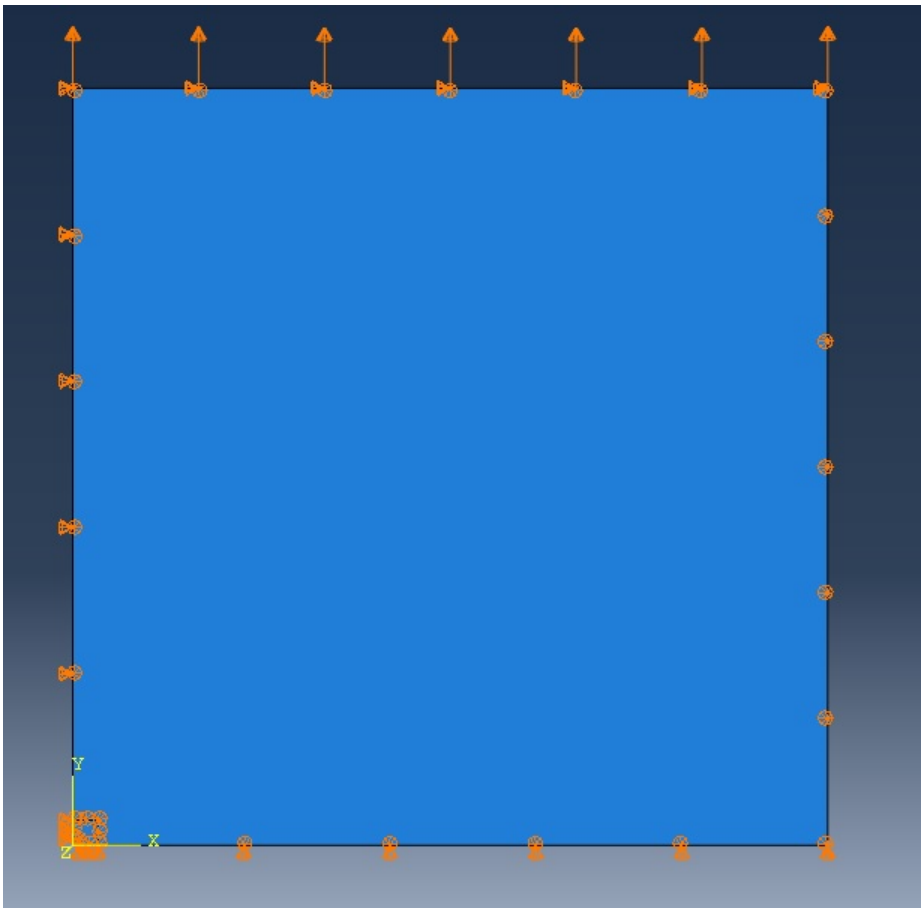


Figure 2.3. Tensile surrogate model w/.5mm radius hole in the lower left hand corner

Owing to the symmetry of the problem, a quarter symmetric plate with a hole in the lower left corner was sufficient to balance computational efficiency with solution accuracy. For this model, zero displacement was applied in the y direction along the bottom edge, a zero x displacement along the left edge, and a zero z displacement along the entirety of the plate was created. A 1mm displacement was applied along the top edge of the model and the elastic properties outlined in Table 3.2 were applied. A display group was created from these results for a small subset of nodes along the bottom edge of the test specimen in the vicinity of the stress concentrating feature and were then used to tabulate stress values. The stresses at these nodes were then plotted via Matlab as shown in Figure 2.4.

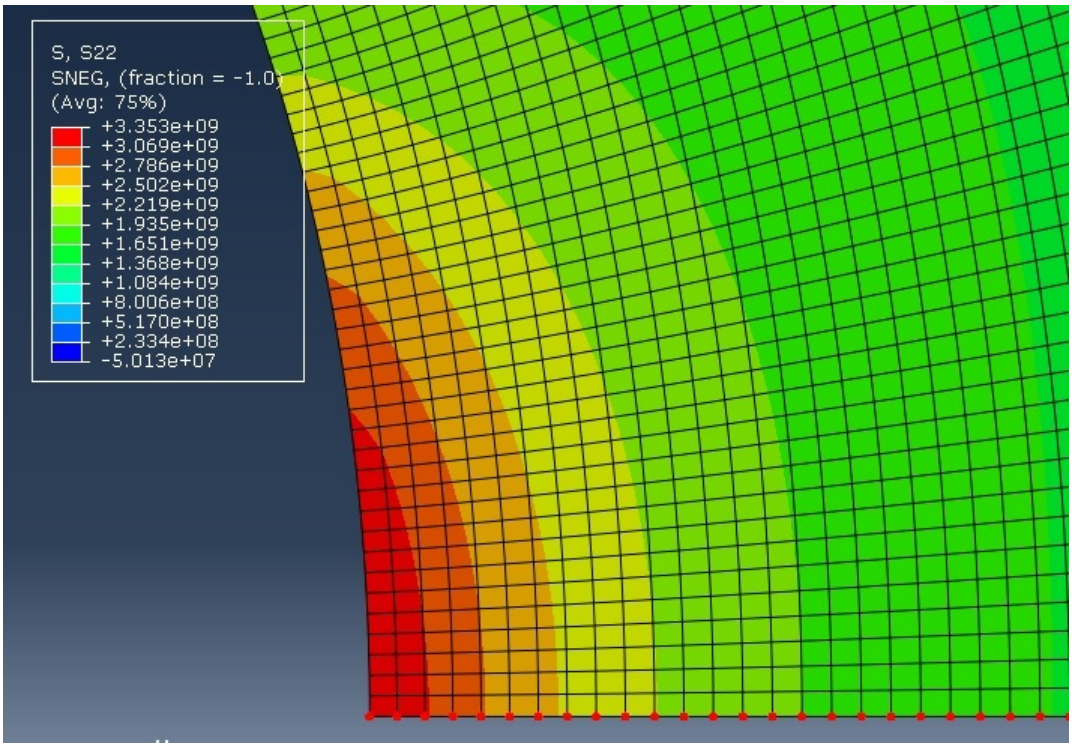


Figure 2.4. Infinite surrogate model nodes at the stress concentration

Based on previous modeling experience and the rapidly changing nature of the gradient in the vicinity of the hole, a swept mesh with a directional bias was initially applied to the geometry in the vicinity of the hole. Ordinarily, a higher number of elements in the vicinity of the hole would generate the most accurate solution for the stress occurring at the hole edge with only a minimal computational cost. Because the numerical method used to calculate the gradient turned out to be so sensitive to even slight mesh inconsistencies however, using a biased mesh made the accurate measurement of the gradient more difficult. After this was discovered, the mesh bias was removed but the swept mesh method was retained as it allowed the generation of a much more consistent and controllable mesh in the vicinity of the hole. A number of different shell elements were used for this modeling owing to their accuracy in simulating a scenario where the specimen thickness is so small relative to the other dimensions but we found that the 4 noded, reduced integration elements provide a more accurate solution than their 8 noded analogues. Plots of nodal stress and the corresponding stress gradient are shown on the same plot in Figure 2.5.

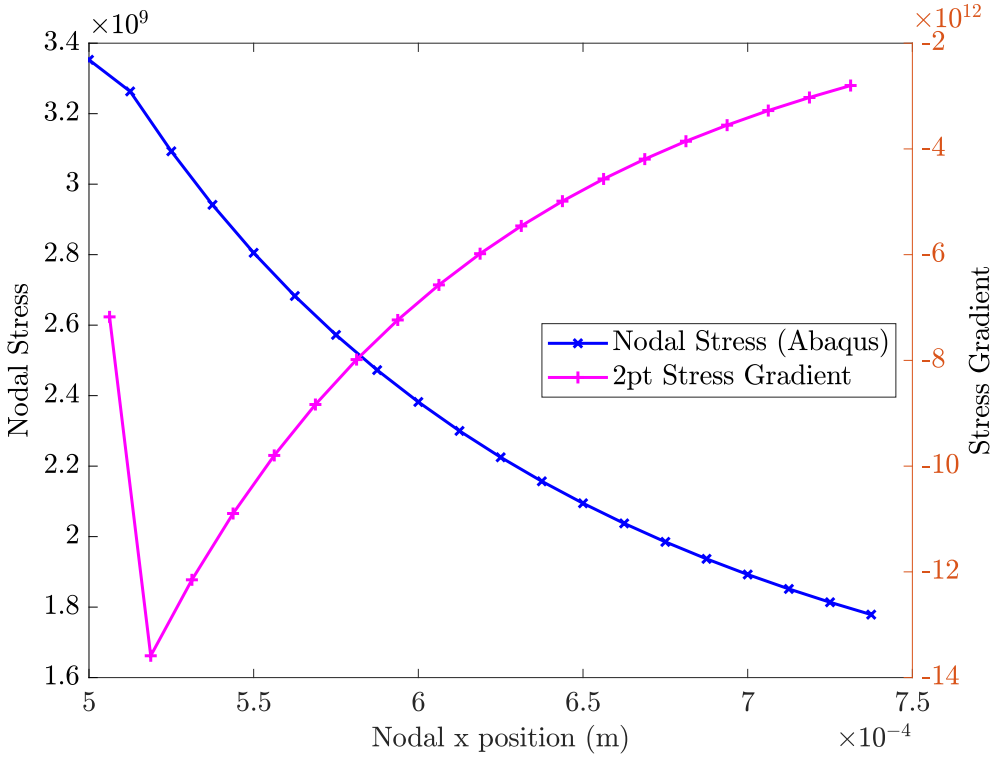


Figure 2.5. Stress and gradient near a 1.0mm hole

Matlab was used to conduct a simple numerical differentiation, initially using a three point differentiation formulation. Upon subsequent analyses however, a two point integration scheme was found to produce smoother behavior of a strictly increasing monotonic nature. As a result, this two point differentiation scheme was used for all calculations. Perhaps most importantly, the function was written so that a variable number of points could be discarded in the interest of determining where the gradient would agree most accurately with theoretical solutions. This was done because of the sensitivity of the numerical differentiation technique to slight changes in initial data and the subsequent effect that slightly varying initial numerical data had on the prediction of stress when extrapolated back to the hole edge.

The stress gradient was then calculated using a simple two point method based on the value

of stress at the node ahead of and at the point of interest in a straightforward manner given by Equation 2.26.

$$\frac{d\sigma}{dx} = \frac{\sigma_{i+1} - \sigma_i}{x_{i+1} - x_i} \tag{2.26}$$

Here, σ_{i+1} is the stress at node $i + 1$ and x_{i+1} is the x coordinate of the corresponding node and the i values were calculated similarly. It should be noted that both a two point as well as a three point method were employed but the two point method was found to produce the most accurate results, i.e. results that were closer to the theoretical predictions given by Equation 2.22 for a infinite, isotropic, plate.

Although this provides a mechanism to calculate the stress gradient, its value is calculated at the $x_i th$ point that lies between the two x values used in Equation 2.25. As a result, in order to determine the value of the gradient at the edge of the hole where it is most of interest, the stress gradient had to be extrapolated back to the hole edge in some manner. The simplest way to do that was via a linear extrapolation back to the hole edge from the closest point in the stress gradient. In Figure 2.5 it is clear that the locations at which the stress gradient are calculated lie between the nodal locations where stress was calculated and subsequently plotted. At this point the stress gradient was normalized by the maximum edge stress using Equation 2.23.

From Equation 2.23 we can see that the absolute value of the stress gradient at the hole edge should have been 14000 $\frac{N}{m^3}$ for a 1mm hole diameter. When this value was normalized by the maximum hole stress, a value predicted by theory to be $3\sigma_0$, a value of around 4667 $\frac{N}{m^3}$ should have resulted.

As mentioned previously, calculation of the stress gradient via the chosen two point numerical differentiation scheme was sensitive to the chosen element type. Both 4 noded and 8 noded shell elements were used to predict the stress and stress gradient. Using higher order elements while controlling the number of elements in the mesh in the immediate vicinity of the geometric feature resulted in less smooth gradient calculations. As a result, only 4 noded elements were used for all subsequent analyses. There was an optimal mesh resolution where the finest mesh produced the most accurate value for the stress concentration factor

but resulted in the most erratic stress gradient values. To assure that we were operating in the vicinity of this optimal region, several mesh densities were run for each calculation with an intermediate mesh density used for the calculation of the stress gradient. Differences between theoretical and experimental values were easily determined as a function of mesh size as seen in Table 2.1.

Table 2.1. Stress gradient linear extrapolation accuracy

Mesh Resolution	Theoretical Value	Predicted Value	Percent Difference
Low	4667	4411	5.48
Medium	4667	4655	.25
High	4667	4695	-.60

After controlling the type and number of elements in the vicinity of the hole, it was clear that the number of points of the gradient that were ignored had an appreciable effect of the predicted stress gradient at the hole edge. This resulted in a stress gradient value of -2105 $\frac{N}{m^3}$ near the edge of the hole. This was clearly headed in the opposite direction of the theoretical value so the decision was made to discard a variable number of initial points in determine if better agreement with the theoretical value was possible given a fewer number of initial points. This was believed to be necessary due to the sensitivity that numerical differentiation has and the subsequent unexpected behavior seen in the gradient nearest to the hole. An example of this can be seen in Figure 2.6.

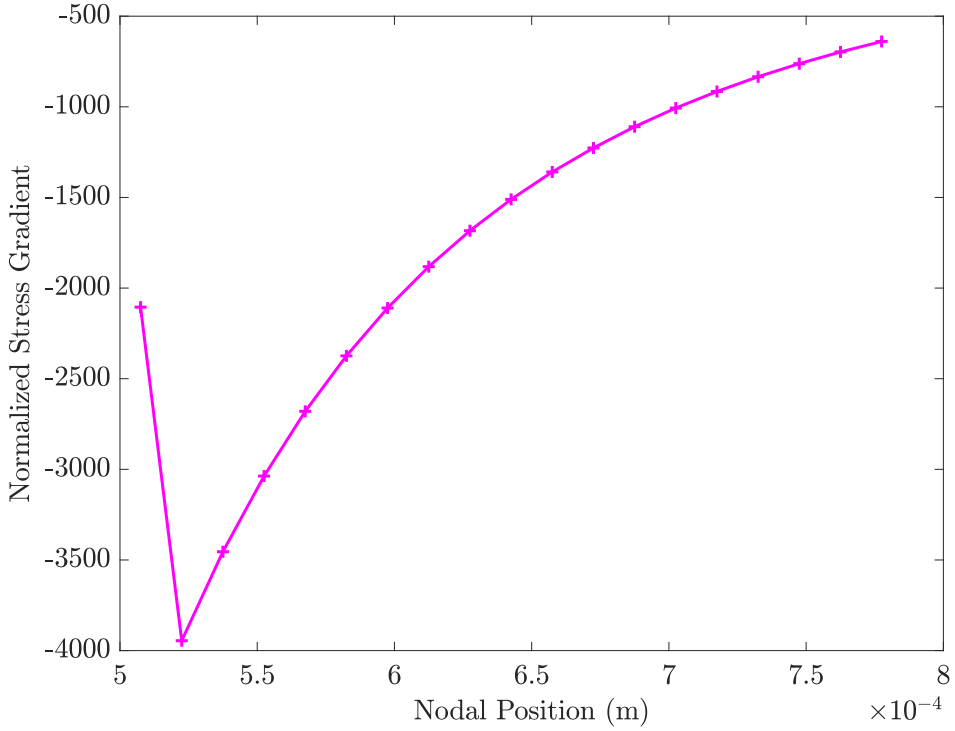


Figure 2.6. Normalized gradient without extrapolation to hole edge

Without discarding any of the gradient points, and using a linear extrapolation back to the edge of the hole edge a value of $-1185\frac{N}{m^3}$ was obtained. This was only about .254 of the theoretical value of $4667\frac{N}{m^3}$. If the first gradient point was discarded hand then the curve was extrapolated back to the edge of the hole, then a linear extrapolation yielded a value of $4682\frac{N}{m^3}$, a number that was in much closer agreement with theoretical predictions. It remained to be seen however, if another technique, a nonlinear extrapolation for example, might be even more accurate since the linear extrapolation was initially chosen only because of ease of implementation. The results of discarding one stress gradient point and using a variety of linear and nonlinear extrapolation techniques are shown in Table 2.2 but they can also be seen graphically in Figure 2.7 which is a zoomed in view of the region of interest taken from Figure 2.6. The dashed red line in Figure 2.7 is the location of the edge of the hole radius and is drawn only for the convenience of the reader.

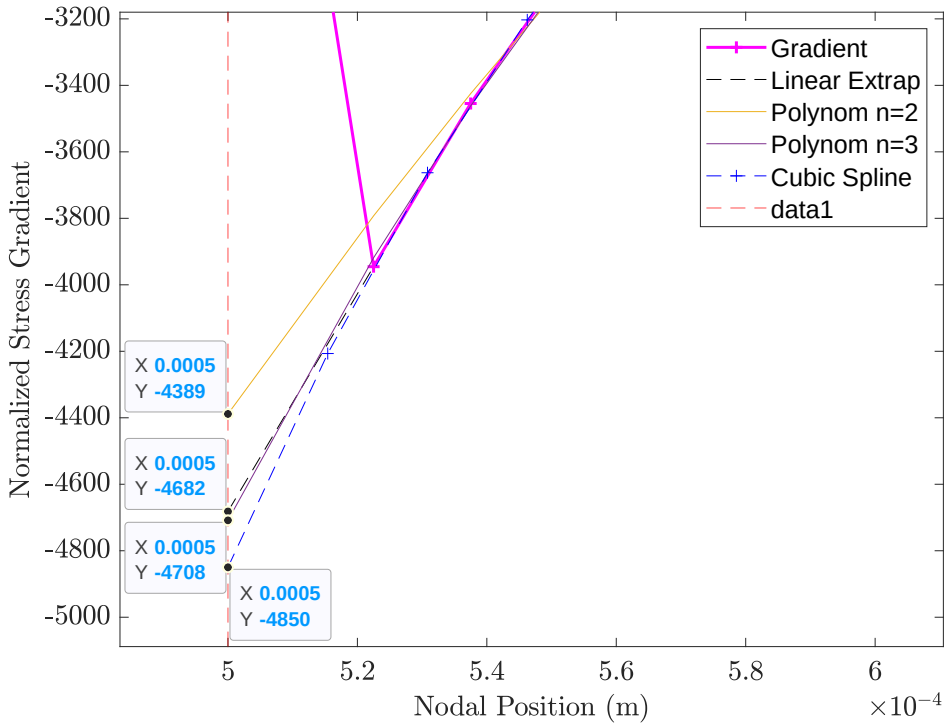


Figure 2.7. Gradient at the hole edge as a function of extrapolation technique

Agreement this close is admittedly somewhat fortuitous given that there is no physical reason why one extrapolation technique should have been more accurate than another but as it was the case that linear extrapolation resulted in the best agreement, and the overall differences between slightly more complicated nonlinear techniques using polynomials of order 2 and 3 were only slightly worse, linear extrapolation was used whenever necessary to predict the stress gradient at the hole edge.

After a sufficiently resolved mesh was determined to have been reached, calculation of the value at the edge of the hole using 2 discard points with different extrapolation methods can be seen in Table 2.2.

Table 2.2. Stress gradient extrapolation method

Extrapolation Technique	Theoretical Value	Predicted Value	Percent Difference
Linear	4667	4682	-.328
Polynomial n=2	4667	4389	5.96
Polynomial n=3	4667	4708	-.879
Cubic spline	4667	4850	-3.92

CHAPTER 3:
Isotropic Specimens

A search for a candidate material to test the accuracy of the UFC started with investigating various polymers. Due to their structure, availability, and strength, several polymers were considered. Although polymer behavior can be quite complex, particularly in additively manufactured (AM) materials, [76]–[78], in general the behavior of isotropic polymers like PMMA makes them an attractive material for the investigation of the new UFC.

PMMA, commonly referred to by the trade names acrylic ™ or Plexiglas ®, is a low cost polymer that is often formed via a process known as mass or bulk polymerization wherein a methyl methacrylate monomer and catalyzing agent are mixed together and cast into a mold forming sheets of specific thickness upon completing the curing process. The nature of its production, coupled with the fact that it is an amorphous and homogeneous polymer, means that its behavior is largely isotropic and ideal for failure interrogation. It also has a number of other desirable properties including transparency, low cost, scratch resistance, ease of machineability, availability, and quantified material properties, all of which combined make it an attractive material for experimental and computational investigation. In addition, the fact that it is both homogeneous and behaves isotropically makes the associate modeling far simpler than that necessary to accurately model composite failure and a good first step towards determining the accuracy of the UFC. To be thorough however, additional materials were selected due to the availability of data in addition to their isotropic behavior. Karihaloo et. al, conducted experimental characterization of hardened cement paste (HCP) and high strength concrete (HSC) [79], [80]. Although the fracture of concrete is an incredibly complicated subject and arguably as a result of its composite nature , poorly described by the approaches of LEFM, HCP is homogeneous, uniform, and brittle enough to warrant further investigation as an isotropic material via the new UFC. Those analyses are also presented in this chapter.

3.1 PMMA Modeling and Testing

Initial testing was conducted at standard quasi-static strain rates, approximately $10^{-4}\ s^{-1}$ using a few different sample geometries. Although different test machines were used, all samples were tested using serrated jaws and a cross head speed of 2 $\frac{mm}{min}$. Both sample geometries, prepared using a waterjet cutting machine, are described in Table 3.1 with a subsequent discussion of results in sub section 3.1.2.

Table 3.1. PMMA sample geometries

Geometry	Dimensions (in mm)	Feature	Orientation to Horizontal
Dog bone	24 x 140 x 6	none	NA
Straight	24 x 140 x 6	oval slit	0°
Straight	24 x 140 x 6	oval slit	15°
Straight	24 x 140 x 6	oval slit	30°
Straight	24 x 140 x 6	oval slit	45°

The dog bone specimens described by row 1 of Table 3.1 were prepared in accordance with ASTM standard D638-10 [81]. These were the first samples to be tested and were instrumented with strain gauges at right angles to the specimen to record both axial and transverse strain [15]. These specimens were used to generate fundamental material properties, including both the tensile Modulus and Poisson's ratio, that were used for subsequent modeling. But in addition, it was also used to generate an average failure strength with good agreement predicted by both the experimental and computational models. The geometry of both sets of specimens described previously in Table 3.1 can be seen in Figure 3.1.

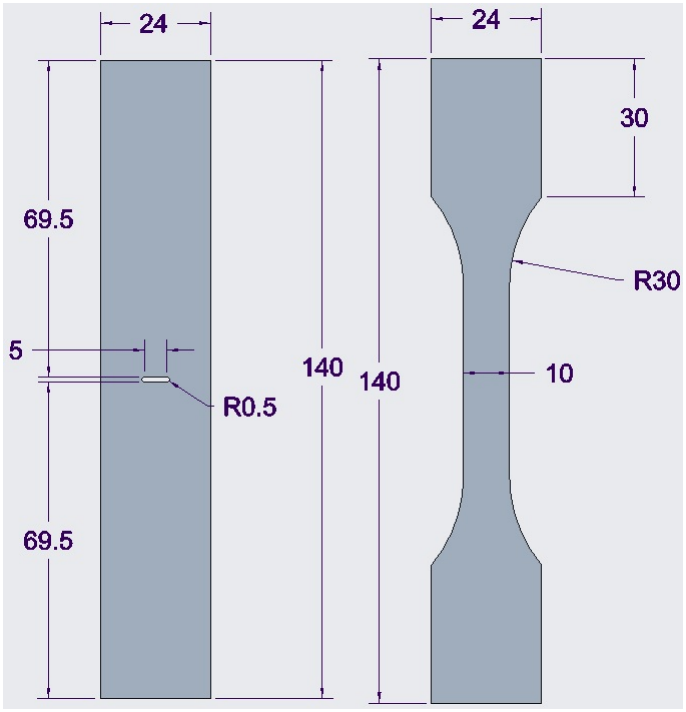


Figure 3.1. PMMA specimen geometry (all dimensions in mm)

Further details of the full model are given in Section 3.1.2.

3.1.1 Sample Preparation and Test Setup

Owing to the low melting temperature of PMMA, approximately $320°F$ and ease of machining, all PMMA test samples were prepared using a waterjet cutting process. This process was not only fast and accurate, but it resulted in a high level of sample consistency owing to the fact that all the waterjet machines were controlled via computer numerical control (CNC) vice manual operation. Waterjet cutting machine produce high precision cuts making them ideal for preparing fine or intricate details and features. All of the samples described in Table 3.1 were prepared using this technique.

The predicted failure strength of PMMA was previously recorded and relative to traditional materials like metals, its mechanical properties, as shown in Table 3.2, are relatively low. As a result, a 50kN load cell and ordinary serrated jaws were sufficient to test all of the isotropic samples until failure.

Table 3.2. Experimentally measured properties of PMMA [46]

E(GPa)	Poisson's Ratio	Failure Strength (MPa)
2.96	0.346	58.3

One of the test machines used for this testing is shown in Figure 3.2.



Figure 3.2. Instron test machine with CFC sample

3.1.2 Modeling and Results

In order to compare the recently developed UFC with experimental results, it was necessary to model the scenarios listed in Table 3.1 in order to calculate the stress gradient that is an element of Equation 2.19. A brief mesh resolution study was first conducted in order to ensure the accuracy of the computational solution. This mesh resolution study was used as the basis for the remaining PMMA models all of which were developed around conventional, reduced integration, 4 noded shell elements (S4R in Abaqus) run at full nodal output precision. The robustness of these elements combined with a reduced integration formulation makes them broadly applicable and capable of accurately modeling a wide range of different applications. The stress gradient, namely $\frac{d\sigma}{ds}$, is that measured in the direction of failure. As a result, the stress tensor element used for the calculation of the stress gradient was the S22 value or the stress occurring on the y face of any element in the y-direction. These values were taken at nodal location so there are certainly differences from what would have been calculated using the integration points but for the ease of calculation, nodal values were the most convenient to employ even though their variance from the solution at the integration points is greatest in the region of strong gradients. In order to conduct a mesh resolution study, the S22 values were collected for otherwise identical problems with varying numbers of elements and the S22 values of stress were plotted to look for the point where the time to solution compared with the change in S22 value reached a point of diminishing returns. A plot of the S22 stress as a function of the number of elements is shown in Figure 3.3.

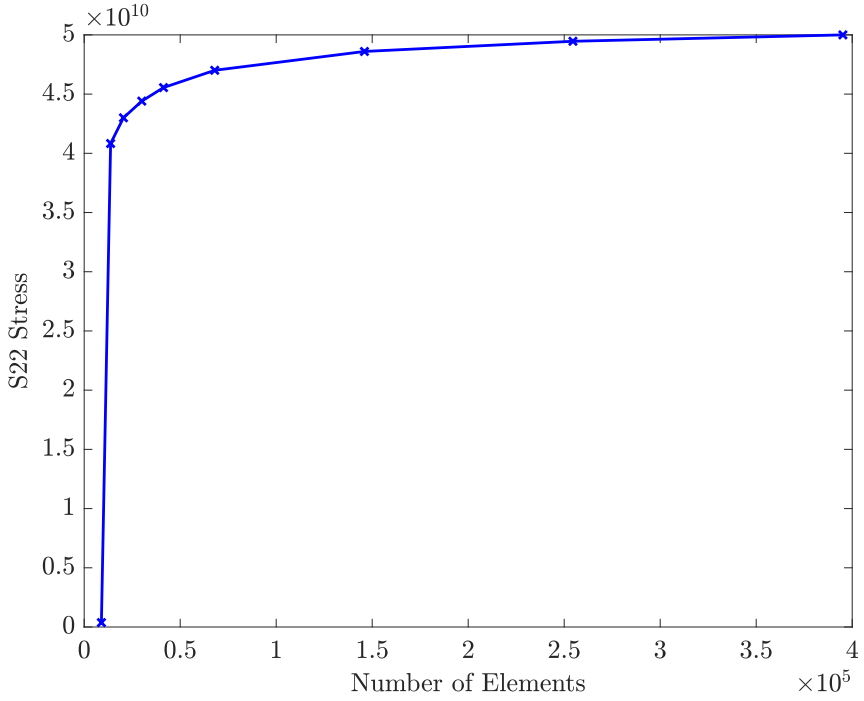


Figure 3.3. Change in PMMA S22 stress with element count

It is clear from this plot that after about 7 subsequently finer mesh iterations mesh, i.e. after the element count was approximately 145k elements, little change in S22 was seen using this problem definition, i.e. material, boundary conditions, and loading. As a result, this mesh density was determined to be sufficient for the purposes of modeling the other similar scenarios moving forward. This still left the question of the number of processors to use in the interest of optimizing the speed up of the problem and to minimize impact on users competing for resources in a shared computational environment. Dassault's algorithm for the number of tokens used by a multiprocessor instance of Abaqus is $INT(5 * N^{0.422})$ where N is the number of processors and INT is merely a function that rounds the sum of this number down to the base integer value. Towards that end, a brief strong scaling study was conducted to determine where the time for a fixed job size was minimized as a function of the number of cores used. The results of this are plotted in Figure 3.4.

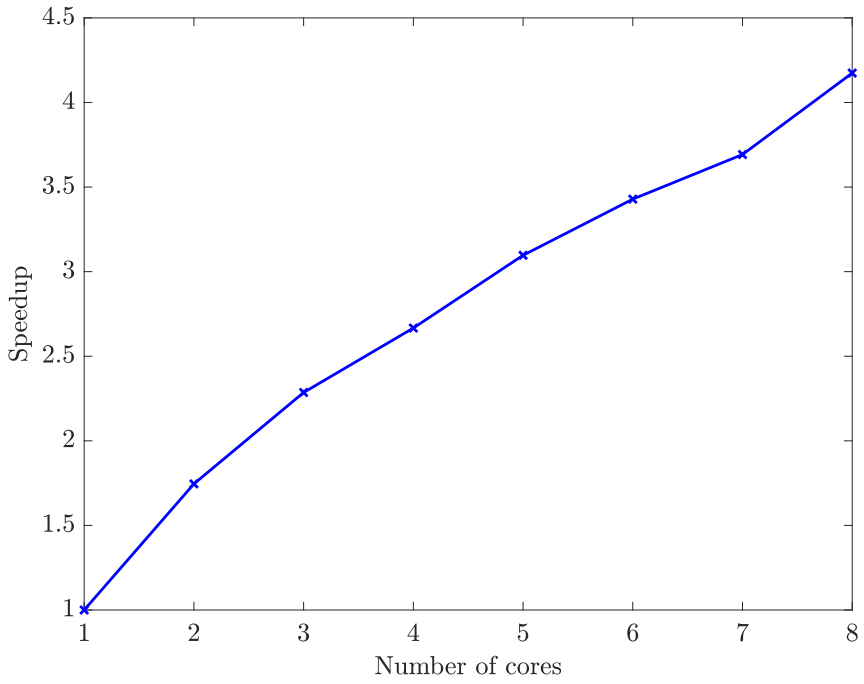


Figure 3.4. Job speed up vs core count

As Figure 3.4 demonstrates, the speed up as a function of cores had not yet plateaued by the time the maximum core count of 8 was reached and so it is likely that a peak value occurs at some number of processors greater than this low value. Although there was little change in the accuracy of the S22 value with an appreciably greater number of elements, because the jobs ran so quickly and at the maximum core count only used 2 additional tokens, generally all jobs were run using 8 cores unless otherwise noted.

To keep the job size within reason while simultaneously optimizing their accuracy, the region around the feature was partitioned so that a swept mesh could be used. This allowed for a higher local mesh resolution in the region where the greatest stress and stress gradient were known to occur with a lower number of elements where they were unnecessary. A node set of a limited number of nodes directly on either side of the feature was created so that a corresponding display group could be used to easily interrogate the stress gradient in

the nodes where it was most relevant. Since the gradient in the vicinity of the hole was of the most interest, and it dropped of rapidly as a function of the distance from the hole edge, using a much greater number of nodes than those local to the edge of the hole provided no measurable value. Figure 3.5 shows a closeup of the mesh with the S22 stress and the right hand side node set in the vicinity of the feature of interest.

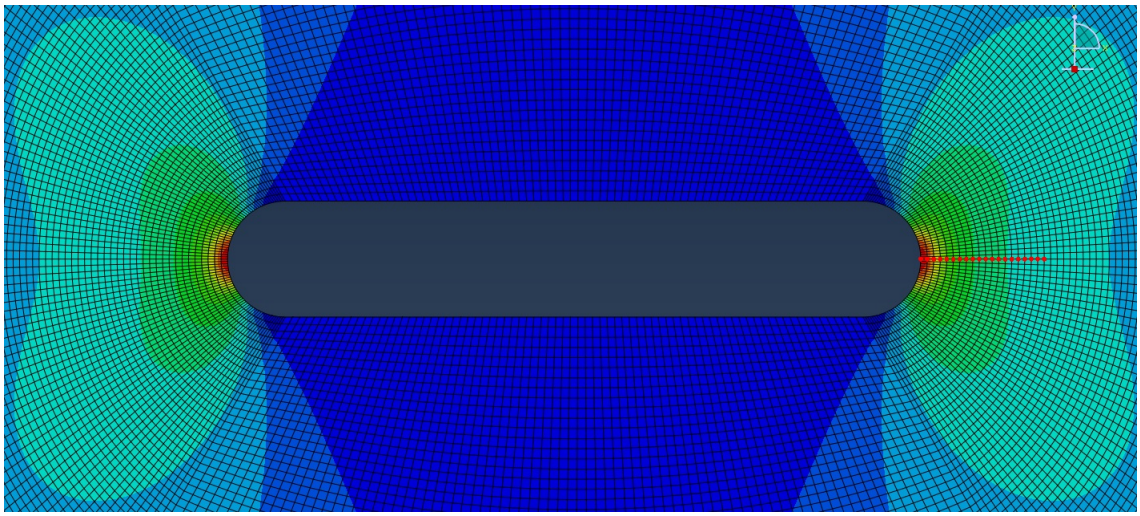


Figure 3.5. 6mm PMMA slot S22 stress

After each of the relevant stress gradients was generated for the various models, only then was it possible to begin the comparison with experimental data. In order to do so however, first a value for κ_{fail} had to be computed. As pointed out in Section 2.5, κ_{fail}, like Young's Modulus E, is a material constant and as a result, can be considered a constant throughout these analyses even when the angle of the slot changes in orientation. To calculate the value for κ_{fail} that would be used for the remaining analyses, one slotted feature scenario was chosen as a baseline from which κ_{fail} was solved for. This required using the value of σ_{fail} measured experimentally and $\frac{d\sigma}{ds}$ measured computationally. It should be pointed out that as was discussed in Section 2.5.1, the accuracy of calculating the stress gradient close to the hole was highly dependent on the curve fitting technique used. In other words, if a third order extrapolation technique were used with two gradient points having been discarded, it resulted in an appreciably different value for the calculated stress gradient than if a linear extrapolation technique that discarded only a single point were used. Ultimately the most

accurate technique was a linear extrapolation used with only a single discarded gradient point. After a sufficiently accurate value for $\frac{d\sigma}{ds}$ was calculated using modeling, the value for κ_{fail} that was then used in all subsequent models, was determined. Figure 3.6 shows that the failure stress calculated in this way agreed well with the theory [15] although some differences between computational and experimental results were present.

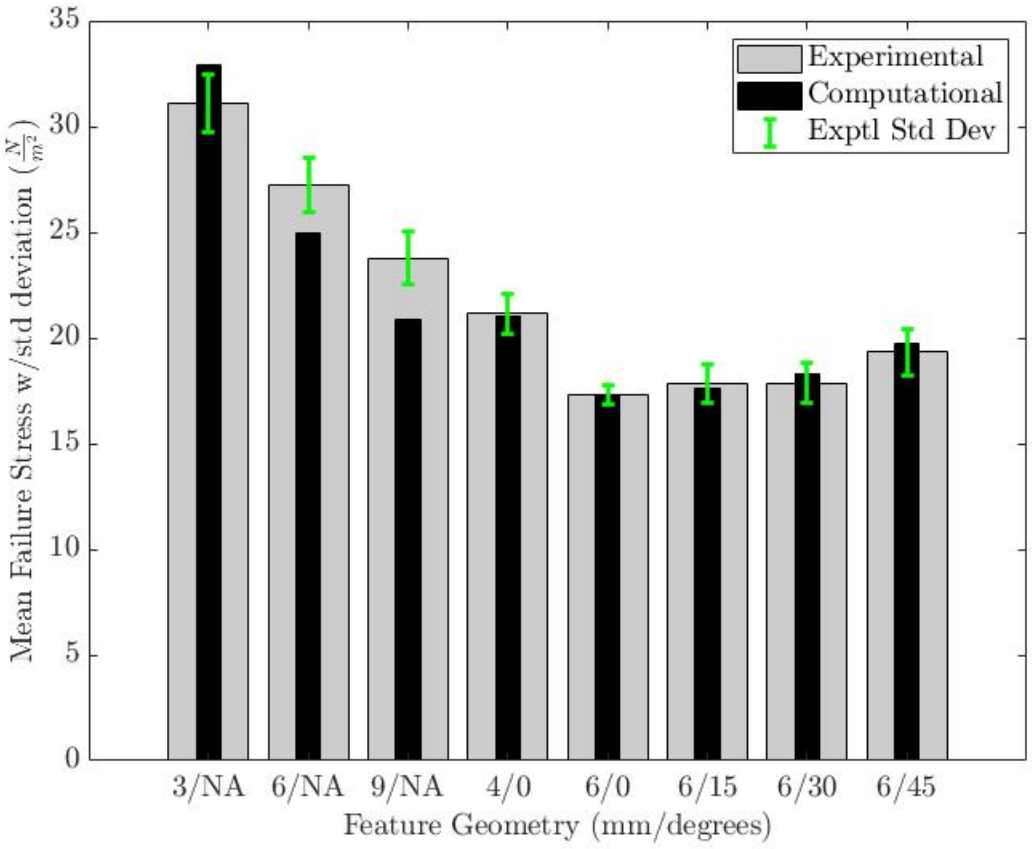


Figure 3.6. Comparison between theoretical and experimental PMMA data Adapted from [15]

Because the agreement between theory and experiment was so close, it was deemed sufficient to proceed on to considering a different material.

3.2 Hardened Cement Paste (HCP) Modeling and Testing

Although the previous experimental data for PMMA confirmed good agreement with the UFC, any truly accurate theory should compare well to a broader set of materials and scenarios, accurately predicting failure outside of just a single narrow regime. While the PMMA samples provided good specimens for both experimental and computational characterization, the nature of their 6mm long feature meant that, regardless of whether it was oriented at 0 degrees or 45 degrees, its behavior was somewhere between a perfectly circular hole and that of a sharp crack. Fortunately Karihaloo [79], [80] et al. conducted an experimental study wherein they compared the failure of beams made of HCP subjected to three point bending with theoretical predictions. Although the consideration of HCP is more complicated than the previous PMMA work owing to variations that typically necessitate different failure models based on the size of the specimen of interest, the reason that made it most attractive for consideration here was that it represented more of a sharp like crack than a more rounded and subtle defect as was investigated previously. Fortuitously, HCP is a brittle, homogeneous, isotropic material, that was both similar and different enough to warrant further investigation and interrogation via the UFC.

In the aforementioned investigation, beams of varying aspect ratios were tested with constant spans but different crack to depth ratios. In a manner similar to that conducted previously in Section 3.1, HCP was modeled for the generation of a stress concentration factor. This stress concentration factor was then compared with those predicted by the UFC to determine how accurately it agreed with computational results simulated by a half symmetric, three point bending problem. Although in general the test described in this work is what is referred to as a 3 point bending test, the geometry and set up were useful for testing a scenario where crack opening in mode I occurs. The mode I scenario is where the crack propagates in a direction normal to the plane in which it occurs [82]. Table 3.3 contains the entire range of problems produced by Karihaloo investigated here.

Table 3.3. HCP Properties from Karihaloo Source: [79]

Depth "W" (mm)	α	Mean Failure Stress (MPa)
75	0.05	0.53
150		0.38
300		0.33
50	0.10	0.44
100		0.35
200		0.30
50	0.30	0.32
100		0.29
200		0.20
50	0.50	0.16
100		0.13
200		0.11

For the initial setup of this problem, approximately 150k three dimensional elements were used and were biased towards the "crack face" from both the x and y direction in an attempt to make these problems numerically efficient while maintaining satisfactory accuracy. The element count was increased appreciably after initial runs indicated a lack of refinement using a technique similar to what was discussed Section 3.1.2. The element type used for this scenario was the C3D8R type which are first order, 8 noded linear hexahedrons with reduced integration and hourglass control. One mesh with a crack aspect ratio of $\alpha = .05$, where $\alpha = \frac{a}{W}$ where a is the crack depth and W is the beam depth, both of which are measured in the y-direction as shown in Figure 3.7.

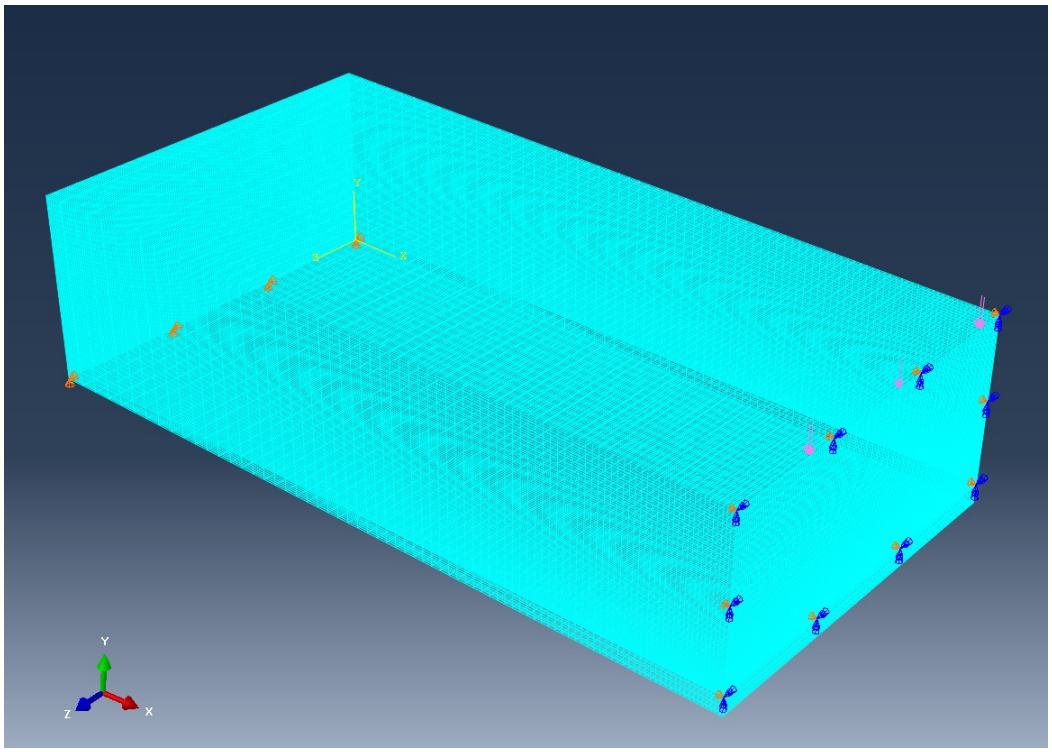


Figure 3.7. Half symmetric HCP beam with mesh and boundary conditions

The parameters of the beam were changed as per the original work wherein various aspect ratio HCP beams were subjected to 3 point bending [79]. The span to depth ratio was 4 with a width of 100mm for all scenarios investigated. The primary variable of interest for this investigation was the failure stress at the crack edge so as a result, a 500 N load was applied all along the top edge in an attempt to simulate a line load.

For these simulations, the crack was simulated by partitioning the face of the beam along the plane of symmetry and applying the symmetric boundary conditions everywhere along that face with the exception of the area representing the opened crack surface. In this way the mechanics of the problem could be simulated but the number of elements in the mesh remained small enough to enable reasonably rapid iteration compared to what would have been necessary if a more traditional approach of meshing a region in the vicinity of the crack edge had been pursued. A closeup of the crack face is shown in Figure 3.8.

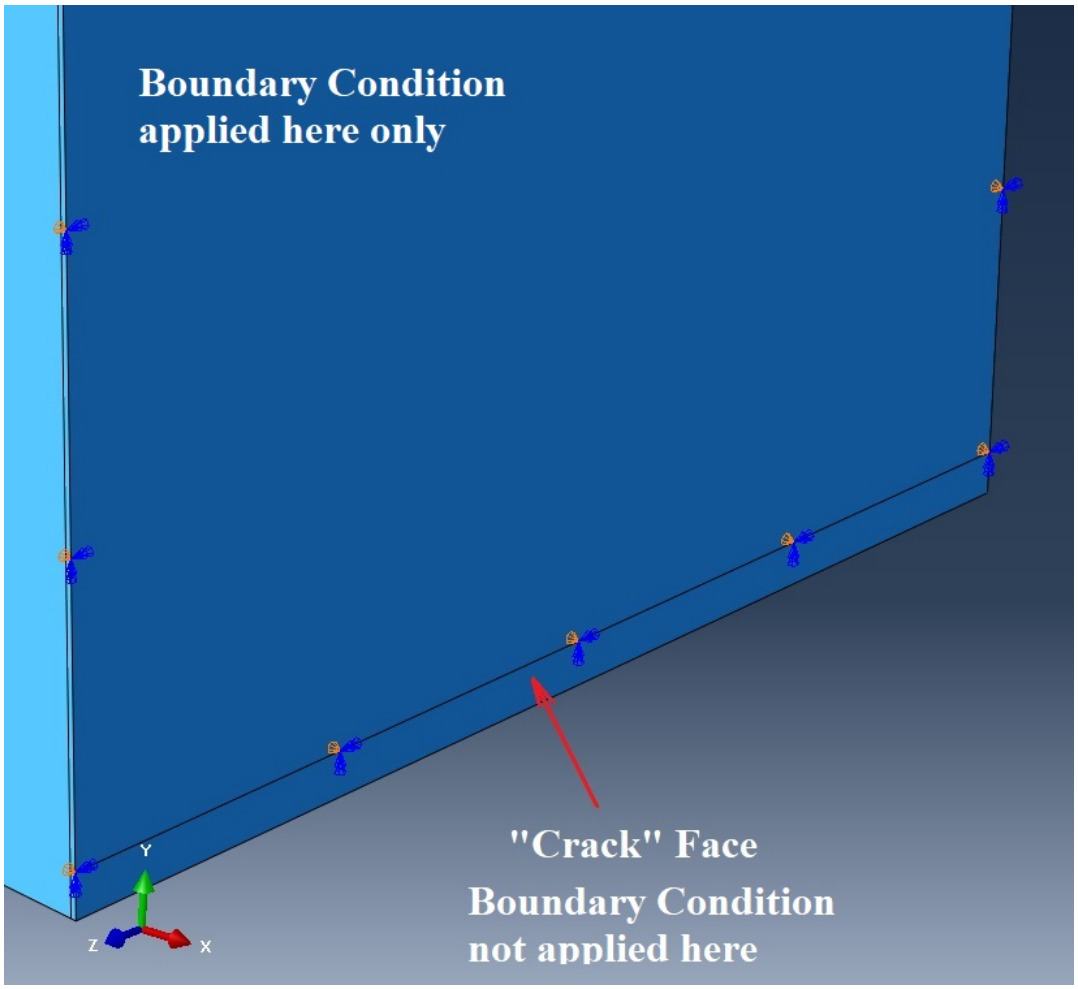


Figure 3.8. Simulated crack face in HCP

The stress gradient along the crack face was not only consistent but was also symmetric. This was measured using node sets at three locations along the crack edge upwards in the anticipated direction of crack propagation. One node set was chosen at the left most edge, with another at the center, and yet another along the right most edge as shown in Figure 3.9. Between 500k and approximately 2,000k reduced integration C3D8R elements were initially chosen, depending on the scenario, to model these configurations.

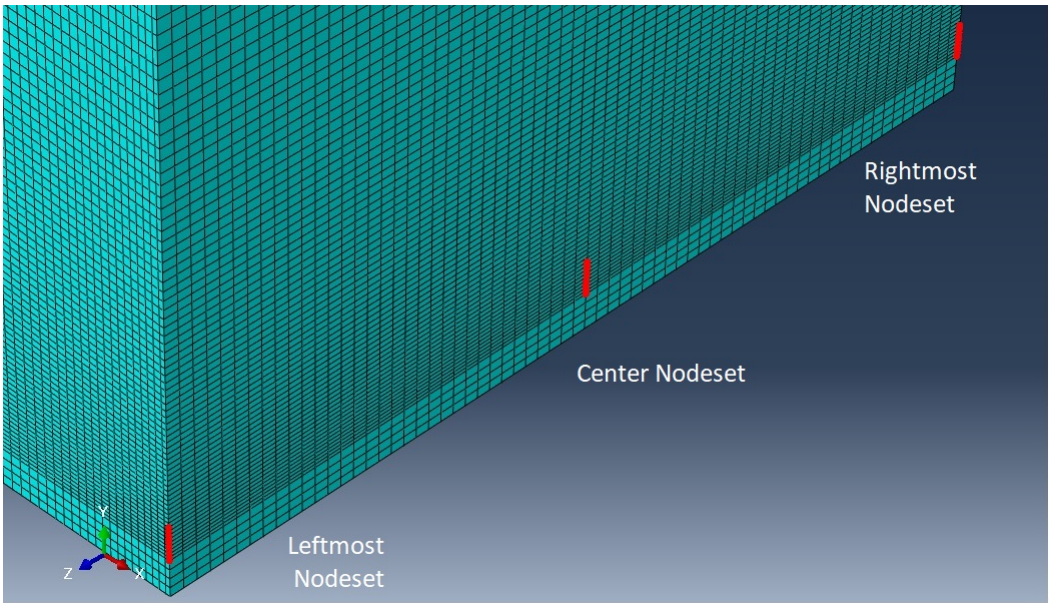


Figure 3.9. Node sets along HCP crack tip for stress/gradient analysis

After investigating the stress and the stress gradient along the plane of symmetry, in this case the y-direction, it was apparent that the behavior of both was consistent and symmetric. This is shown in Figures 3.10 and 3.11. Although it appears that there are only 2 of the 3 node sets plotted in both figures, the left most and right most nodal values were identical so those curves lie on top of each other and as a result, only one is visible.

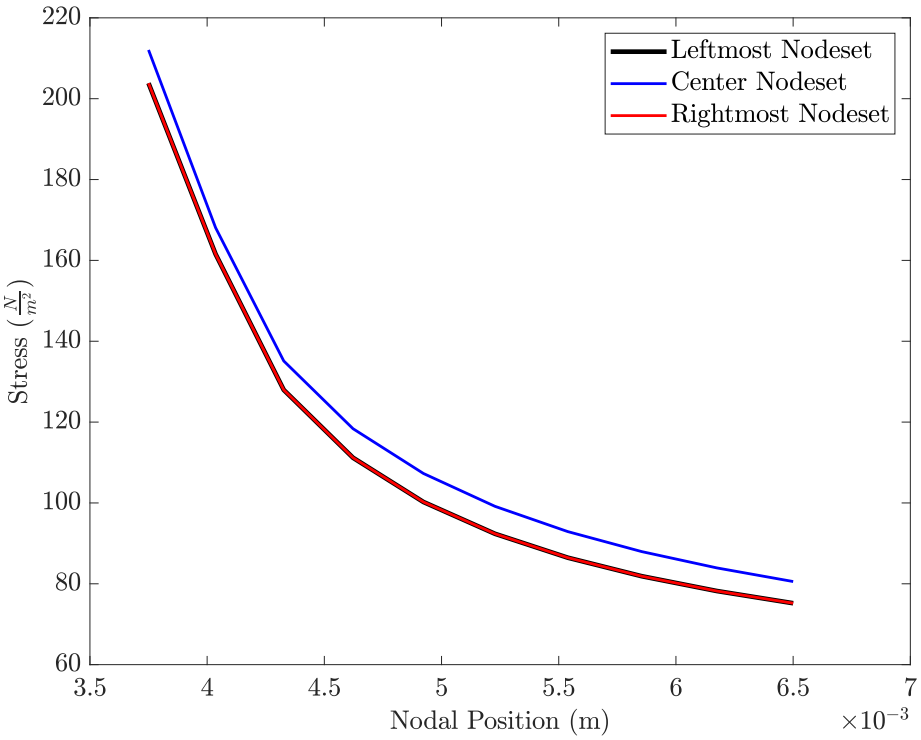


Figure 3.10. Node set stress at three different positions along HCP crack

Due to differences between values for stress as it is calculated at the integration point vs how it is interpolated at the nodes, if reduced integration elements were selected, as they were by default, then the gradient was not nearly as well behaved. In the case where reduced integration elements were used, namely C3D8R vice C3D8, the stress exhibited a sharp discontinuity and turned downward as it approached the edge of the hole. This was counter to theoretical predictions that dictated that the stress should tend towards infinity the closer to the edge you interrogate. When ordinary, i.e. non reduced integration elements, were used however, the stress increased before decaying as predicted by theory. Using 2*nd* order accurate elements did not make any difference at the mesh resolutions used here but they did provide more computationally efficient and essentially identical answers at a far lower mesh resolution. Both Figures 3.10 and 3.11 were generated using 2nd order, fully integrated elements.

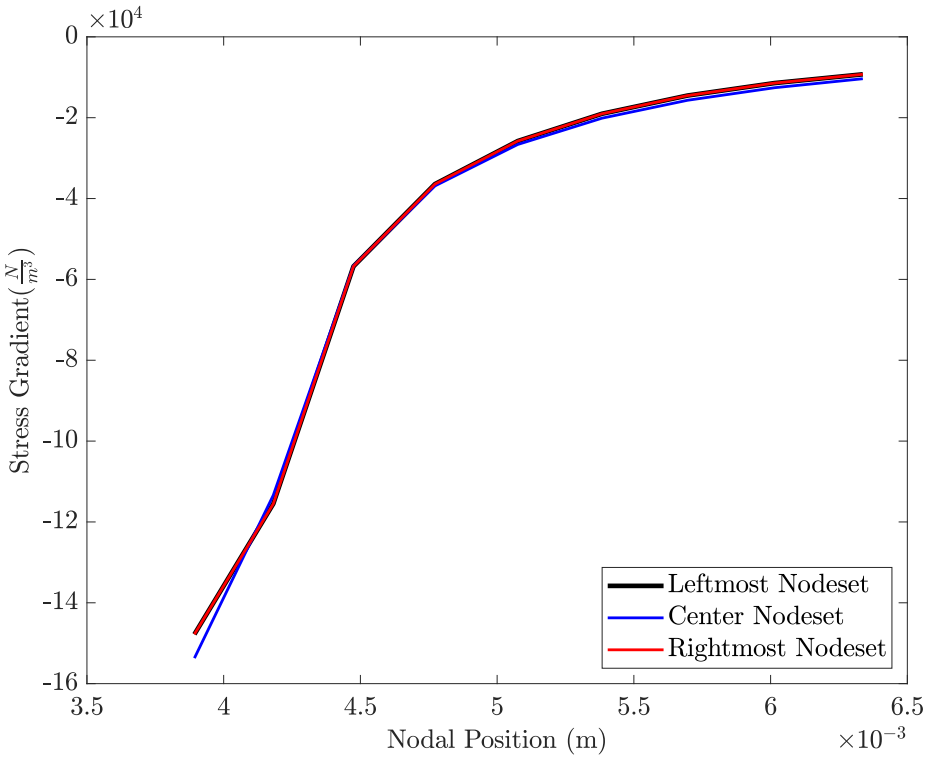


Figure 3.11. Nodal stress gradient at three different positions along the HCP crack

A further check of the accuracy using this technique was developed through the calculation of the stress intensity factor (SIF) K. The SIF is a value used to quantitatively describe the stress in the immediate vicinity of a crack and is related to the two material properties κ_{fail} and E_{eff}. Equation 3.1 is the most common form of this equation.

$$\sigma_{eff} = \frac{K}{\sqrt{x}} \tag{3.1}$$

Here x is the distance from the crack tip and σ_{eff} is the failure stress that, upon subsequent manipulation, yields Equation 3.2.

$$\kappa_f = \frac{K^2}{E_{eff}} \tag{3.2}$$

In this form of the equation, κ_f is a notch failure value related to the critical energy release rate and E_{eff} is the effective modulus. For the HCP scenario of interest here, κ_{fail} was calculated using the first row of Table 3.4 similar to the discussion of Section 3.1.2.

K was calculated using a curve fit to computational data generated from the analytical FEA program, an example of which can be seen in Figure 3.12.

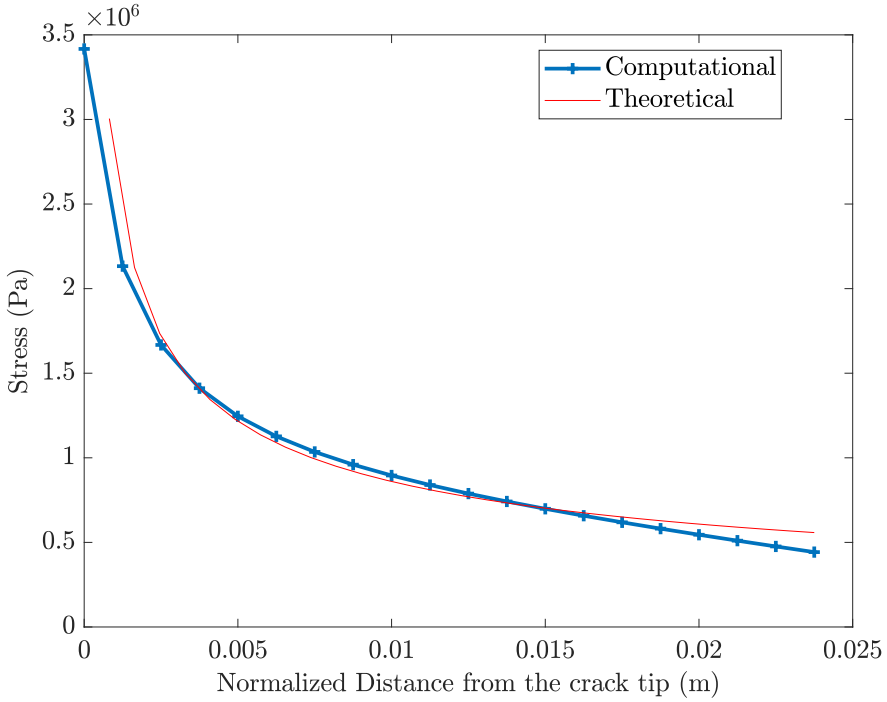


Figure 3.12. Curve fit for generating SIF

From Section 2.2 we know that Inglis' solution predicts an infinite stress at the root of the crack. The FEM however, is only able to predict a *finite* stress even where other theories predict a much higher value.

3.3 Results

The difficulty with determining stress, and subsequently stress gradients via the method of Section 2.5.1, is that unlike force and displacement, stress (and strain) are calculated at the integration points of the element. This means that their values have to be interpolated at the nodes based and are subsequently different. In regions of strong gradients in particular, using reduced integration elements resulted in answers that varied appreciably from those calculated had integration points been used. In theory this effect should be minimized when the mesh becomes so dense that the distance between the nodes and integration points becomes infinitesimal, but where strong changes, i.e. gradients, occur, it was easy to underestimate how sensitive calculations based on the gradient were. This was unfortunately the case with the calculations based on the mesh in the vicinity of the crack and as a result, appreciable variation was observed between the failure loads predicted using finite element analysis to generate the stress gradient necessary to test the UFC and those measured previously by Kariloo and his team [79]. Fortunately in attempting to validate this theory, prior researchers developed a 2-dimensional analytical code that used integration point values instead of nodal ones used here. When coupled with the fact that there was no appreciable variation in stress or stress gradient in the z-direction it meant that the use of this 2-dimensional analytical code should be a sufficiently accurate alternative to using the FEM [15]. Table 3.4 shows the comparison between stresses calculated in the previous manner with experimental results. This gives a subsequent measure of accuracy using the new UFC.

Table 3.4. Theoretical and experimental failure loads Adapted from [79]

Depth "W" (mm)	α	Exptl Failure (kN)	Theoretical Failure (kN)	% Difference
75	0.05	3.98	3.67	-7.71
150		5.63	5.14	-8.66
300		9.83	7.44	-24.28
50	0.10	2.22	2.40	7.97
100		3.49	3.54	1.30
200		6.06	4.71	-22.21
50	0.30	1.62	1.49	-8.11
100		2.85	2.36	-17.30
200		4.09	3.14	-23.16
50	0.50	0.8	0.86	7.14
100		1.32	1.23	-6.84
200		2.14	1.77	-17.39

From Table 3.4 it is easy to see that the closest agreement was achieved between experimental and predicted loads using the UFC when the depths compared were the two shallowest for each span to depth ration α. This is likely due to the size effects exhibited by the materials Karihaloo was investigating vice the UFC described by Equations 2.18 and 2.19. This well known phenomenon is when decreasing strength is observed with increasing size (for compressive strength) for concrete members. Although not shown explicitly here, as the experimental failure load increases for any given span to depth ratio, the failure stress actually decreases. This unusual behavior is a result of microstructural features that are statistically based and as a result, can not be accurately accounted for here. Where the samples are smaller, and hence the participation of microstructural voids or damage are likely to exist in smaller quantities, the UFC provides reasonable agreement with experimental results. With only one exception, i.e. the scenario where $\alpha = 0.3$ and $W = 100$ mm, the difference between experimental and theoretical predictions are all less than 10%. It is likely that in the excepted case a greater number of voids or other microstructural features existed that

caused a more appreciable difference to occur between experimental and theoretical results. The values for small crack ratios at small depths that are generally accurately predicted in this manner are also likely to vary as a result of this same microstructural variation and its subsequent effect on experimental measurements. As a result, this technique was determined to be sufficiently accurate as to be applicable to the general class of isotropic materials so that analyses could begin on the more complex and difficult class of anisotropic materials.

CHAPTER 4:
Anisotropic Specimens

Having established good agreement between computational modeling and experimental results for the application of the UFC to predicting the failure of isotropic materials, additional materials with different behavior were prepared for follow on investigation. Any truly satisfactory model would have broad applications beyond a single niche and should accurately predict the failure of both isotropic and anisotropic materials with at least some degree of accuracy. It was in an attempt to quantify the breadth of applicability and accuracy of the approach that both poly lactic acid (PLA) and CFCs were also tested.

4.1 PLA Sample Preparation

PLA is a aliphatic polyester type of thermoplastic polymer, often referred to as a biopolymer or bioplastic because it is made from organic and biodegradable materials like corn starch. Invented in the early 20^{th} century, because it is not petroleum based, it is generally considered to be a more environmentally friendly and sustainable product than traditional petroleum based plastics. The mechanisms contributing to biodegradability are an area of ongoing research and there is currently much debate about its sustainability and degradation over time [83]–[85]. Because of its mechanical properties, availability, and low cost however, it is likely to be a material of choice for the foreseeable future. Even though it is a polymer, the structure and manufacturing method of PLA means that predicting its behavior, in particular the failure of samples used with fused deposition modeling (FDM), alternatively referred to as fused filament fabrication (FFF), might ordinarily be much more difficult than for simpler, amorphous, and isotropic materials. Printed PLA however, is far more complicated than that of the polymer PMMA discussed in section 3.1. Numerous researchers have shown a variety of PLA parts created using FDM exhibit consistently measurable anisotropy from layer to layer owing to differences in bonding strength that naturally occurs from one printing layer to the next [86]–[88]. In general, depending on the application, such behavior would likely be undesirable, but the ability to induce and control anisotropy by overriding ordinary printing directions was precisely what made the material attractive for use here.

The default setting for slicing software used with 3-d printers is to manufacture a part in a manner that balances time, material usage, and structural characteristics to produce parts that are a balance of such features vice one having the highest possible strength. As the maturity of the FDM process increases however, and users are no longer seeking to generate simple models but rather are making parts intended to replace some other part manufactured via a more traditional process, the need to improve and control strength, and even directionality, will increase as well. As a result, although the default orientation that a printer will generally use is one where the material is printed in different layers at different orientations, typically a $+45^\circ$ and -135°. In the interest of inducing this behavior we controlled the print direction using Ultimaker's Cura software to control the printing parameters such that the PLA fibers were printed in a single direction, here 0°, corresponding to the direction in which loading would occur. An example of controlling the print direction is seen in Figure 4.1.

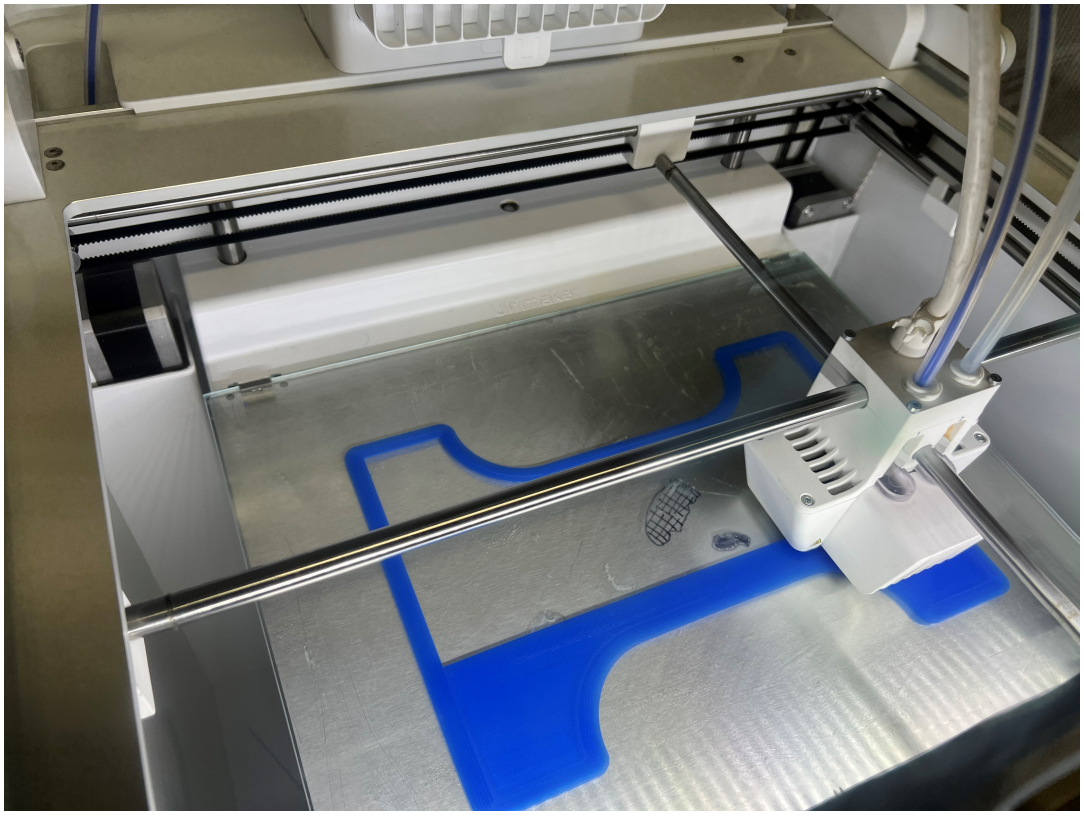


Figure 4.1. Ultimaker unidirectional printing PLA dogbone

Although PLA is by most standards considered to be a brittle material [89]–[91], its behavior as witnessed during testing showed appreciable variation ranging from ductile to brittle despite the fact that the print orientation and other parameters were identical. Although all controllable printing parameters, including temperature and the direction, were identical, differences in the printing environment, e.g. closed vs open environment, dehumidified vs ambient, and the printing feed stock itself, including supplier, storage conditions, and possibly even color, all likely contributed to observed differences. The results and application of the UFC however, remain equally applicable as will be shown. Because the PLA samples were initially tested and their failure found to occur suddenly with crack propagation occurring at a rate that was beyond the observer's ability to see it, digital high speed video (HSV) cameras were used in an attempt to capture this behavior. Digital Phantom ® cameras were used to capture all HSV images shown here.

The PLA samples were prepared according to Table 4.1.

Table 4.1. Printed PLA tensile samples

Geometry	Printer/PLA	Layup	Feature (mm)
Straight	Ultimaker	Unidirectional	No hole
Dogbone	Prusa	Unidirectional	3mm circular hole
Dogbone	Prusa	Unidirectional	6mm circular hole
Dogbone	Prusa	Unidirectional	10mm circular hole

The overall sample measured 240mm long by 160mm in width. When printed, the ends were 3mm thick and tapered down to 1mm in the central 80mm wide gauge length section of the specimen. The samples were printed with only one side having thicker ends. Separately printed 2mm thick tabs were fixed to the other side of the sample after both prints were complete. This gave the sample ends gripped by the jaw a maximum thickness of about 5mm. Using tabs in this manner was necessary to minimize failures that would otherwise occur at the specimen ends due to the low compressive strength of thin PLA in addition to a relatively wide range of force that hydraulic grips tend to apply. Initially printing the tabs on

only one side of the specimen also eliminated the need to print with structural supporting material that would otherwise have been necessary to prevent sagging for regions higher than the print bed. A finished sample printed on the Prusa with a 3mm drilled center hole is shown in Figure 4.2.

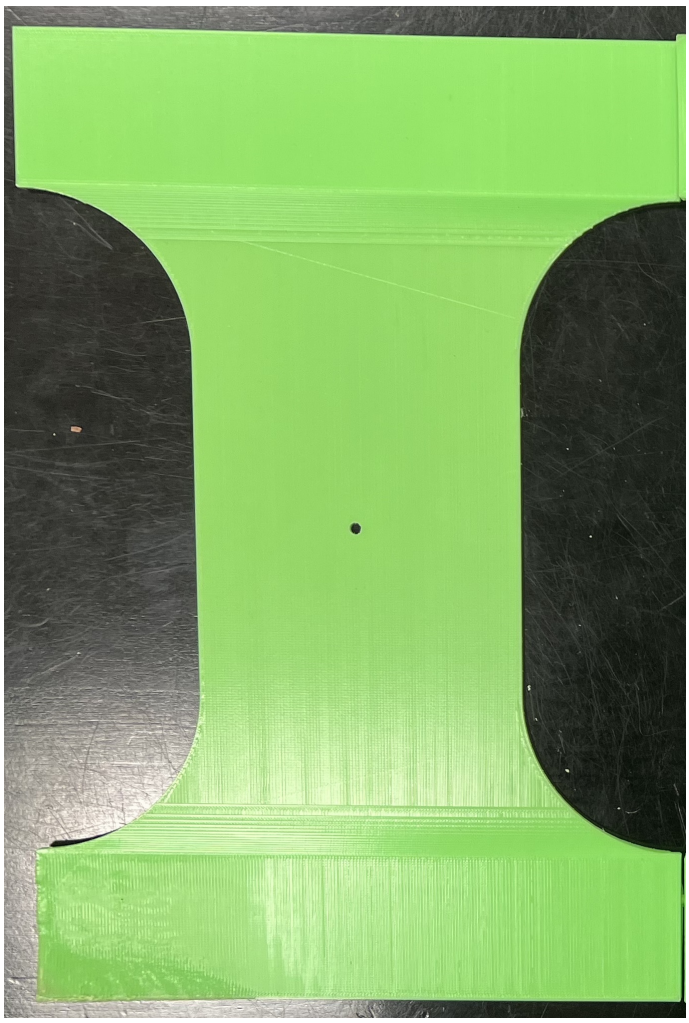


Figure 4.2. Unidirectional PLA dogbone w/3mm hole

Schmeier and other showed that the quality of material at the edge of any hole is best when it is drilled vs when it is printed in so for this reason, the various holes were drilled rather than printed in [92]. As any printing media needs to be hot enough to flow through the print

head nozzle, printing precise parts where elements of the geometry are not supported is impossible. This is the purpose of printing using a structural support media but doing so is not without downsides. In addition to speeding up the printing process, printing without using structural supporting material resulted in a better surface finish than otherwise would have been achievable had it been used. This was desirable so as to minimize potential failure locations that could have otherwise resulted from a non smooth or irregular, and subsequently stress concentration prone, surface. The tabs were glued down to the sample with a cyanoacrylate based adhesive and clamped in place for several hours to ensure a strong bond. Extreme care had to be taken when gluing PLA samples in this manner however, as the working time before the glue set enough to permanently fasten the adjoined parts was extremely short so the potential for adjustments were minimal.

4.1.1 Modeling and Testing

Testing of the unidirectionally printed PLA dogbones was conducted using an MTS tensile test machine. These samples were made with the intent that the location of failure could be observed more accurately than if standard tensile dog bone specimens like those discussed in 3.1 were tested. Figure 4.3 shows the setup of this test.



Figure 4.3. MTS testing of unidirectional PLA dogbone w/3mm hole

The full configuration was also modeled using approximately 630k elements of which approximately 590k were tetrahedral C3D10 elements. A small partition measuring approximately 10*R where R was the radius of the center hole, was used with a swept mesh of C3D8 hexahedral elements due to their inherently greater accuracy, at a consistent mesh density, in the region of interest. The displacement boundary conditions for the scenario where a 3mm displacement was applied at the top surface is shown in Figure 4.4 (elements

not shown). Although the computational efficiency of the problem could have been improved by using a quarter symmetric model, a fact enabled by geometric planar symmetry, symmetric loading, and symmetric boundary conditions, due to the relatively small number of elements the code was easily capable of handling the full model rather than inducing symmetry artificially. Furthermore, when modeling composites even if the boundary conditions and geometry are symmetric, the fiber orientation in the layup can provide misleading results. In the interest of consistency and minimization of misleading results for other analyses, even though the PLA specimens could have been simulated to take advantage of symmetry, this was not done out of a sense of caution. The curvature of the specimen in two directions necessitated tetrahedral elements be used because of difficulties in meshing a part with such geometric features.

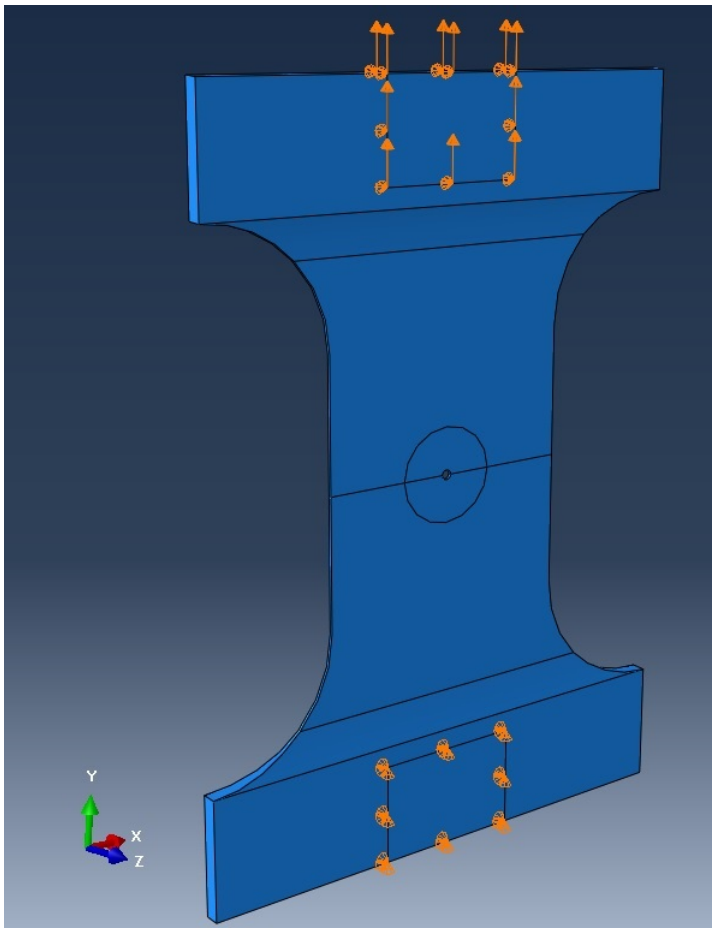


Figure 4.4. PLA dog bone model w/3mm hole and BCs

Although it was not surprising, when the sample without any central geometric feature was modeled under a 3.0 mm displacement, the greatest stress was shown to occur where the curved portion of "dog bone" end necks down to the straight central section comprising the gauge length. Failure occurred at that location several times during testing. If close attention was not paid to the parameters used to generate the .stl file in whatever solid modeling package was used to create the geometry, then the user would unintentionally introduce low fidelity features that would induce failure at this location. This was a result of the fact that the .stl file, an intermediate step between the solid model and the g code generated by the slicing software, generally operates with a default fidelity setting that favors speed and

convenience of manufacture rather than final quality of the printed geometry. This can be seen in a series of flattened curves with discontinuities where they connect to each other in the code's attempt to maintain the larger overall radius of curvature. When that occurred, failure occurred preferentially at those locations due to obvious stress concentrations. In order to circumvent this tendency, the user must force the software to create as high of a fidelity .stl file as is possible by minimizing the cord height. This ensures that sections that are curved are created using true curves rather than a collection of imperfectly printed curved segments. As long as resolution was optimized in this manner then the likelihood of a successful test was optimized although it was by no means guaranteed.

A closeup of typical results of the PLA dog bone model with a central hole are shown in Figure 4.5.

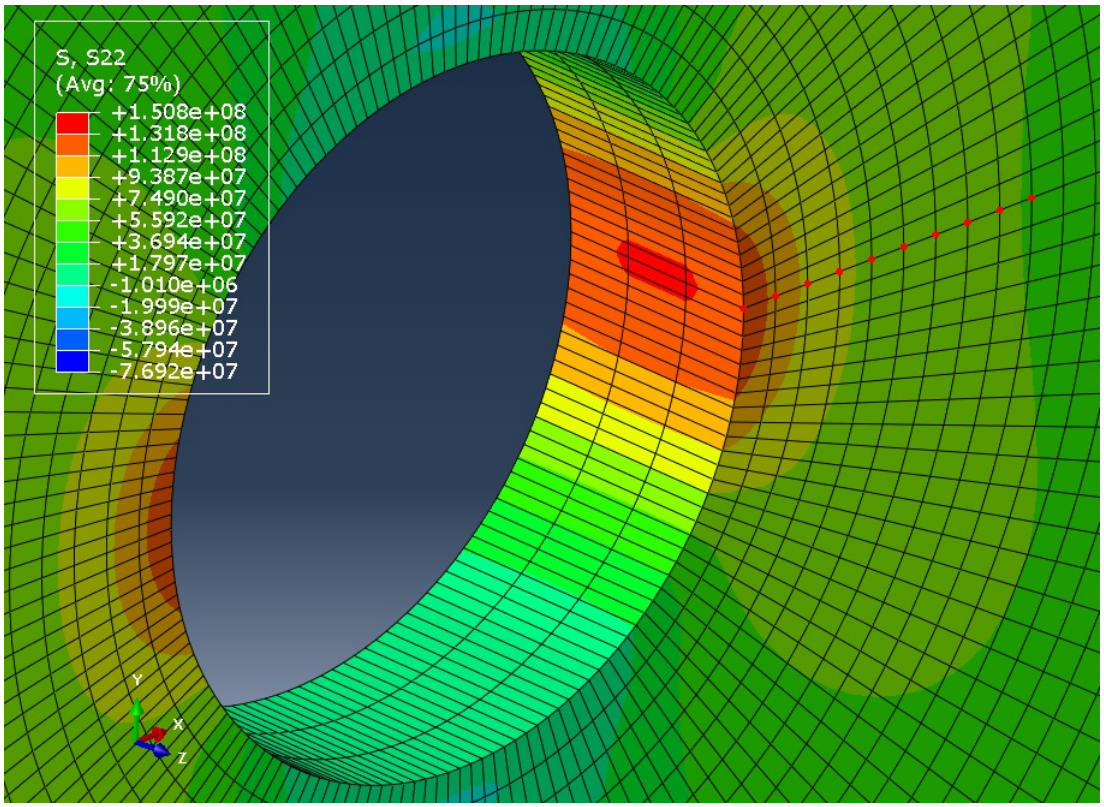


Figure 4.5. PLA dogbone model w/3mm hole S22 stress distribution

Data gathered from these models included the peak stress as well as the stress gradient in the vicinity of the central feature. After all of the dog bone specimens were modeled and tested, experimental and computational values were used to calculate κ as discussed previously in Section 2.5.1. As was previously mentioned, this material parameter is a function of Young's modulus, the stress gradient (calculated via modeling), and the failure stress (calculated from testing). A particular scenario was chosen from which κ was calculated. In this case it was the scenario with the 3mm hole in the center. The accuracy of κ is highly sensitive to the calculation of the stress gradient at the edge of the hole. For all of the scenarios listed here, due to prior experience with the various extrapolation methods as discussed in Section 2.5.1, a linear extrapolation technique was used. The subsequently calculated value of κ, along with a tensile modulus, E, of 2.33 GPa, was used for all later models.

4.2 PLA Test Results

As was pointed out previously in Section 4.1, PLA is generally considered a brittle material so even though the standard quasi-static tensile testing conducted here was sufficiently slow, the failure of PLA was believed to occur at a rate that necessitated high speed diagnostics in an attempt to capture the inception of failure. This was verified by early tests that showed a much more rapid and brittle type of failure. Owing to the rate of the testing and the observed failures, we initially believed that in order to capture the precise location and moment of failure, the velocity of which should be no higher than the longitudinal sound speed of PLA generally around $1800 - 2200\frac{m}{s^2}$ [88], [93], [94], the decision was made to use high speed digital imaging techniques. Two different Phantom cameras were used, one a V2512 model and the other a V2640. As a result, there were a number of differences including the lenses, apertures, lighting, and other settings that resulted in noticeable differences in the captured images. Because of initial concerns over rapid brittle failure, a behavior that we subsequently learned only manifested itself on samples printed on the Ultimaker printers and PLA, the V2512 camera was initially run at a framing rate of approximately 50 kfps over a 128x128 pixel area. Evidence of one such brittle failure can be seen in Figure 4.6. Failure of this nature did not occur exclusively however and as a result, the framing rate was reduced to only 20 kfps although even that lower framing rate turned out to be far more than was necessary.

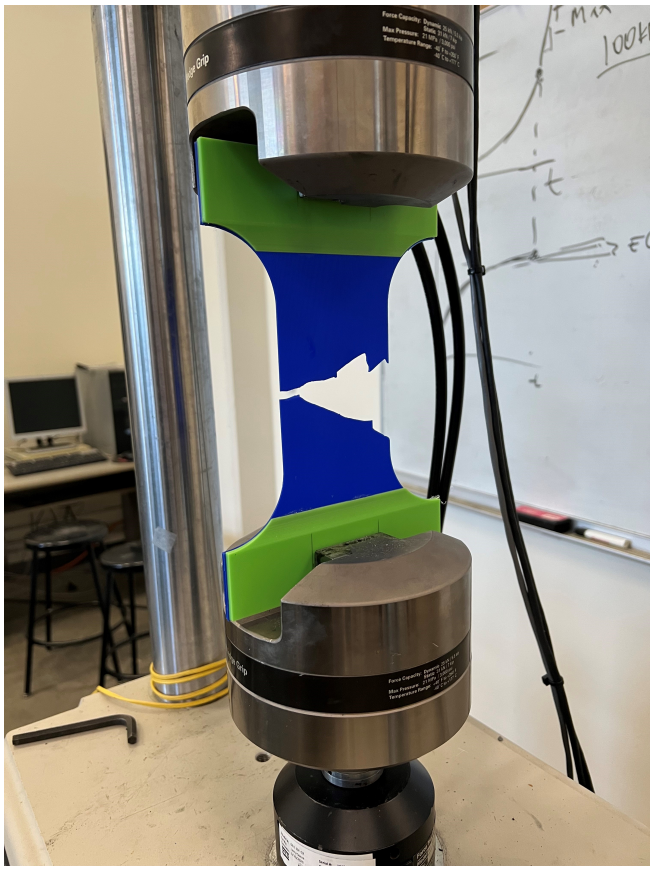


Figure 4.6. Brittle PLA tensile specimen failure

When considering illumination of the test specimen at high framing rates, it is necessary to use a powerful light source. This is due to the fact that at high framing rates, the short exposure duration does not allow sufficient light to impact the image sensor resulting in an overly dark image. If care is not taken with respect to the placement of high power incandescent lights near the test specimen however, and the specimens are relatively thin as they were here, appreciable thermal softening will occur. For this reason the distance between the lights and the test sample was maximized whenever possible, subjected to the constraint of sufficient intensity at or near the focal point, and the duration over which the lights were kept on was minimized. Whenever possible high intensity LED lights should be used but even they generate appreciable heat that needs to be minimized at the sample lest their use adversely influence experimental results.

When samples containing larger 6 and 10mm central holes, failure always originated from the edge of the hole. A typical example of this type and onset of failure can be seen in Figure 4.7.

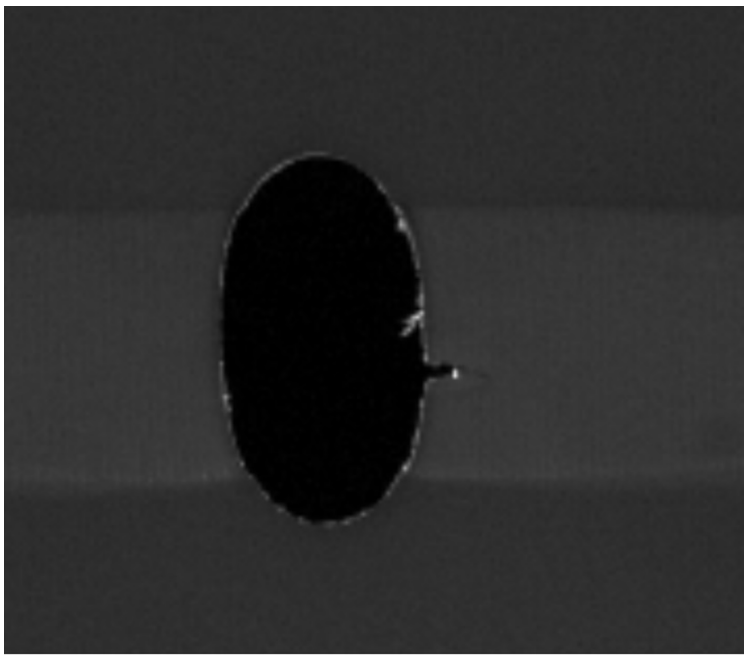


Figure 4.7. Typical failure initiation for a 6mm PLA hole

For the PLA samples created with smaller 3mm diameter holes however, failure occurred in a much different manner. For these specimens, failure consistently began some distance away from the edge of the hole. This is particularly interesting when considered in light of the UFC Equation 2.19. This component of the failure criterion states that in order for failure to occur, the effective stress σ_{eff} need only be greater than the cube root of the product of two material parameters, namely Young's modulus E and κ_{fail}, and the stress gradient in the direction of failure. In and of itself, Equation 2.19 does not explicitly predict that the location of failure should occur away from the edge of the hole. But why failure occurs at the edge of the hole or some distance into the sample away from the edge, and whether it might be predicted numerically, are questions that remain to be answered. An example of the inception and evolution of material failure can be seen in Figures 4.8 and 4.9.

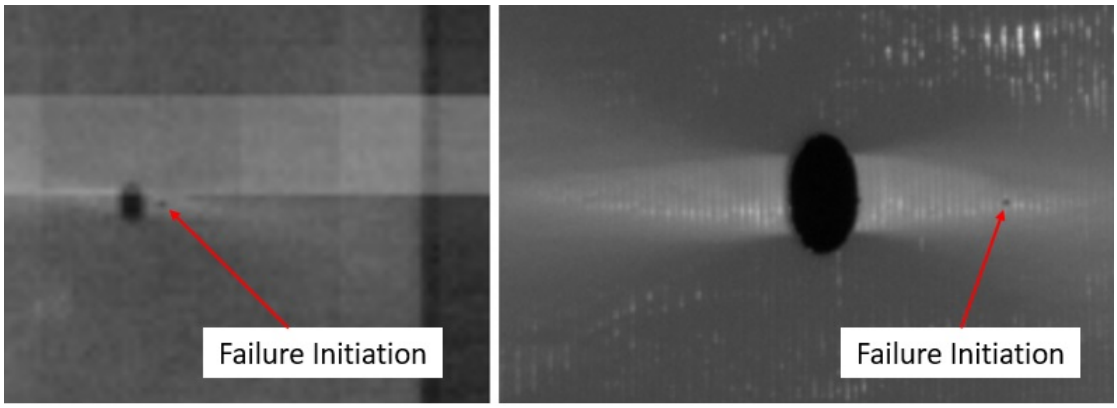


Figure 4.8. 3mm PLA hole damage away from the edge of the hole

Figure 4.9 shows the subsequent evolution of the hole shown on the right hand side of Figure 4.8.

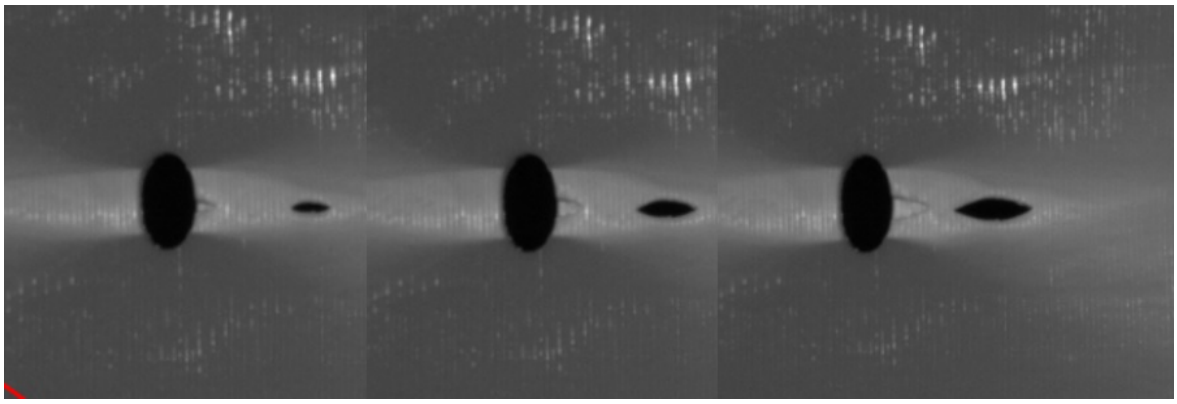


Figure 4.9. 3mm PLA hole evolution

Although the series of images in Figure 4.9 shows thinning of the PLA in the vicinity of the hole, the inception and propagation of true material failure manifests itself in a visible through hole that occurs some distance away from the edge of the centrally drilled hole. But why does failure occur some distance *remote* from the central feature for certain sized holes but yet it begins *at* the central feature for others and what, if anything, does the new UFC

predict about such a situation? Referring back to Equations 2.18 and 2.19 that comprise the UFC, and considering a specimen with a central feature, we can compare theoretical and experimental results.

Figure 4.10 contains several different pieces of data that describe the application of the UFC to the PLA tensile test specimens discussed here. The curve plotted in red for example, is the failure stress predicted from Equation 2.19, generated via Abaqus, otherwise referred to as the stress gradient condition. The blue curve is the equivalent or nominal stress that is the maximum normal stress and is generated from the nodal stress values in Abaqus. The straight black line is the failure stress predicted by Equation 2.18. All of these stresses are normalized by the failure strength of the material explaining why the failure stress occurs at a value of 1 while the others are much lower than the magnitudes of stresses that would occur were it not for this operation. Qualitatively however, their behavior appears correct as we anticipate that the failure stress should rise to a theoretical value close to 3 as was shown for the idealization of an infinite plate previously. All of these values are plotted against a distance from the hole edge that has been normalized by subtracting the hole diameter.

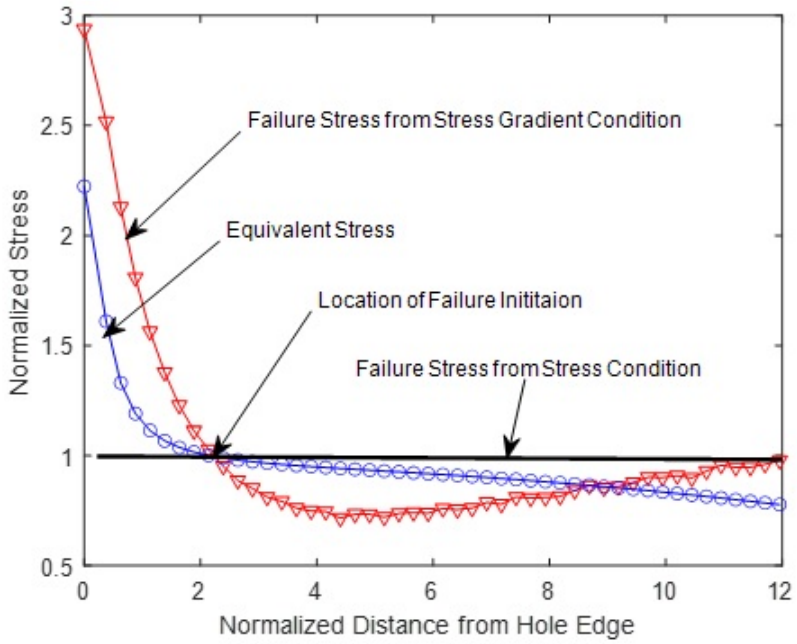


Figure 4.10. UFC conditions for a 3mm PLA hole Source: [95]

The key is that the stress that occurs along the direction of failure, i.e. the equivalent stress, must *simultaneously* satisfy both Equation 2.18 and 2.19. In Figure 4.10 to the left where the equivalent stress intersects the horizontal line that is simply a graphical representation the failure stress, although the stress is everywhere greater than that dictated by the failure stress as described by Equation 2.18, it does not, at the same time, satisfy Equation 2.19 as it is clearly not greater than or equal to the failure stress required by the stress gradient condition. To the right of the labeled location of failure it does not satisfy the first condition as it is lower than the normalized failure stress. The only location at which it satisfies both conditions simultaneously is at its intersection with the normalized failure stress line and the curve generated by the normalized stress gradient. This varies somewhat from numerical predictions that showed that failure should occur approximately 6mm away from the edge of the hole. Those predictions agreed closely with those seen experimentally as shown in Figure 4.9. If one considers the case where the hole size becomes even smaller it is easy to see that this would cause a shift in both the equivalent stress as well as the

failure stress resulting from the use of the stress gradient condition. If the values of these functions changed at even slightly different rates with respect to one another then it is easy to imagine that they would no longer intersect as they shifted left. Without an intersection to simultaneously satisfy both conditions, it would be as if a small hole appeared to the failure of the sample as if there were no hole at all despite the fact that from theory we would anticipate that the stress at the edge, i.e. the stress concentration factor, tends to an ever increasing number. Not surprisingly, there are differences that result when the hole size moves in the other direction as well. An example of how the UFC applies to predicting the failure of a PLA tensile test specimen with a larger 6mm sized hole is shown in Figure 4.11.

In this scenario plotting the same values yields the plot shown in Figure 4.11 with a few key differences. Although the equivalent stress is close to equaling the failure stress generated by the stress gradient condition, it no longer does so at the intersection of the normalized failure stress and the stress gradient condition. For this scenario however, the only location where the failure stress simultaneously satisfies both equations is at the edge of the hole.

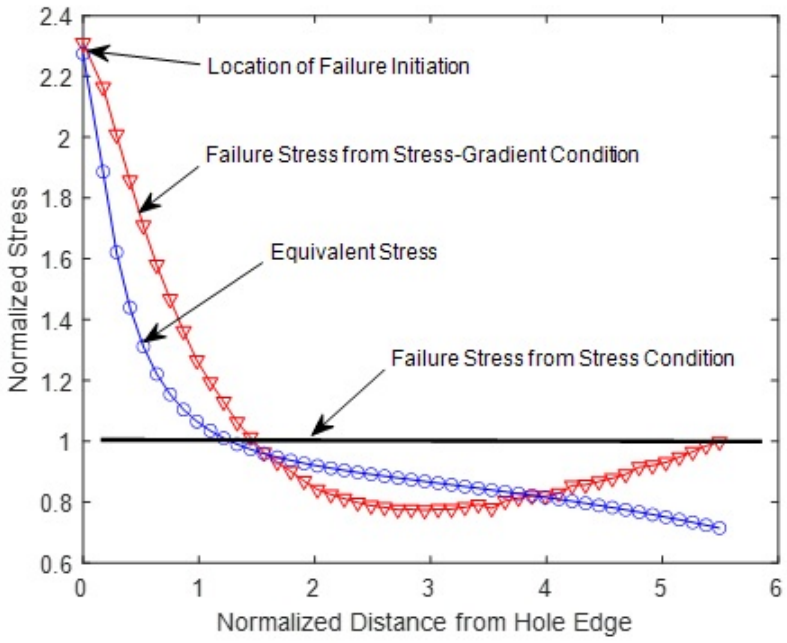


Figure 4.11. UFC conditions for a 6mm PLA hole Source: [95]

This is exactly what was seen experimentally for all hole sizes larger than 3mm. An example of failure initiating at the edge of the hole is shown in Figure 4.7.

The plots shown in Figure 4.10 and 4.11 are simply graphical representations of the UFC as described by Equations 2.18 and 2.19. The explanation of the plotted stresses correlates well with the captured video images of the onset of failure. If the newly developed UFC model did not accurately describe the locations of failure captured with HSV then some differences in the previous plots would necessary. This therefore means that the newly developed model accurately describes the type of failures seen in the PLA specimens tested here. Perhaps somewhat surprising however, is that the theory works as well as it does for specimens which did not behave in as a brittle manner as anticipated. Although it is possible that there is a region of failure, strain rate, material, etc. outside of which this model accurately applies, given the conditions tested here the models predictions agree remarkably well with experimental data and as a result, it offers a most plausible explanation for the location of incipient failure.

4.3 CFC Sample Preparation

To determine if the UFC would produce accurate results when applied to more complicated, non homogeneous CFC, additional materials were tested in tension. The CFC tensile test specimens consisted of carbon fiber filament impregnated polymer produced by Allred & Associates known as DragonPlate ™. A number of different geometric samples were produced, all of which were cut using a waterjet cutting machine and all of which resulted in at least slight inaccuracies in the accuracy of the "feature" geometry like those described by Section 3.1.1. A list of sample geometries that were modeled and tested is shown in Table 4.2. Both sets of quasi-isotropic (QI) and the cross ply (CP) samples measured 24mm x 140mm x 1.8mm. Generally, QI means that the properties of a material within a plane are such that the overall sample has identical properties in all directions (of the plane of the composite). This requires a series of alternating layers of $0, 90, \pm 45°$ orientations. The QI samples here were not truly QI but for the purposes here, they will be referred to as such.

Table 4.2. CFC Test specimen geometry

Sample	Layup	Feature (mm)
1	QI, CP	3mm circular hole
2	QI, CP	6mm circular hole
3	QI	8mm circular hole
4	CP	9mm circular hole
5	QI, CP	0 ° elliptical slot
6	QI, CP	15 ° elliptical slot
7	QI, CP	30 ° elliptical slot
8	QI, CP	45 ° elliptical slot
9	QI, CP	0 ° short horizontal slot
10	QI, CP	0 ° long horizontal slot

Like the homogeneous, isotropic PMMA samples tested previously, all CFC samples were prepared using a waterjet cutting machine. Similar anisotropic behavior has been observed even for some homogeneous materials like PLA parts printed via FDM. Anisotropy of FDM printed parts like PLA are apparently the result of the print orientation and material as well as a combination of the two [87], [96], [97]. Fortunately it was possible to investigate a number of these factors owing to the wide variety of CFC sheet available from a number of commercial vendors in addition to our ability to generally locally printed PLA parts. Three specific orientations were used including unidirectional, quasi-isotropic, and cross ply fiber orientations. All samples were approximately 1.8 mm thick and used NCT 3-4-1 resin with UTS 700 fiber at a 55% fiber volume. Table 4.3 lists the orientation and number of lamina for the CFC samples, all of which were approximately 1.8mm thick.

Table 4.3. DragonPlate CFC specifications

Sample Type	Orientations	No. of Lamina
CrossPly	$(90/0/90)_S$	6
Quasi-Isotropic	$(90/0/45/-45/90/0)_S$	12

From examination of the different lamina orientations for the QI layup it worth noting that what is ordinarily referred to as quasi-isotropic is different from the lamina orientations shown here.

Like the PMMA samples tested previously, it was necessary to add tabs to the PLA Because of consistency, availability, cost, and ease of machineability, samples were cut from larger 12 in x 12 in DragonPlate sheets. As a result of logistical factors related to machining these samples, two different lots were prepared at two disparate locations using different waterjet parameters. Although both sets of samples were printed using standard solid model part file formats, one process used a more traditional garnet media with lower pressures (approximately 20 ksi) while the other, out of expediency and lack of media, used a higher pressure without any media. Unfortunately the latter process produced an appreciable amount of delamination in the vicinity of any internal features and as a result, was unusable for any samples containing circular or elliptical holes. An example of this is shown in Figure 4.12.

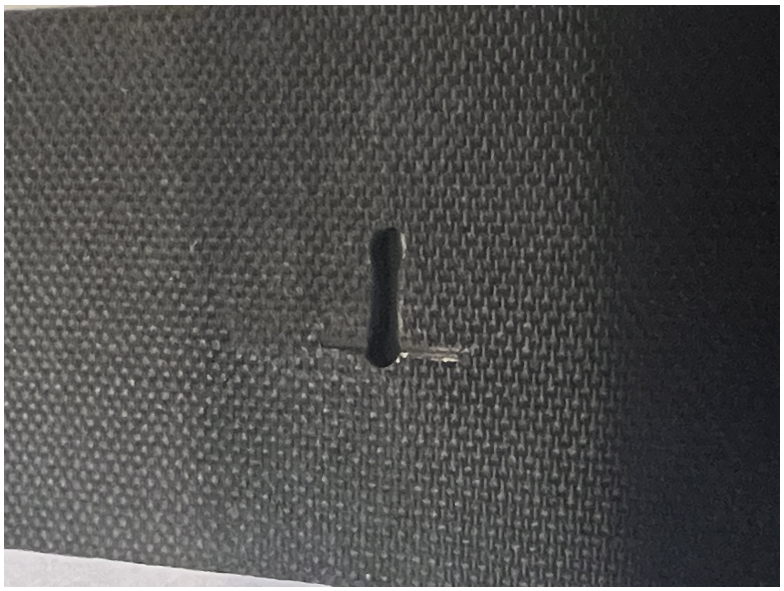


Figure 4.12. Waterjet induced delamination in CFC

4.3.1 Instron Testing

All CFC samples were tested in the Instron machine. Unlike the previous PLA dog bones, the narrower sample widths were all less than the test machine jaw widths so that symmetrically gripping the samples was possible even when there was a backing plate on the grips. The layups for both the QI and CP test samples was shown in Table 4.3 previously. The average specimen failure loads of three test samples per layup per hole size are listed in Table 4.4

Table 4.4. CFC failure loads and stresses

Sample Type	Interior Hole (mm)	Failure Load (kN)	Failure Stress (MPa)
CP	3	19.2	445
CP	6	17.3	400
CP	9	14.1	327
QI	3	24.3	562
QI	6	19.9	460
QI	8	16.7	387
QI	9	16.4	380

4.4 Modeling Setup and Methods

Modeling a composite sample requires appreciably more input and effort than that of modeling an isotropic, homogeneous material like PMMA. Depending on the ultimate goal of the model, Abaqus points out that there are at least 5 different methods of modeling composite based structures [98]. These include microscopic modeling where the fiber or particle and matrix are explicitly accounted for and are modeled separately. Although possible for at least small sections of a structure, modeling a composite to this level of detail is not commonly done owing to a variety of factors not the least of which is its high computational cost.

Another technique is that of macroscopic modeling where the composite is homogenized and the fiber and matrix properties are smeared across the model as if it were a single homogeneous and orthotropic material, or even an anisotropic, homogeneous material. The third type of composite modeling is a laminate model wherein each layer of the composite is accounted for discretely. These layers may have different thicknesses and fiber orientations such that the overall laminate is effectively a homogenization of the individual lamina. This type of model is typically useful where accurate physical behavior can be captured using

shell elements. The fourth type consists of the modeling of discrete reinforcements such that the reinforcing aspects of the composite are considered explicitly and the interface between the reinforcement and the matrix is considered an ideal, fully bonded connection and the last type of model consists of submodeling where the mesh may be highly locally defined based on the particular scenario. This capability is useful when more accurate results are desired in a region that is a subset of the greater model but does not have any appreciable effect on the overall solution. This is necessary when one desires to study, for example, the stress state around reinforcement fibers of a composite. These different models are generally used in an attempt to model macroscopic behaviors such as damage and structural failure.

Due to the various complexities and relative value of each technique only the homogenization modeling technique will be discussed here. In this manner the various engineering constants relevant to anisotropic elasticity were introduced to account for accurate material behavior. Although this technique is both simple and efficient, the homogenization modeling technique can be enhanced through the use of multiscale or multi-length scale modeling that produces a behavior at the microscopic scale to be used to predict behavior in the macroscopic regime. This will be discussed at greater length in the section on multi-length scale modeling.

4.4.1 Homogenization

The simplest method of modeling a composite specimen was through the use of what is generally referred to as "homogenization" or macroscopic modeling. This is where the properties of the individual fiber bundles and matrix are generated in aggregate or smeared out so that there is no distinction from one layer to the next and no treatment of the nature that gives heterogeneous composites their unique structure and properties. When modeled in this manner it is as if the CFC is comprised of a single continuous material without any individual lamina. On some level, e.g. consideration of the preferential failure of a particular layer, this has much less physical accuracy than the actual heterogeneous specimens. As a result, using the homogenized or macroscopic method results in an inability to predict the failure stress in the individual laminae let alone the fibers or matrix. Although it may not be representative of the real mechanics of failure, smearing or homogenizing the material properties in this manner is still a useful technique for predicting the overall behavior of a composite structure or component, albeit one with a much lower computational cost than might otherwise be incurred.

Because the composite was modeled as a homogeneous macroscopic model with symmetric geometry, loads, and boundary conditions, quarter symmetry could have been utilized to accurately predict the overall response. Because the problem was reasonably small however, in order to remove any concerns over issues arising from symmetry, the full model was used. Owing to the nature of the geometry, all of these model comprised of approximately 200k S4R shell elements was generated with a smaller central region having a more dense swept mesh in a circular partition ranging from 2 to 4 times the radius of the central hole. Like the work on PMMA cited previously in Section 3.1.2, 8 cores were used with full nodal precision. Similarly, a non biased swept mesh was used in the vicinity of the hole because it made the calculated gradient smoother than it would otherwise be had a more biased mesh been used. This made subsequent analyses more accurate as a result of not introducing sensitivity from the numerical differentiation process

The elastic lamina option was used to define the structure of the necessary material properties. The lamina type of elastic model is meant to accurately model plane stress scenarios by simulating the material as orthotropic. Had a composite layup been used instead, the individual lamina would have been modeled as orthotropic layers so using this type of elastic input was deemed to be a logical conclusion in attempting to model overall behavior. This approach necessitated different values however, based on orientation of the lamina that compose the laminate structure. Because two different types of laminates were tested, i.e. QI and CP, different material properties were provided to accurately simulate them under tensile test conditions. In order to generate a single set of homogenized properties in this manner, composite lamination theory was used. This technique, used previously by Kwon et al [15], provides a way to generate a single set of properties through the use of the following equation

$$[\overline{D}] = \sum_{i=1}^{n} [D]_i \frac{(z_{i+1} - z_i)}{h} \tag{4.1}$$

where there are n layers, D_i is the i-th layer stiffness matrix, and z is the coordinate value in the thickness direction. The coordinate values of the top and bottom layers are represented by $z_i = z_1$ and $z_{i+1} = z_n$ respectively while h is the total specimen thickness. Applying this method results in the values collected in Table 4.5.

Table 4.5. CP and QI CFC properties

	$E_1(GPa)$	$E_2(GPa)$	ν_{12}	$G_{12}(GPa)$	$G_{13}(GPa)$	$G_{23}(GPa)$
CP	65.12	55.56	.0278	2.89	2.89	2.89
QI	51.54	51.54	.2015	1.173	1.173	1.173

In order to determine the accuracy of the UFC in predicting the failure of CFC test specimens, it was necessary to compare the failure stress predicted experimentally with that predicted using the two UFC conditions. As discussed previously in 3.1.2, κ_{fail} is a material property that has to be calculated from a composition of modeling and testing. Using Equation 2.19 to generate the stress gradient extrapolated back to the hole edge, and using the value of σ_{fail} determined experimentally provides a way to solve for $\overline{\kappa}_{fail}$. This requires that $\overline{\kappa}_{fail}$ be calculated once for each layup. While that is perfectly easy to do for samples as simple as the ones tested here, for real world scenarios that is simply an intractable approach. A corollary of this is that because one experimental data point must be used in order to generate this value, it matches exactly with that scenario but lies within some range of variability for the others. This can be seen in Figure 4.13.

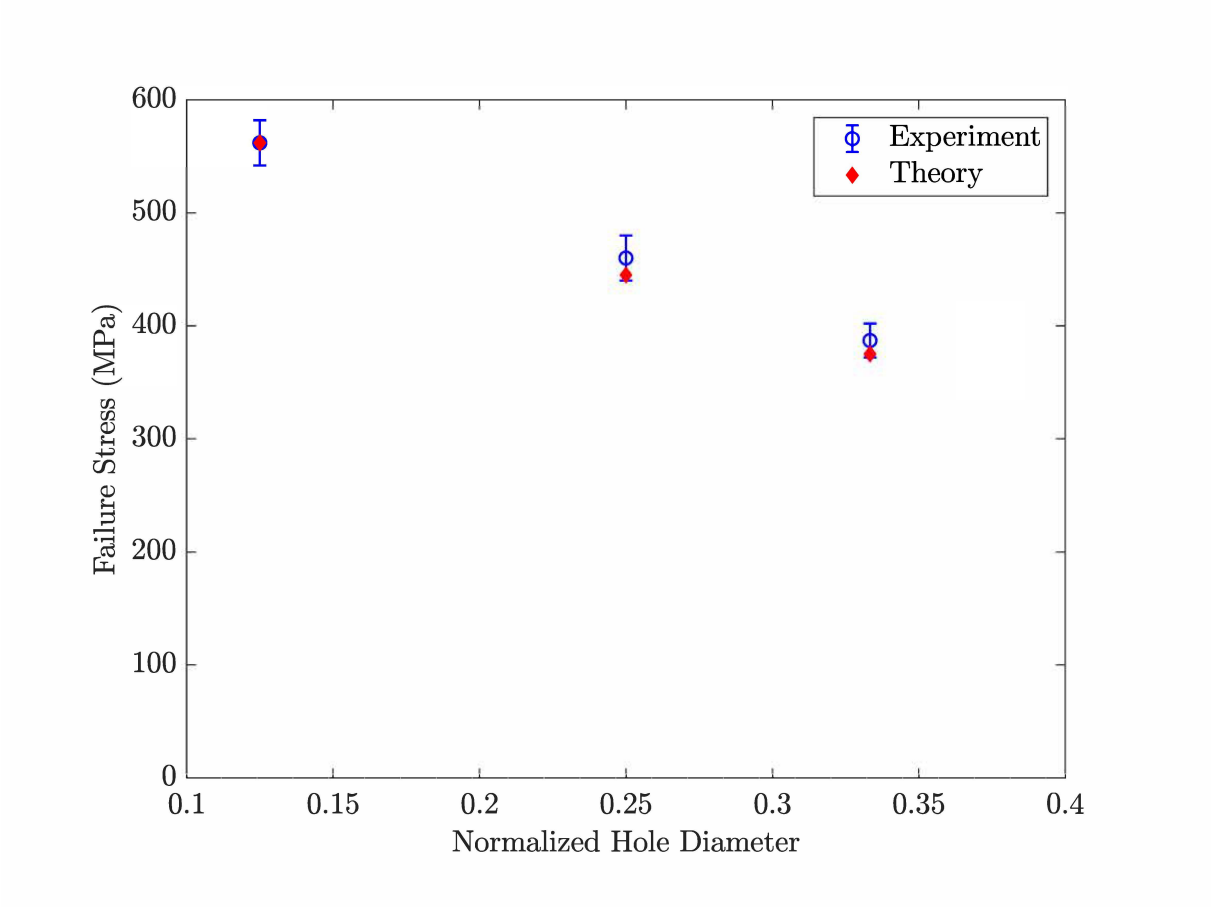


Figure 4.13. Comparison of UFC with QI experimental data

The data in Figure 4.13 are the mean failure stresses, with standard deviations, for the QI samples with discrete hole sizes measuring 3,6, and 8 mm in diameter as was shown previously in Table 4.4. Those hole sizes were normalized by the specimen width which is why the scale of the abscissa has no units. As discussed previously, the data point used for the calculation of κ_{fail} was the 3mm diameter case so that is why the agreement between the failure stress experimental and theoretical, i.e. UFC theories is in perfect agreement. For all the other data points however the agreement is similar although not perfect. It does however lie within the error bands of all the tests so it agrees extremely well with experimental data. Similar data for the CP specimens can be seen in Figure 4.14.

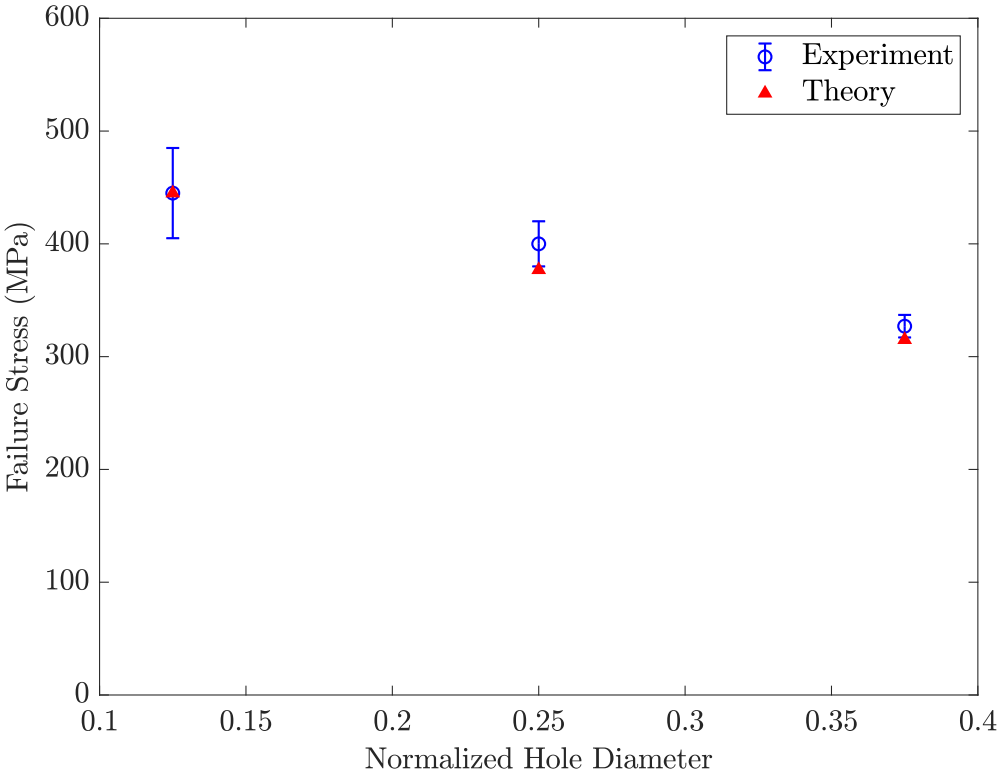


Figure 4.14. Comparison of UFC with CP experimental data Source: [95]

It is important to note the close agreement not only with the QI specimens but with the CP ones as noted in the previous discussion. The strengths of these materials the their overall behaviors are measurably different and despite that fact the UFC predictions of failure stress through a combination of both equations seems to be reasonably correct.

4.4.2 Multi length Scale Modeling

Ordinarily a wide variety of extremely complex material behavior can be simulated using the breadth of models available to the Abaqus user. Some of these have already been discussed and include linear elastic behavior as well as orthotropic and even anisotropic models each

of which necessities a unique material definition or combination of material properties. There are however limitations to what the models are capable of predicting. In modeling CFCs for example, predicting failure at the constituent level, i.e. at the fiber and matrix, is not possible so there are situations where existing models are insufficient predict certain aspects of material behavior in all conditions. Fortunately Daussault understood this and made it possible for users to write their own material definitions describing unique and different potential behaviors far from what was initially envisioned. This is the purpose of the user material (UMAT) used here.

One of the goals of using a UMAT is to address a fundamental shortcoming of the previous homogenization modeling technique. In order to accurately apply that technique to the breadth of composite layups, a test using a specimen having the same fiber composition and orientation must be tested. This suffers from a practical limitation of being overly narrow in application and as a result, it is prohibitively expensive and time consuming given the range of fiber composition and orientations. A much more broadly applicable modelling approach would be desirable if its accuracy were at least approximately as good. That is the goal of this multi length scale modeling effort

This approach is an attempt to implicitly account for the results that occur when modeling different composites containing different fiber and matrix orientations or materials. The fibers and matrix are generalized for example, in a unit cell or RVE with a representation of their properties including voids, fiber type and orientation, and matrix composition in a collection of subcells. A necessary assumption is that of the uniformity of stress and strain within each individual subcell as well as subcell to subcell deformation compatibility. Figure 4.15 is an example of this type of structure.

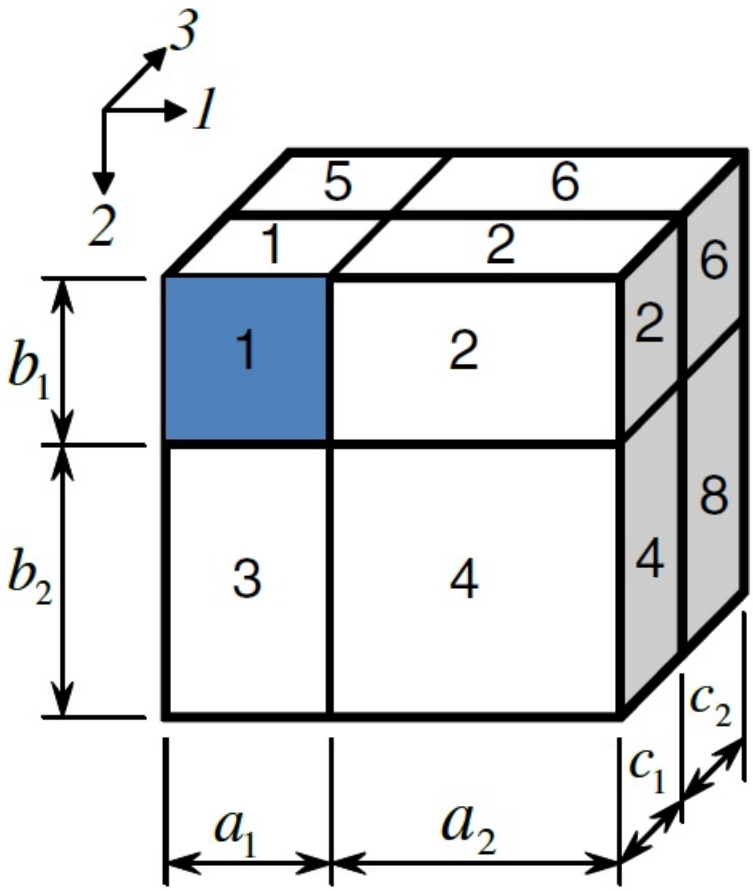


Figure 4.15. Micromechanics unit-cell model Source: [99]

This allows for accurate simulation of properties and behavior of the constituents at the micro level without having to suffer the tremendous computational expense of modeling them explicitly. This approach is implemented through the use of an Abaqus UMAT. This model, the development of which was previously described in [23], [24], [72], not only predicts failure at the fiber or "micro" level but through the user defined routine feeds failure information up to the composite or "macro" level for the purposes of developing the most broadly applicable, and hopefully accurate, predictions of macroscopic failure influenced by damage and failure where it physically occurs, on the constituents at the micro level. This behavior is not one directional however and as the problem runs out in time, data is

continually transferred back and forth in an iterative cycle of transferring information from stress, strain, and damage at the constituent level up to the greater lamina or macro-level. Similar data from this higher level is subsequently feed back to the constituent level and provides an opportunity for modification of micro level properties based on system or macro level stress, strain, and damage. The communication of this information back and forth, to and from the various levels is known as *upscaling* and *downscaling*. The connection or link between the two scales is through what is referred to as a unit cell or RVE.

The UMAT model used here was developed by previous researchers [25], [72], [99], [99]. It uses a custom Fortran file with a set of 37 different variables generated in the ordinary process of running an implicit Abaqus analysis. This file performs a variety of functions including upscaling, damage detection, strength reduction, and downscaling as it couples with an otherwise ordinary Abaqus calculation. Some of those variables need to be defined by the user and some of them are passed into the function. There are 15 user input material variables in the form of "mechanical constants" and ultimately this routine generates 58 solution dependent state variables that it stores in the STATEV array and uses throughout the calculations.

Like the homogenization technique demonstrated previously, the test of how well the UMAT predicts brittle, composite, failure necessitates a comparison with previous experimental data like what was shown in Figures 4.13 and 4.14. An important point to remember is that the goal for this model is a more broad applicability without the need for testing so the degree of success will depend equally on accuracy as well as applicability. The latter of these two requirements would, for example, allow accurate predictions of both QI and CP behavior based only a single test that quantifies the unidirectional fiber properties. The UMAT would then transform those values to the appropriate directions and composition to represent the different lamina without having to conduct any additional testing and would within reason, accurately predict similar results to those shown previously using the homogenization technique. An additional feature that this model offers that the previous homogenization technique does not is the ability to predict failure at the fiber level.

Predicting failure at the fiber level requires experimental data capturing failure stress at the laminate level, computationally derived failure stress for a smaller section of material, and knowledge of the fiber stress. Doing so allows one to calculate an "experimental" value for

the fiber failure stress. After this data has been gathered, the UFC was applied at the fiber level, to calculate the stress gradient in the fibers, with the known material parameters E and κ_{fail} in the form of

$$\sigma_{fail,fiber} = (\kappa_{fail,fiber}|\frac{d\sigma}{ds}|)^{(1/3)} \tag{4.2}$$

When that is done it is possible to measure the error in the predicted fiber failure strengths using the UFC. The results for both QI and CP fiber failure predictions using this method are shown in Table 4.6.

Table 4.6. Unidirectional CFC sample tests

Layup	Hole Diameter (mm)	Fiber σ_{fail} (MPa)	UFC σ_{fail} (MPa)	% error
QI	3	8252	7892	-4.35
QI	6	7251	6689	-7.76
QI	8	6593	6145	-6.79
CP	3	8252	10030	22.10
CP	6	7251	10144	3.51
CP	9	6593	9088	4.22

A few points are immediately clear upon examination of this data. The first is that the difference between the UFC generated prediction for fiber failure and that which was experimentally measured, columns 4 and 3 respectively, agree with less than 7% error but only for the QI specimens. These values are well within variation that would likely be explained by ordinary experimental error given that there is a range over which the fibers fail during the experiment. The second thing that you notice is that in general the values for the predicted % error of the cross ply layup are also very good being within less than 5% error for the two larger diameter holes. The one exception that results is that of the smallest 3mm diameter hole that has a surprisingly large 22% error. As the calculation of

fiber failure stress is based exclusively on the material parameter κ and the computationally derived stress gradient $\frac{d\sigma}{ds}$ those are two potential sources of error that could account for this large value. If κ itself were the source of this error however, then you would expect to see larger errors across the spread of hole diameters but because this occurs only for the 3mm hole scenario, it is unlikely to be the cause of that error.

Another potential source of this error was experienced previously during the modeling of HCP discussed in Section 3.2. Like concrete, CFC also has a strength that can be statistical in nature. This results in a similar reduction in composite strength when longer fibers are present owing to the fact that the probability of the fibers having defects is to some degree, proportional to their length. In other words, longer fibers are more likely to have strength lowering defects than shorter ones.

Unfortunately at the time of this writing it was impossible to narrow the cause for this large value down any further so further investigation is warranted. It is clear however, that in general, for the simulation and prediction of failure of most QI scenarios and for all CP ones included here, the UFC applied here gives results accurate to within less than 8% error. This has been shown to apply to prediction of failure at both the fiber and composite levels for all anisotropic specimens tested to date.

THIS PAGE INTENTIONALLY LEFT BLANK

CHAPTER 5:
High Strain Rate Modeling and Testing

Heretofore all of the presented modeling and testing focused on interrogating the new UFC for the prediction of failure that occurs during conditions represented by ordinary, quasi-static, strain rates of about $10^{-2}s^{-1}$ or slower. The question of whether or not the UFC model might also be used to accurately predict the failure of specimens subjected to higher rate, dynamic loading is the subject of the work described here.

Figure 5.1 is an example of the conditions and experimental instruments necessary to reach the variety of relevant strain rates.

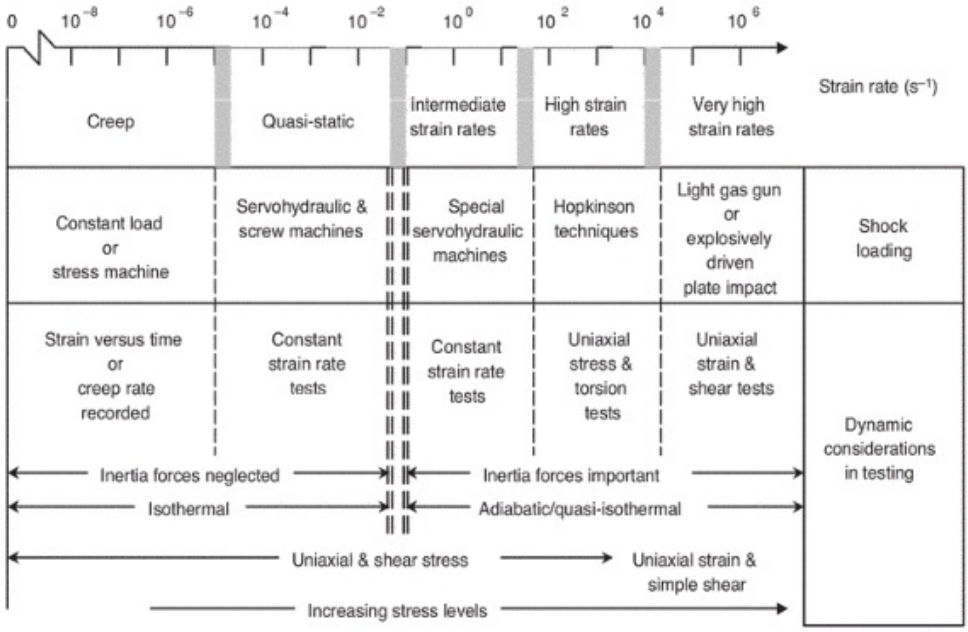


Figure 5.1. Strain rate spectrum Source: [100]

The apparatus necessary to reach the different orders of magnitude of strain rate are appreciably different. Similarly, the modeling techniques and the failure modes themselves

also change significantly with strain rate. The change from standard quasi-static FEM to dynamic modeling for example, requires the consideration of a variety of aspects including element choice, time step, and material properties among other factors if the inertial effects associated with higher rate modeling are to be accurately accounted for. It is important to point out that with respect to the work presented in this chapter, the focus will be on modeling the behavior and predicting the failure of CFC subjected to what Figure 5.1 refers to as the "high" to "very high" strain rate regimes.

The variation in the different types of behavior that occur as a function of strain rate is true not only for metals but it is also particularly true for the more complicated scenario of the dynamic loading of heterogeneous, anisotropic, composites [101]–[109]. Although there are a variety of methods that will allow testing into the highest strain rate regimes including propellant and gas guns as well as flyer plate experiments, the two which were included here include the split Hopkinson pressure bar (SHPB) and explosive loading. These were used to attain strain rates in the range of $8 * 10^3 s^{-1}$ up to a maximum of about $1 * 10^5 s^{-1}$ for SHPB and explosive testing respectively. It is important to point out that the composite and the layups used for the SHPB testing were different than those that were explosively tested. The fiber and matrix materials with corresponding fiber values are listed in Table 5.1.

Table 5.1. SHPB and explosive test sample CFC properties

CFC	Fiber	Fiber Tensile Strength (MPa)	Matrix
DragonPlate	UTS 700	1400	NCT 304-1
Touray	UTS 4900	4900	UF 3325

The DragonPlate uses the same fibers so the compressive strength has been listed. It otherwise has the same tensile strength as the Touray composite. The DragonPlate was comprised of 6 unidirectional layers while the cylindrical samples were comprised of $(\pm 85°, \pm 85° \pm 45° \pm 85°, \pm 85° \pm 45°)$ layers of a TCR composite described in Section 5.4.

5.1 Background

The SHPB, also known as a Kolsky bar, has a long history for use in testing the high strain rate response of a variety of materials. First developed by Hopkinson circa 1914 the apparatus has undergone several modifications to resemble the test device that it is today [110]–[114]. SHPBs, a schematic of which can be seen in Figure 5.1, are commonly used to characterize material behavior up to strain rates of approximately $10^4 s^{-1}$ dependent on sample size.

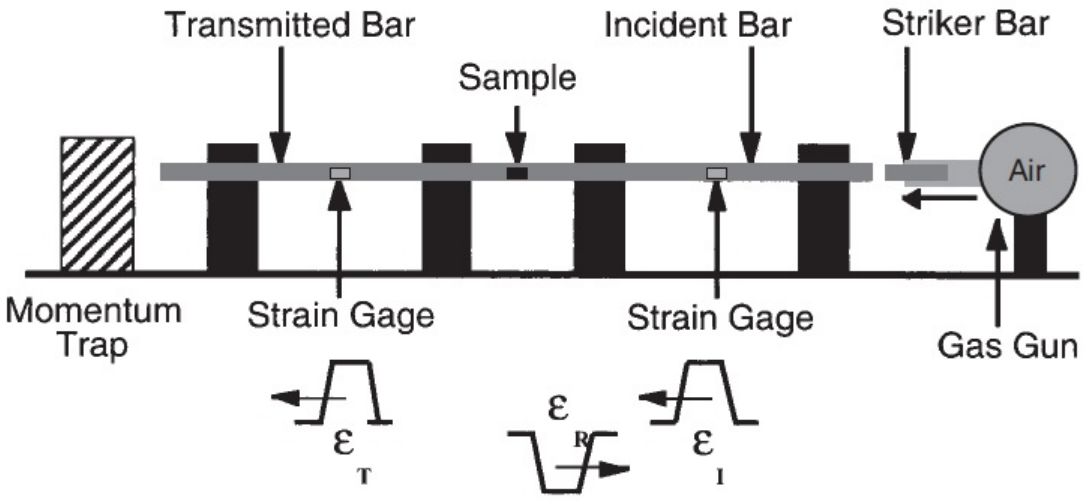


Figure 5.2. SHPB schematic Source: [110]

Although a wide variety of test parameters can be interrogated using this apparatus, including compression, tension, torsion, combined loading, and elevated or reduced temperature testing, this work only focuses on compression and tension testing of anisotropic materials, specifically CFCs, for the purpose of comparing failure to that predicted by the UFC to see if good agreement occurs between the theory and experiment.

Regardless of the nature of the SHPB test, i.e. whether it is tensile or compressive, the principles by which it operates are identical. Using the compression test as an example, a striker bar is propelled, typically by compressed air operating at approximately 15-100 psi, to impact an incident or sometimes referred to as an *input* bar. These bars composition and

diameters are chosen so that their strength will exceed the imparted stress wave prohibiting the possibility of them deforming plastically, and so that the duration and quality of the imparted stress wave sufficient to ensure a one-dimensional wave propagation. Small copper discs, commonly referred to as wave or pulse shapers and are only .051 cm thick, were used between the striker and transmission bars to smooth out the rise time of the incident stress wave. Although this is not strictly necessary, it is commonly done. Between the incident and transmission, or *output* bar, is where the sample of interest is "captured."

Upon being impacted by the striker, an elastic pulse travels down the length of the incident bar where it impacts the specimen. Owing to the nature of stress wave propagation, upon impact with a specimen of differing impedance, an elastic wave is reflected back down the incident bar while another is transmitted through the sample and into the transmission bar. When the wave transiting the sample hits the transmission bar, it to is reflected back into the sample and another wave is transmitted into the output bar. The now left going reflected wave in the sample hits the interface between the sample and the incident bar and the process of reflecting a series of waves back and forth in the sample of sets up a high enough stress level within the specimen to induce compression. This is true as long as certain conditions are satisfied, namely that the strength of the sample is sufficiently lower than that of the incident and transmission bars and appreciably large plastic deformation can be induced in the test article. This deformation is most often, at least for brittle materials such as CFC, sufficient to completely destroy the test sample. Strain gauges on the incident and transmission bars measure the reflected and transmitted pulses, i.e. ϵ_r and ϵ_t respectively. It is these measured values of reflected and transmitted strain that it is possible to calculate the stress, strain rate, and strain that occurs in the sample [115]–[117]. Ordinarily you might conduct high rate testing using a SHPB in order to quantify the stress strain response of a material at a high strain rate as it will likely differ appreciably from that experienced at quasi-static rates. In this case however, the SHPB was used solely for the purpose of determining strain rate sensitivity of the composite.

5.2 SHPB Test Sample Preparation

Two sets of SHPB samples were tested, one QI and the other was unidirectional. The layup of the QI specimens was described previously in Table 4.3. It was anticipated that no discernible

difference would be noted for the QI case but because of the orientation, it was believed that testing a unidirectional configuration would result in noticeable differences. Even though it was unidirectional, this laminate was comprised of 6 layers of unidirectional oriented plies and the hope was that it would be possible to see the differences that result when the transmitted stress occurred both parallel and perpendicular to the fiber orientation. In theory this should result in the measurement of appreciably different failure loads measured as a result of the differences in transmitted and reflected pulses owing to the different sound speeds of the fibers and the matrix. Unlike many SHPB tests that use cylindrical samples, rectangular rather than axisymmetric cylindrical specimens without any loss of accuracy [114], [118]. Fortunately the same Dragonplate sheets used for previous quasi-static testing could be used to provide media for these specimens. The sample size however, needed to be small in order to ensure the fundamental requirement of stress equilibrium that is particularly pronounced given the minimal number of wave reflections necessary for a valid test as the time it takes for that to occur depends on the softness of the polymer matrix as well as that of the relatively stiff carbon fibers. Two different orientations were tested using the same sample sizes of 1mm x 2mm x 3mm. For the QI tests, the 3mm direction was parallel to the axis of transmission but for the unidirectional samples, the 1mm direction was oriented parallel to the axis of transmission as shown in Figure 5.3.

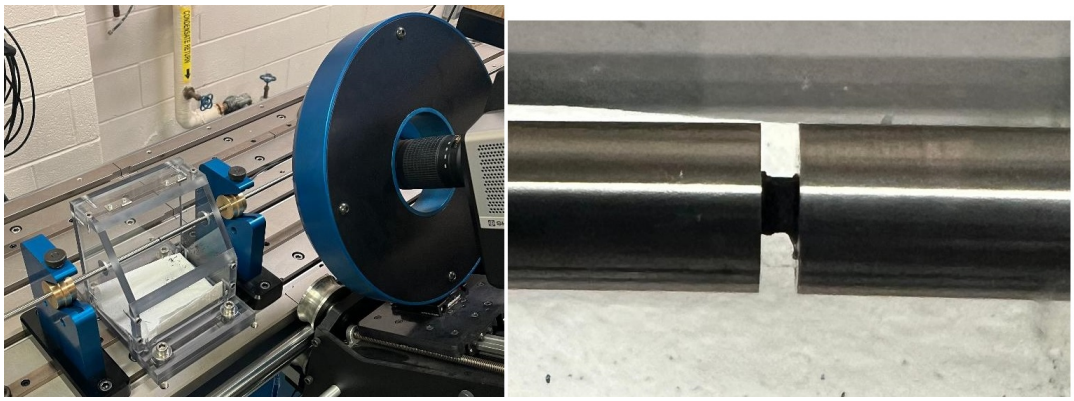


Figure 5.3. SHPB setup with closeup sample view

The best way to manufacture samples of such a small size was to cut them from the larger sheet using the waterjet cutting machines as described previously in Section 4.3. An example

of how they were prepared can be seen in Figure 5.4

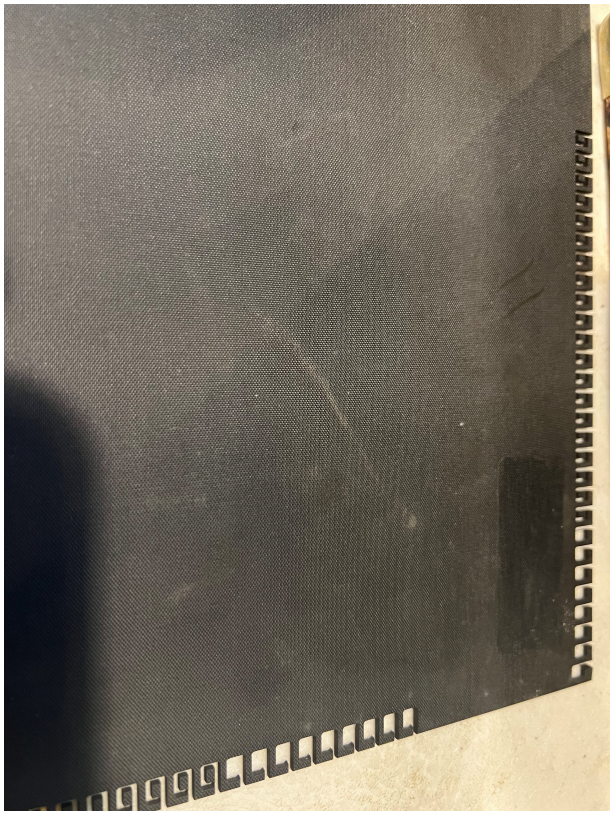


Figure 5.4. Waterjet cut SHPB test samples

The test samples are the small hanging pieces on the edge of the large plate. A small amount of additional material was left on the sample after separation from the larger sheet, but owing to the orientation of the sample during testing, this was not believed to have any impact on testing so no effort to sand the sample down was undertaken. Since the sheet was unidirectional, one set of samples would find the fibers parallel to the direction of the stress pulse and for the other, the fibers would be perpendicular to the direction of loading. Clearly the strength was anticipated to be much lower in the direction parallel to the fibers given that the transverse properties of both the matrix and the fibers would play a greater role in the overall specimen response.

5.3 SHPB Test Results

Not surprisingly, testing resulted in the complete destruction of all CFC samples. Figure 5.5 shows a series of snapshots from a high speed video taken at approximately 460k fps.

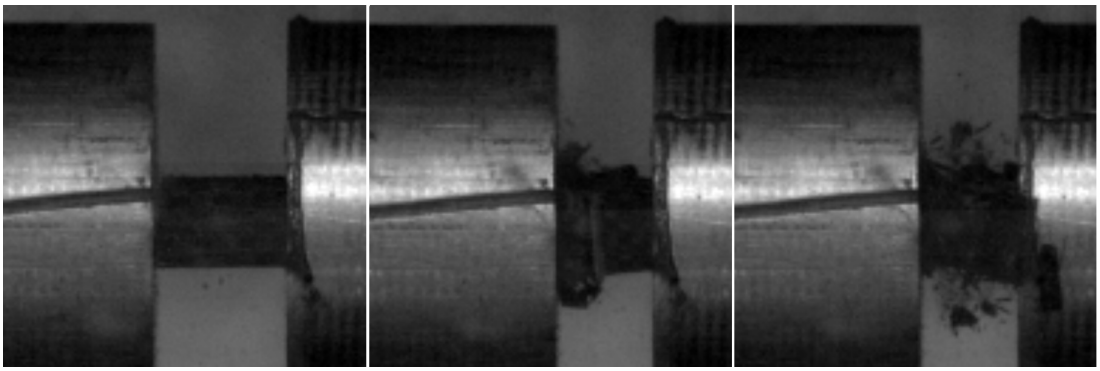


Figure 5.5. CFC SHPB test frames

An example of raw data displayed by the Sure Pulse ™ software is shown in Figure 5.6. In this form the data is simply a measure of output, measured in voltage as a function of time, and is a superposition of the transmitted and reflected pulses in both the incident and transmission bars. The software then handles the conversion process and transforms this signal into the desired forms of stress, strain, and strain rate as functions of time.

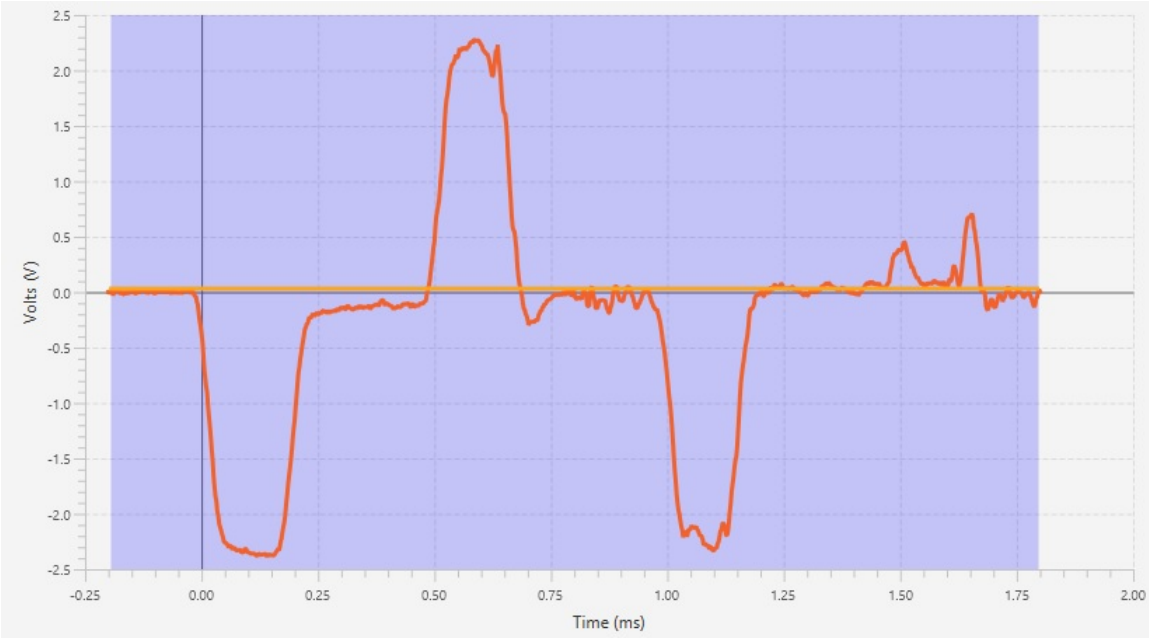


Figure 5.6. SHPB raw data

The two plots of data that are primary interest for this effort were the stress and strain rate as a function of time. The stress vs time curve was used to bound failure from above. This value was then used to estimate the failure strain that occurred at the time that the peak stress was realized. A total of 12 tests were conducted, 7 of which were conducted with the fibers parallel to the axis of the SHPB and 5 with the fibers perpendicular to that axis. Figures 5.7 and 5.8 are examples of the stress experienced by the samples with the fibers aligned parallel to the direction of the pulse transmission and those with the fibers aligned perpendicular to it.

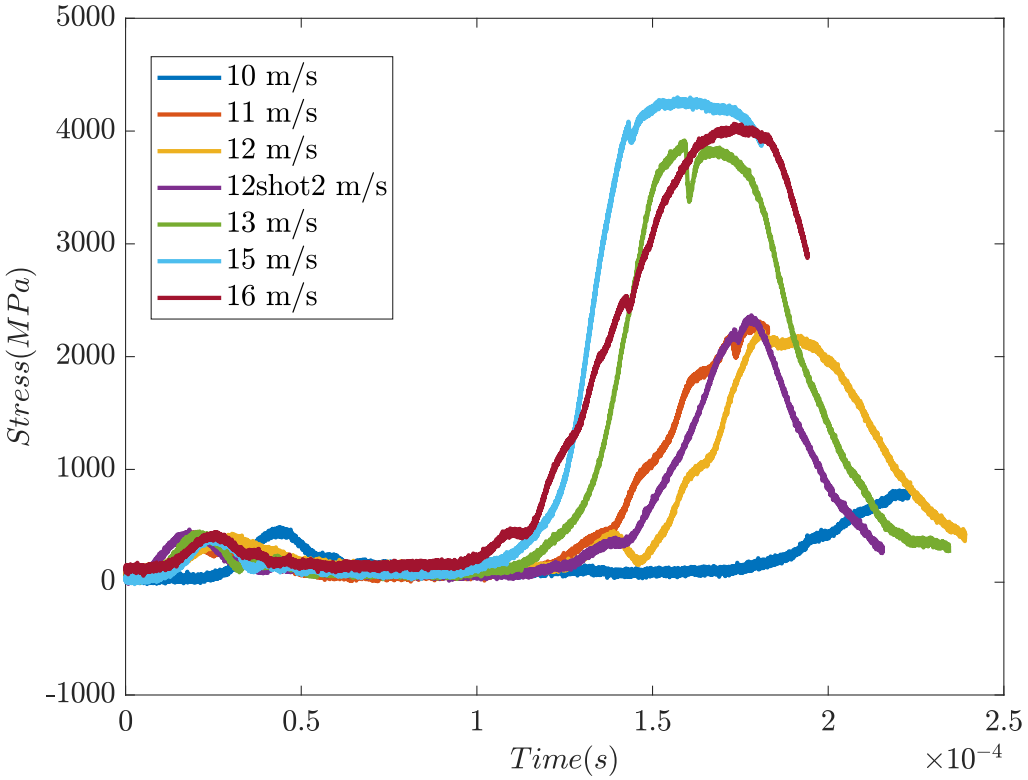


Figure 5.7. SHPB CFC stress vs time for parallel fiber orientation

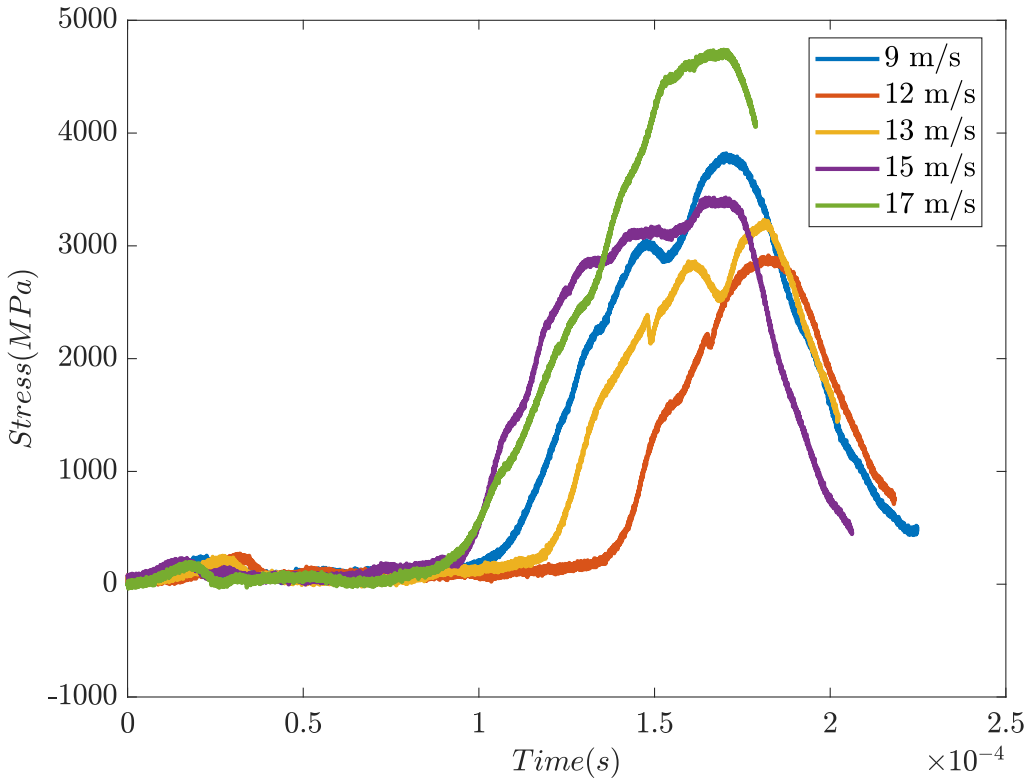


Figure 5.8. SHPB CFC stress vs time for perpendicular fiber orientation

The peak stress values taken from Figures 5.8 and 5.9 are shown in Table 5.2. It is important to point out that in almost every case, these values exceed the maximum, theoretical, composite failure stress of 1.45 GPa.

Table 5.2. Maximum stress for SHPB compression testing

Test	Fiber orientation	Max Stress (MPa)
1	Parallel	813
2	Parallel	2310
3	Parallel	2247
4	Parallel	2366
5	Parallel	3916
6	Parallel	4299
7	Parallel	4064
8	Perpendicular	3820
9	Perpendicular	2914
10	Perpendicular	3229
11	Perpendicular	3428
12	Perpendicular	4739

The data shown in Figures 5.8 and 5.9 was somewhat surprising in that there were no discernible difference between the stresses that resulted from the different fiber orientations. Similarly there were also no noticeable trends in the strain or strain rate as functions of time nor was there any consistent difference between stress as a function of strain. Although somewhat variable, the strain rates for these tests ranged from roughly $4.6 * 10^3 s^{-1}$ to approximately $7.5 * 10^3 s^{-1}$ as shown only for the parallel fiber orientation samples in Figure 5.9.

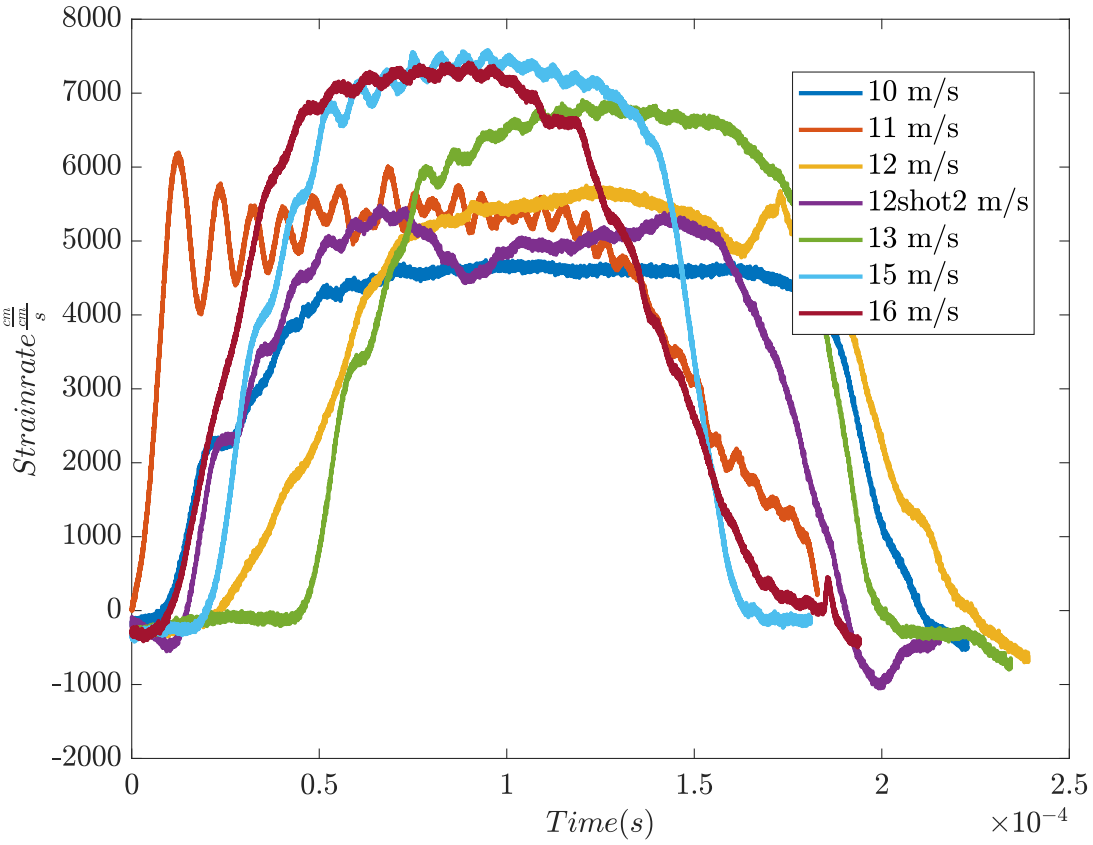


Figure 5.9. SHPB CFC strain rate vs time for parallel fiber orientation

Both the parallel and perpendicular fiber orientation samples exhibited similar behavior wherein they experienced a very rapid rise in strain rate and then essentially plateaued to a value that varied only a few hundred s^{-1}. No variations with strain rate were noticeable in any of the subsequent data. The lack of variation with strain should not be surprising however, because although the question of the strain rate sensitivity of CFCs may be debated, regardless of the degree to which it is present or its effect, the general consensus is that any sensitivity that does exist occurs as a result of the polymer matrix and not the fibers themselves [37], [119], [120]. As the fibers comprise approximately 60% of the overall composite it is reasonable that far less strain rate sensitivity would occur than might otherwise be the case for a higher volume fraction of matrix.

From an examination of HSV, an example of which was shown in Figure 5.5, total catastrophic failure was observed for every sample tested. Although precisely locating the time, location, or stress at failure was impossible given the framing rate and imprecise synchronization of the HSV with the strain gauge, it still clearly shows that the CFC sample is rapidly compressed. In addition, this rapid compression appears to subsequently result in matrix to fiber separation before some of separated material is ejected radially outward. During that time however, even after the matrix had failed but before all of the sample had been forcibly driven out from between the incident and transmission bars, the strain gauge was still recording data. Much of this data was therefore recorded *after* matrix separation and includes values resulting from whatever damaged fiber and/or matrix was compacted between the incident and transmission bars. This compaction occurred after initial failure but while both the strain gauge and HSV were still collecting data.

As a result of continued data acquisition after initial failure and a fact that the values are all significantly greater than the theoretical, *composite*, compressive strength of 1.45 GPa, the peak failure stresses shown in Table 5.2 are likely not indicative of *fiber* failure. Furthermore, those values are also likely an overestimate of the stress at which matrix failure initiated in these samples. If we look to the plot of stress vs time we see that in general, both of the curves shown Figures 5.7 and 5.8 exhibit inflection points well before they reach their peak values. If we zoom into the plots of stress vs time, we see some interesting behavior at an inflection point that lies well below the peak stress values. A plot of this is shown in Figure 5.10.

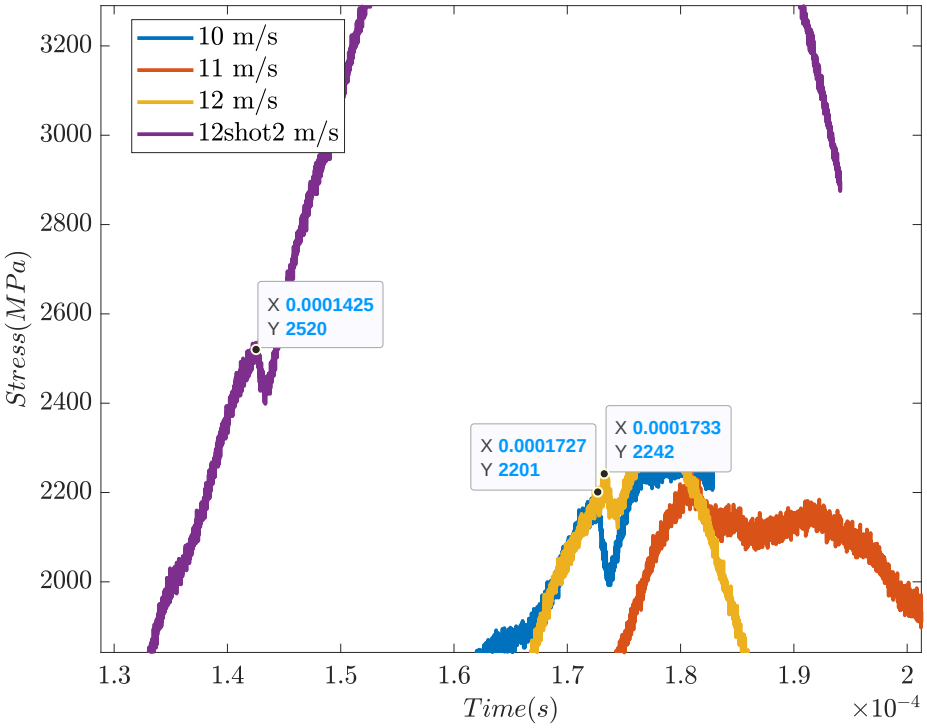


Figure 5.10. Close up of Figure 5.7

This point of interest occurs early in the rapid ramp up to peak stress. Although not equally pronounced in all traces, from Figure 5.10 we can see this occasionally subtle feature if we zoom into the plot to a greater degree. The most salient feature of this plot however, is how little these values change with a corresponding strain rate that varies from approximately $4500 - 5700s^{-1}$. Despite such variation, the mean stress for all the curves was 2.321 GPa with a standard deviation of only 174 MPa. The lack of variation in this value further reinforces the idea that considering the CFC to be independent of strain rate effects is a valid assumption and provides sufficient evidence for applying this assumption to even higher strain rates. It was impossible to visually verify whether this is in fact the point at which matrix to fiber separation occurs but if that hypothesis is correct, it obviates any difficulty in understanding why there were no strain rate effects when only fiber remains and the only contributor to strain rate variability has been completely destroyed.

5.4 Explosive Sample Preparation and Testing

The size and shape of the samples needed for explosive testing necessitated a different approach as a greater level of control over the fiber layup and orientation was desired than was capable of being delivered via commercial off the shelf (COTS) composite samples like the Dragonplate used for the previous SHPB testing. These samples were cylindrical and owing to the thickness and orientation of interest, had to be manufactured specifically for this purpose. Although two different sizes of CFC samples were prepared, both were manufactured using TCR ™ Composites preimpregnated tows comprised of a winding of Toray T700SC-50C fibers with an embedded TCR's UF3325 resin. The larger samples were prepared using an 4 axis X-winder ® filament winder while the smaller samples were prepared using a locally manufactured machine. Both used an orientation of ($\pm 85°, \pm 85° \pm 45° \pm 85°, \pm 85° \pm 45°$) where a 90° winding is strictly circumferential and a 0° winding is strictly longitudinal. After completion of the winding, the fiber wound mandrel was wrapped with a shrinking tape and then placed in an oven for curing. The heated curing process causes the tape to shrink and forces the epoxy, already preimpregnated into the fiber tow of which the structure is comprised, to flow within the confines of the tape and mandrel such that the finished product is, for all intents and purposes, a uniform composite structure identical to that which would have resulted had a dry fiber been pulled through a resin bath and cured using more conventional vacuum bagging technology. The finished sample was then removed from the mandrel, most often by pressing it out.

When using the X-Winder to create CFC tubes in this way, users should be cautious of using low winding angles. Low winding angles require a lot of attention and effort to maintain fiber angles without inducing filament drag that results in either gaps or excessive overlap. Although the ends of the samples were discarded, and the overall sample sectioned to create shorter test articles, should it be necessary to produce a sample near the full mandrel length, such a technique might prove to be unacceptable. The closer to 0° but all angles less than about 30° require additional effort to ensure the filament is laid down in an ideal manner. Initially this was in the form of pins in a sort of spiked "dog collar" but the radial distance that the pins protruded necessitated holding the eyelet of the filament winding arm farther away from the mandrel during rotation. This had the undesirable effect of encouraging filament drag and/or separation making the production of a high quality winding impossible, at least in the vicinity of the ends. Additional attempts were made

with additively manufactured and COTS pin collars but each of these experienced similar problems. In the end, the only method that proved successful to make low fiber filament winding angles was to manufacture, or in this case print, rounded hollow end caps so that the machine could operate in a true 4-axis manner with the feed head moving in and out radially along the mandrel length and the filament could be consistently and accurately wound over the ends near the rotating shaft. This inhibited fiber separation and made the layup to be of high quality with minimal gaps or overlap.

In order to prepare samples that were the orientation of interest for interrogating the failure model at these higher rates, it was necessary to prepare custom parts through the use of a carbon fiber filament winding machine. The X-winder used to produce the larger, high rate samples is a small desktop filament winding apparatus that gives users the ability to produce high quality, low cost cylindrical samples with a shallow learning curve due to an intuitive interface that does not require a user to have an intimate knowledge of G-code in order to produce different layups, although some knowledge is certainly helpful as slight tweaks not made accessible through the graphical user interface were often otherwise impossible. The setup and operation of the X-Winder is seen in Figure 5.5.

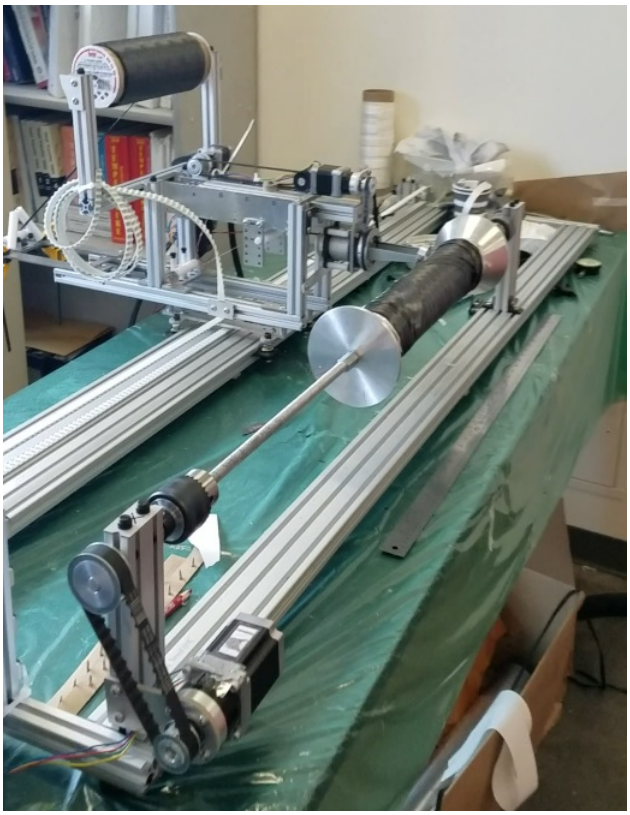


Figure 5.11. X-Winder 4-axis CFC filament winding machine in operation

As mentioned previously, two different filament winding machines were used. NPS' X-Winder was used to produce the larger 7.62 cm diameter samples as seen above and a local machine was used to produce smaller samples an example of which is shown in Figure 5.12.

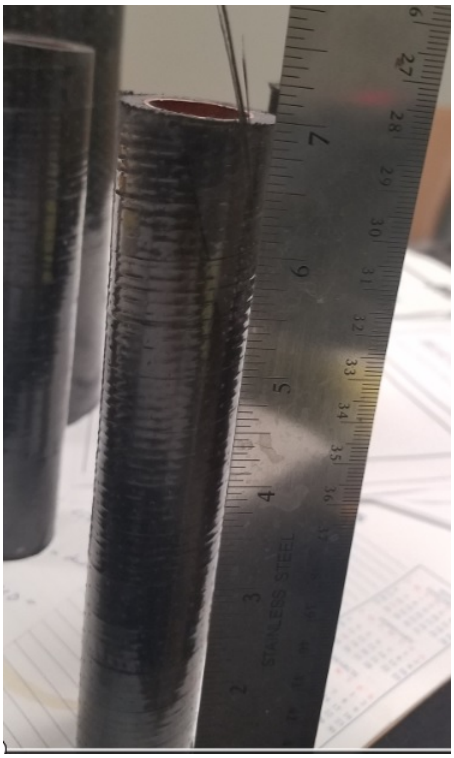


Figure 5.12. Small diameter CFC tube

All samples were parted on a band saw from the larger windings that they were originally a part of. The larger samples were tested with a thick intermediate Aluminum tube as a buffer. This was done in an attempt to gather accurate strain gauge data as it was believed to prolong the event and was hoped to reduce the noise seen by the gauge that was affixed to the outside of the CFC tube. After it was realized that the buffering technique used in the larger diameter tests did not alleviate the high frequency noise on the strain gauge channels, smaller tubes were manufactured locally. These small tubes were the final test articles as the longer overall sample length allowed for greater time for the instrumentation, including both optical and lasers, to gather the data of interest so that a comparison could be made using both of the UFC conditions.

It should be noted that as a result of the manner that the X-winder filament winding machine works in laying up a ($\pm 85^\circ \pm 85^\circ \pm 45^\circ \pm 85^\circ \pm 85^\circ \pm 45^\circ$) orientation, the machine lays

down the +85° layer while traveling down the mandrel axis in one direction and then lays the −85° while traveling in the opposite direction. This type of orientation resembles a twill or fabric where there is a seem of layers running in opposite directions rather than a single +85° layer that forms a complete layer in an of itself with a −85° layer on top of it.

5.4.1 Explosive Testing

All CFC samples were hand loaded with a moldable explosive after which they were permanently mounted into a fixture designed to hold the photonic doppler velocimetry (PDV) probes. An example of an early fixture designed to hold the larger CFC samples with an aluminum buffer can be seen in Figure 5.13. It is important to point out that none of the data presented here was from tests that included the aluminum buffer but mounting fixture shown here was representative of them all.

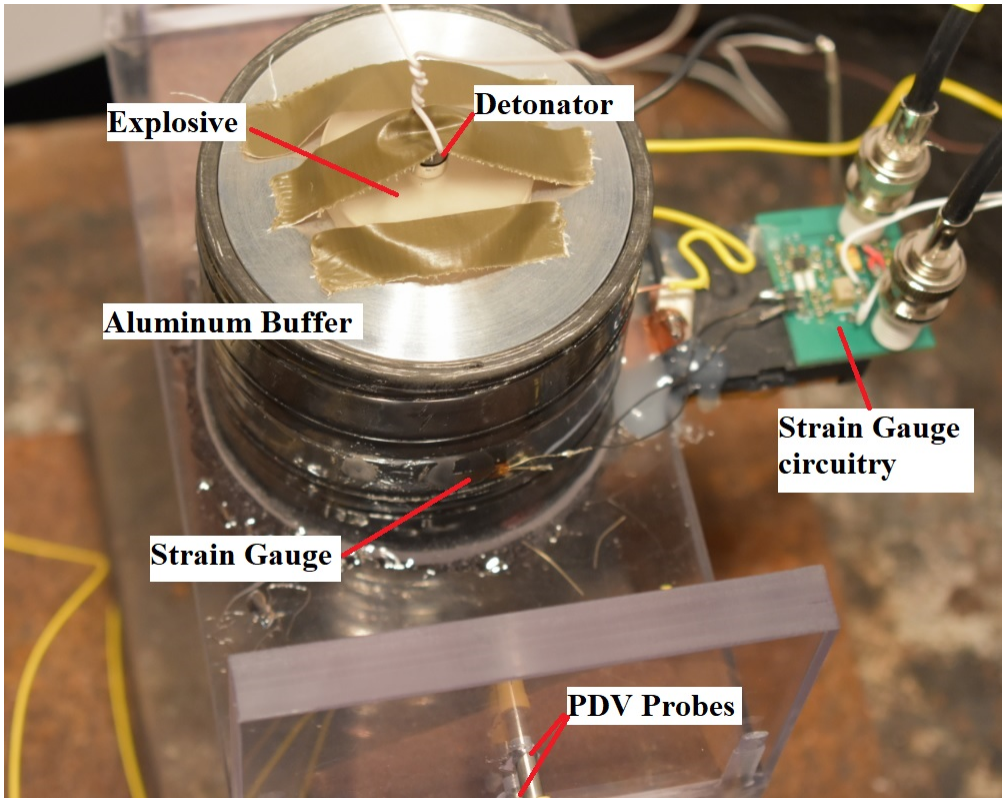


Figure 5.13. Large CFC cylinder experimental setup

All samples were epoxied into the fixture both for stability as well as to ensure orthogonality between the test article and the PDV's emitted laser. Although reflectivity was initially a concern it turned out not to be any issues and the data could be gathered without the need to enhance surface reflectivity.

Initial tests were conducted without using any PDV probes. We attempted to gather strain data using a few different types of strain gauges including traditional Omega SGD-7/350-LY11 gauges in addition to Dynasen Mn/Cn4-50-Ek gauges. All gauges were bonded to the outer surface of the CFC samples using an M-bond AE-10 strain gauge adhesive. All of these tests were conducted using the explosive composition C-4 due to its availability and ease of use which it could be loaded into the test articles. It was loaded piecemeal using a wooden dowel to ensure that no air gaps or imperfections existed as if they were of a sufficient degree, they could change the test results. This also had the added benefit of conforming to any surface imperfections again alleviating concerns of asymmetric expansion or irregular velocity that could have resulted from defects created during the manufacturing process. The characteristics of the explosive used for subsequent modeling are shown in Table 5.2. These are commonly referred to as the Jones-Wilkins-Lee (JWL) Equation of State (EOS) parameters after several early contributors to the field of detonation science [121].

Table 5.3. Composition C4 JWL Parameters

$\rho(g/cm^3)$	Det velocity $(cm/\mu s)$	A (Mbar)	B (Mbar)	R1	R2	ω
1.601	.8193	6.833	0.1487	4.7	1.5	.28

The detonators used for all tests were RISI RP-502 economy exploding bridge wire (EBW). These detonators, essentially the equivalent of a #8 blasting cap with respect to explosive output, are commonly used in testing due to their inherent safety requiring a minimum of 500V to initiate. Although not as precise as other members of the EBW family, they have a much lower price that still provides an initiation standard deviation of less than 500 ns making them more than sufficient for timing of the magnitude that was expected here.

Although the various strain gauges should not have had any limitations with respect to

acquiring data at the rates generated by explosive loading, they were susceptible to high frequency transient noise even when shielded to the fullest extent possible. Shortening the leads and dropping the voltage to a minimal level to fire still did not alleviate the problems with noise. Although the detonation wave should have reached the plane of the strain gauge at about $4.7\mu s$ owing to the variability in the detonator, the transit time of the signals involved, the scope reading the signal and possibly other factors a small amount of variation could not be overcome. Figure 5.14 shows the raw strain gauge output, i.e. voltage as a function of time, for two of these tests. The first signals at roughly $.2\mu s$ were noise induced by the firing pulse going to the detonator. The pulse that occurs at a little under $5\mu s$ was believed to be the initial reading of the strain gauge albeit with unexpected oscillatory behavior. An early hypothesis for why this oscillation occurred was due to a rapid reflection of the incident shock from the outer CFC surface. This hypothesis was quickly abandoned however because it was believed to be highly unlikely that the spall strength of the adhesive used to affix the gauge would have been sufficient to hold the gauge onto the cylindrical surface after the initial incident shock. This signal was therefore hypothesized to be some type of noise coupling to the strain gauge output with the actual reading occurring somewhere in the rising voltage almost immediately after that point. Unfortunately although the trend of the signal was as expected, namely increasing to some failure strain, it still suffered from an extremely high signal to noise (S/N) ratio making it very difficult to determine where the readings began and ultimately where failure had occurred.

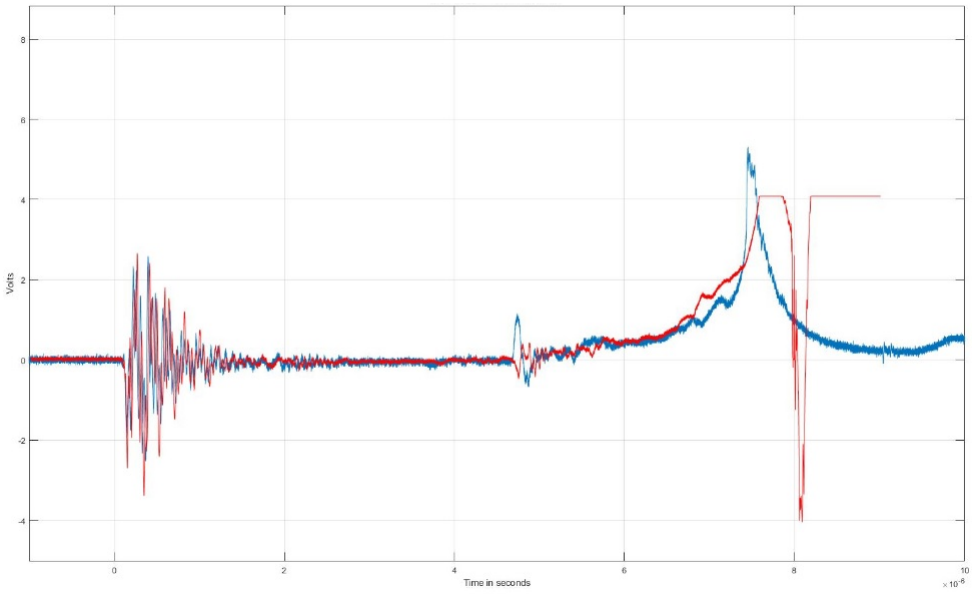


Figure 5.14. Strain gauge voltage vs time (2 large CFC samples)

The high frequency transient noise on the strain gauge channel is believed to have been the result of at least two separate events. The first high frequency decaying signal that can be seen in Figure 5.8 above is believed to be due to the EBW. Because EBWs require such a high initiation voltage, and by virtue of the nature of the location of the detonator to the strain gauge that was mounted to the outside of the CFC cylinder, the magnetic pulse that naturally occurs as a result of the EBW seeing a high voltage pulse was believed to couple to the strain gauge contributing to the noise seen here. Although magnetic shielding of the strain gauge lines was attempted, in addition to dropping the voltage to the minimal level to consistently initiate the detonator, all attempts to diminish this noise were unsuccessful.

In addition to the electrical and magnetic noise from the high voltage pulse sent to the detonator, the extremely rapid exothermic transformation from condensed phase explosive comprised of C, H, N, and O atoms into intermediate molecules including CO, CO_2, H_2O, N_2, NO_x and other products, generates a conductive soup of rapidly changing chemical species. A rapidly evolving cloud of dissociated ions and conductive chemical species develops on the order of microseconds within a region of increasing pressure, temperature, and dynamic chemical species. that only takes about $22\mu s$ to consume all of the solid explosive used

here. Dattlebaum and others have demonstrated that polymers tend to experience changes in electrical conductivity and polarization as a result of experiencing a strong shock [101]. Depending on the polymer, these changes may occur between 20 and 30 GPa. The P_{CJ}, i.e. detonation pressure, for composition C4 is slightly over 27 GPa which places it solidly within the range of likely experiencing changes of conductivity for at least a portion of the matrix from which the CFC cylinder is comprised.

If a shock of this magnitude occurs then the chemical dissociation of a shocked polymer is likely yet another contributing factor to the high frequency transient noise that made it impossible to consistently collect clean output from the strain gauges. As a result of this inability to extract useful strain gauge data, in addition to the inability to precisely synchronize strain gauge measurement with the beginning of the event, i.e. usually the firing signal to the detonator strain gauges were abandoned in favor of the optical technique known as PDV. This technique provided a direct optical measurement of velocity and as a result, was free from problems associated with excessive RF noise introduced by high voltage and the need to measure extremely rapid and sensitive electrical signals from nearby gauges. Ultimately owing to the difficulty of consistently and accurately determining when the strain gauge began to read actual wall strain, and subsequent difficulties in determining at what point failure actually occurred, we found it necessary to abandon the use of strain gauges in favor of the PDV technique.

PDV is a technique developed by O.T. Strand in 2004 while at Lawrence Livermore National Laboratories [122]–[125]. Although it is a relatively new technique in the form that it is now widely used, it is at least somewhat based on other interferometric techniques that have been in use since the late 1960s. This simpler and more modern method uses laser light split in two distinct streams where one is focused on a reflective surface of interest and the other is used as a reference. When the surface of interest moves, rapidly as in the case of a detonation, the reflected laser light, i.e. the light that has been doppler shifted, along with the unshifted, reference light, is collected by a detector. The combination of these two distinct light waves causes a beat phenomenon wherein after they are added and interfere with each other, they produce a waveform with a distinct pattern or beat frequency that is proportional to the velocity of the measured surface. This technique, also allows for extremely accurate measurement of velocity with much less cost and complexity than previously or similar techniques the associated electronics allows for an extremely rapid

measurement of the shines on a surface. In the process of so doing, there is a shift in the frequency of light that is proportional to the velocity of the surface onto which it is focused. This information is then converted from raw form into a more usable measure of velocity. It has largely replaced older and larger, more complicated interferometric systems including the Velocity Interferometer System for Any Reflector (VISAR) and the Fabry-Perot [75] interferometer.

When we switched from using strain gauges to using PDV probes we simultaneously transitioned to a longer sample with a smaller diameter. This new aspect ratio sample had an inner diameter measuring 2.26 cm and an outer diameter of 3.230 cm as shown in Figure 5.12. These were loaded by hand with composition C4 and placed into a fixture that allowed the mounting of inward facing PDV probes as shown in Figure 5.15. The PDV probe locations were chosen such that two pairs were located colinearly opposite each other measuring velocity on opposite walls of the test article, The face of the gauges was approximately 6.6 cm from the outer surface of the tube at about 7.62 cm down from the detonator. The second pair of PDV probes was located another 6.08 cm down from the first pair. This was done in an effort to ensure that the detonation would be fully evolved and had achieved a steady state although this was not the case for the larger samples shown previously.



Figure 5.15. Small diameter CFC experimental set up and PDV probes

The CFC tube was loaded with C4 and glued into the fixture after which the top plate was bolted down and the PDV probes permanently attached to the sides. Because we did not have a consistent and predictable angle at which the tube would diverge from vertical (it was initiated from the top), it was impossible to guess at a more accurate angle to align the probes in a perpendicular sense so they were mounted perfectly perpendicular to the CFC cylinder wall by boring blind holes into the supporting PMMA sides. This is important to remember when we analyze the data for this test in the following section.

As we wished to gather optical data of the progression of detonation in addition to wall velocity from the PDV probes, A white backdrop of cardboard was used for the purpose of reflecting light. A Kirana 5M camera was used with a framing rate of 5 million frames per second and at that rate, additional light was necessary. The additional light was generated using 3 pairs of xenon flash bulbs (not shown in Figure 5.15) triggered in series from the

detonator, with different delays, to illuminate the event over the duration which the camera was capable of capturing frames. Several of the images were spliced together and can be seen in Figure 5.16.

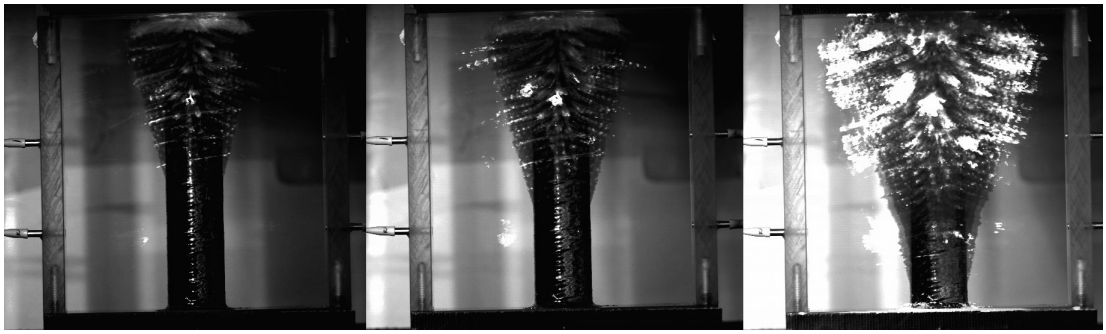


Figure 5.16. Three high speed video frames of explosively driven CFC

These images were captured at approximately 15, 17, and 21 μs respectively. Although the camera was triggered by the signal running to the detonator, it was difficult to synchronize the exact times with the event owing to the facts that the line lengths were somewhat different and so determination of exact camera timing was vague and the fact that so many of the early frames were black. The latter fact was a result from the only approximate and vague times that the 6 xenon flash bulbs began producing usable light. These lights, set up in 3 banks of 2 were staggered to come on at different times during the event. Because of that, in addition to the variable duration over which they produced visible light, the exhibited a breathing like behavior where the light alternated between becoming brighter and darker before eventually being consumed completely although most of the event, with the exception of very early times, was captured. The later images suffer from overexposure as a result of the breakout of gaseous detonation products from the wall which has reached several volume expansions and appears to have already failed in numerous locations. If we enlarge one of the earlier frames however, we can see some interesting behavior. Figure 5.17 is a larger version of the leftmost image above.

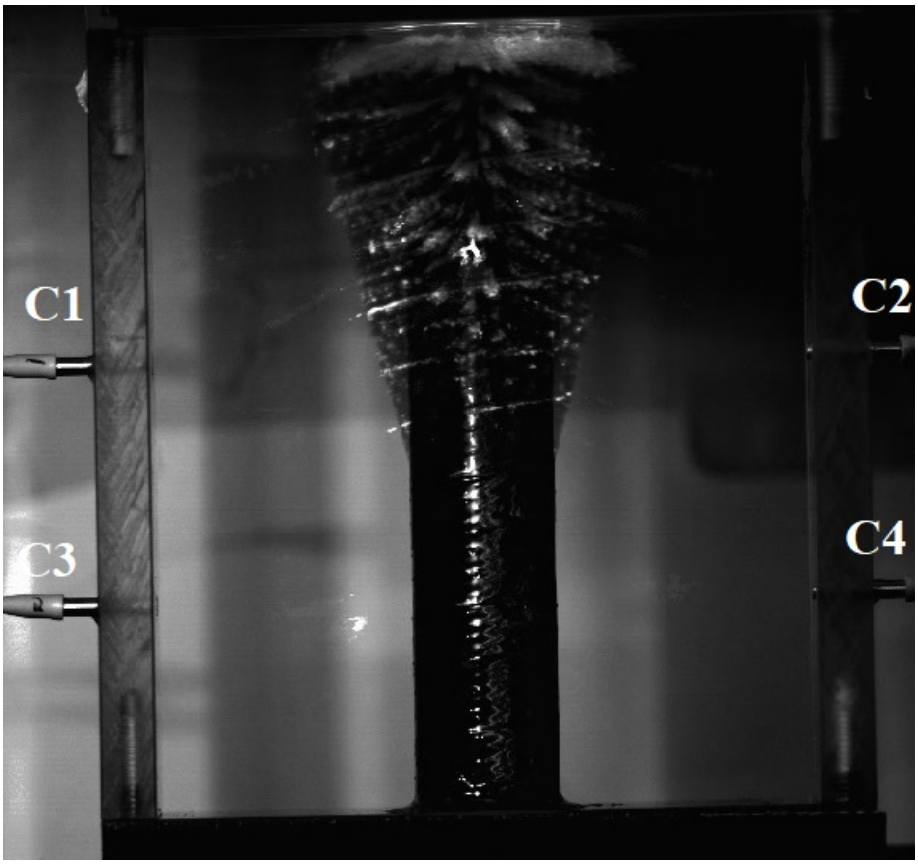


Figure 5.17. CFC cylinder approximately 15μs after initiation

Several important things can be seen within this frame. The first is that the gaseous products appear to have forced their way through the various layers in several locations. Evidence of this is the consistently lit rings that are shown in the expanding region of the CFC tube. What is noteworthy about that fact is that they appear to be the angles closest to circumferential in the ($\pm 85° \pm 85° \pm 45° \pm 85° \pm 85° \pm 45°$) layup. In order to see light through any of the 85° layers, it means that the preceding layers had to have already failed at least to some degree. In addition, from closer examination of the photograph it appears as if at least the outer layer of polymer in the matrix has spalled as a result of exposure to a high shock pressure. The phenomenon of spall occurs when an incident shock reflects from a free surface as a tensile wave and interacts with its own rarefaction. When that occurs, the material is placed in tension and if the magnitude of that tension is larger than the tensile strength of the

material, it fails. In this scenario the spall is radially distributed and results in a field of ejected polymer. In the case of an ordinary metal such as the copper used in a conventional cylindrical expansion experiment (CYLEX), this material remains solid until failure occurs but the polymer is unable to bear that load similarly. This means that in the case of this explosively loaded CFC tube, rather than an in tact, monolithic, radially expanding wall, what is seen and measured is a radially expanding debris field comprised of spalled polymer from the matrix, preceding an expanding layer of fibers from which it has separated at least to some degree.

Evidence of this being a field of spalled matrix is supported by the fact that in the optical photograph of Figure 5.17 you can see through lines of light shining through at a consistent $-85°$ angle from the positive downward direction. This light is only visible in the region of the CFC tube that has expanded radially outward to even a slight degree. Because the layer corresponding to what appears to be a clear and consistent angle is less than the outermost $\pm 45°$ layers however, it can only mean that the outermost layer has separated enough for that light to shine through. Although not conclusively an indication of anything other than ordinary failure in and of itself examination of the raw PDV data provides another clue as to the nature of this failure. PDV gauges are only able to read a sufficiently reflective surface so if at any time such a surface did not exist or was becoming less reflective in time, this would be an additional indication that gaseous products had leaked from the expanding cylinder indicating that failure had already occurred. A consequence of this is that some time after spall occurs, any PDV probe data will rapidly become untrustworthy as it will be too broken and intermingled with high velocity, high pressure and temperature gases that have pushed their way through the various layers to be measuring the wall or even its remnants. This is in fact what was seen in the reduced PDV data as shown in Figure 5.18.

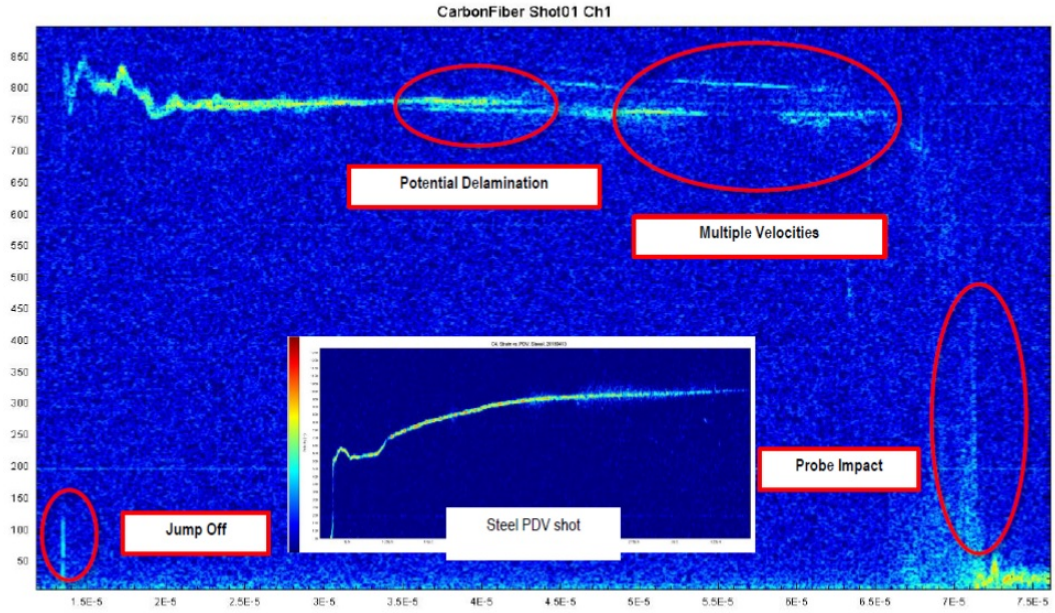


Figure 5.18. Raw PDV trace of a CFC cylinder with steel trace inset

When the larger raw PDV data is compared with the inset which is raw data for a similar test conducted on a conventional metal, the CFC data has a few distinct differences. The most important difference is that the inset contains a long duration signal that is clear and consistent. This type of signal is indicative of a reflective surface that although moving rapidly, is intact when it is measured. The larger image, however, shows only a brief period of a consistent and clear signal followed by what is a non uniquely valued trace. This begins at around $35\mu s$ and becomes much more pronounced at approximately $45\mu s$. Behavior like this only occurs when the surface reflectivity has changed so much that a single strong signal no longer results, as would be the case when the leading edge of the material the PDV laser is reflecting from has shattered into a number of facets, is intermingled with gaseous products, and/or is no longer a single reflective surface. All three of these factors are indicative of what would occur if the matrix had in fact spalled or otherwise been broken into so many pieces that it no longer reflected the laser light as a single monolithic surface. An important aspect of this behavior is that after the point at which spall or fracture becomes apparent, the velocity data and everything derived from it can no longer be deemed accurate enough for use.

5.4.2 Explosive Modeling

Modeling an exploding cylinder using Abaqus requires different techniques than the previous quasi-static modeling. The rapid nature of detonation, occurring on the order of $.8193\frac{cm}{\mu s}$ for Composition C-4 at a density of $1.602\frac{gm}{cm^3}$ as was the case here, meant that the problem needed to be treated explicitly which is of course, only conditionally stable owing to the fact that explicit integration methods must take a time step lower than the Courant-Friedrichs-Lewy (CFL) condition. This requirement for stability states that the distance any information travels in a given time step, must be less than the distance between the elements of the mesh. Ultimately this means that there are far more stringent requirements placed on the mesh density than those for the previously discussed implicit problems and that for similar high rate problems, *conditional stability* is equally as important as *convergence*.

As the region of interest in this problem is the CFC sleeve, there was no need to treat the explosive contained within or the air or void on the outside with equal fidelity. Furthermore, the rapid expansion of the explosive products means that at best, such a region could be treated in an Arbitrary Lagrangian Eulerian (ALE) manner as is done in many "*hydrocodes*" created solely for the purpose of solving such problems. Here however, the explosive was treated as a an Eulerian material without any loss of accuracy occurring in the region of interest. To solve problems where one or more of the materials is expanding in a manner that would otherwise cause numerical problems at the very least would include a loss of accuracy if all regions were considered similarly, the later versions of Abaqus have a capability called CEL for Coupled Eulerian Lagrangian analysis. This was the type of analysis used here wherein the CFC tube of interest was modelled as a Lagrangian solid with an Eulerian HE and air regions surrounding it. Abaqus handles the transfer of information between the two meshes and allows for a simpler calculation that that which would be necessary should an ALE formulation been used.

This problem was comprised of an Eulerian domain consisting of approximately 141k EC3D8R Eulerian elements and a Lagrangian CFC sleeve composed of about 3408 SC8R linear shell elements from the standard element library. Although a traditional linear Us-up model could have been chosen it would have homogenized out the physical behavior of interest and so although there was no consideration of rate dependence, the engineering constants were used to define orthotropic elasticity of the composite. Shell elements were

used because of the relative thickness of the structure in the radial direction. These were of the reduced integration variety owing to the expectation of large deformations and concerns over potential hourglass modes. The high explosive (HE) was shaped in and defined using the Composition C4 JWL explosive parameters given in Table 5.1 of Section 5.4.1. The only boundary conditions were applied to the exterior of the Eulerian region wherein no inflow was allowed but free outflow was permissible. At time 0 the HE, which had been shaped in using the volume fraction option of the discrete field tool, was detonated and the detonation propagated downward from top to bottom just like in the previously described experiment. It is important to point out that modeling composites using the composite layup technique in an explicit calculation is not enabled like it was for the previous implicit calculations and as a result, the lamina properties, to include thickness and fiber orientation, had to be defined using a composite section which was then assigned to the sleeve surrounding the explosive. A single element was defined in the radial direction and the layer thicknesses were assigned under the section definition. Two nodes corresponding to the precise locations at which the PDV probes were located during testing were added to the model and were where the majority of the history output data was collected and output was collected at a rate of one point every .1 μs.

As a result of lacking a computational material failure model, Abaqus does not capture the generation of spall. Spall was observed optically but without a failure model, Abaqus predicted physically unrealistic behavior where the cylinder grew to a point beyond which it had failed as observed during the experiment. Interestingly, without the capability of predicting physically realistic failure, there was virtually no axial translation of the nodes chosen for both the PDV locations and their velocity was almost exclusively radial. This means that when run in this manner, the code has no capability of predicting the Taylor angle and is much closer to the traditional idealization of Gurney velocity [126]. The computational model was limited to 60 μs as that duration was more than sufficient to simulate the actual experiment and to predict failure with which to compare the UFC

An early comparison of the model with an experimental image reveals reasonable physical agreement with experimental data as shown in Figure 5.19.

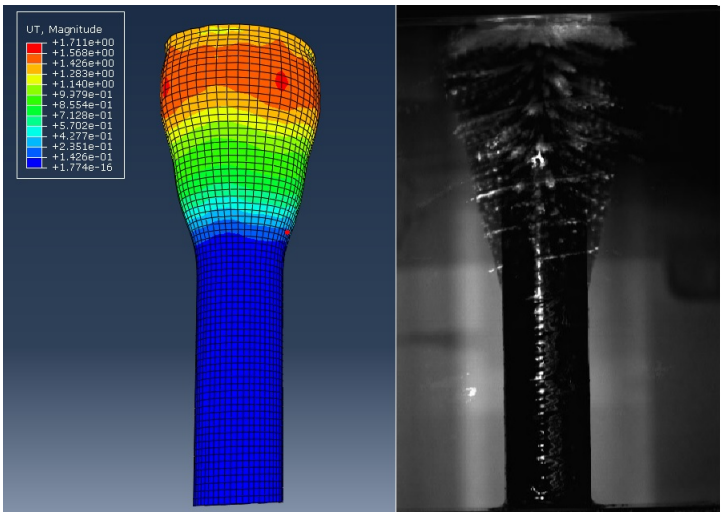


Figure 5.19. Abaqus and experimental CFC wall at approximately 15 μs

There are a few distinct difference between these two images, some which are not the result of experimental variation. The largest difference resulted from an inability to synchronize the camera images to the recorded time due to variation in the Xenon flash bulb illumination time and duration. These bulbs were used for ad hoc illumination and are not precision items so although they were effective, their performance was less than ideal. In addition, the RP-502 EBW used to initiate the detonation also has a half microsecond of function time deviation, that contributes slightly to some of the observed differences. In general however, the surface of the model is a clear and distinct leading edge without any evidence of gaseous products leaking through an locally and irregularly damaged surface.

The wall velocity data is easily gathered from Abaqus and is useful measure with which to compare to the actual PDV data shown in Figure 5.20.

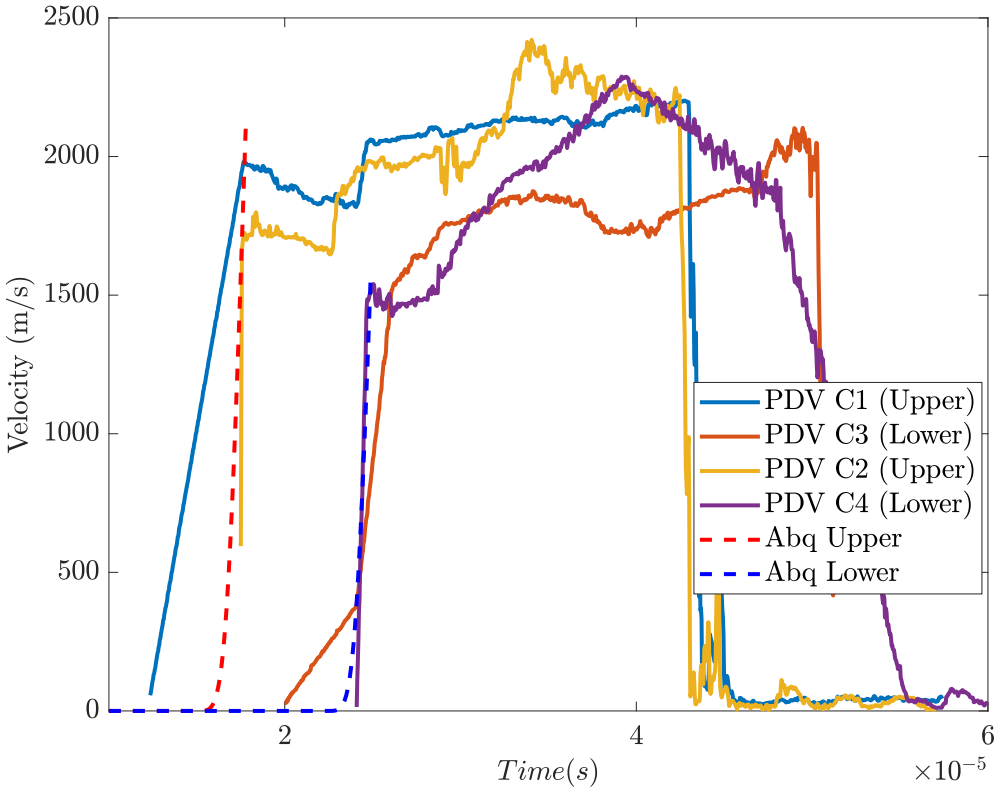


Figure 5.20. PDV and Abaqus generated velocities

The increase in wall velocity predicted by Abaqus closely matches that of the experimental data but it is important to point out that because no failure model was included in the modeling, the CFC tube wall remained intact over the entire duration of the simulation. As a result, were the data from the Abaqus generated PDV nodes plotted even later in time, they would be shown to exhibit a non physically realistic oscillatory behavior. This physically unrealistic pulsation is important as it had an appreciable effect on predicting the position of the outer wall but does not occur in reality due to the destruction of the CFC during the explosive detonation. Actual failure occurs relatively early as the solid explosive is converted to high pressure gas which destructively expands the CFC cylinder. For metals like steel, anecdotal evidence suggests that this occurs around 3 volume expansions so failure occurring sooner for a more brittle sample would be expected. Precisely where the

failure occurs in time however, remains to be seen from Figure 5.20.

A noteworthy feature in the PDV data is an immediate jump followed by a subsequent decrease in velocity that drops to a local minimum before again increasing rapidly. This location, pronounced in all of the signals but channel 3, occurs between .5 and 6.4 μs after the initial peak is reached as shown in Figure 5.21.

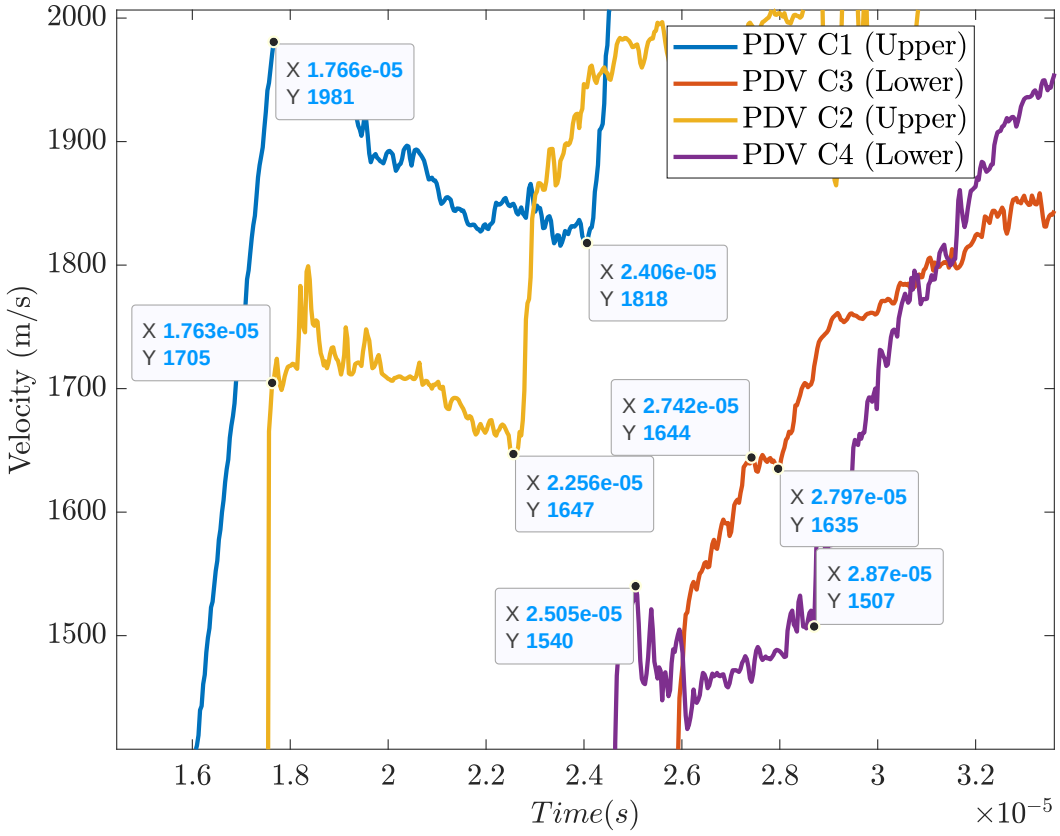


Figure 5.21. Closeup of hypothesized failure times from Figure 5.20

For the upper PDV locations, this occurs between 22.6 and 24.1μs and for the lower PDVs this occurs from 28.0 and 28.7μs. Our hypothesized explanation for this deceleration is the previously discussed topic of spall. Based on the thickness of the tube wall and the sound speed through the matrix but perpendicular to the fibers, it should only take somewhere on

the order of 1-2 μs for the shock to begin reflecting from the outer surface. This brief time relative to the deceleration reached approximately 4-6 μs later means that there is enough time for spall to manifest itself before reaching 22.5 and 24.1 μs as shown in Figure 5.21 so although further verification was not possible using the given diagnostics, the duration such an effect could have had falls well within the time over which deceleration occurred. If the matrix has completely spalled by this time however, then the only material left to resist the expanding pressure is the remaining fiber and whatever matrix was trapped and not ejected during the time the detonation wave swept down the inner surface of the cylinder.

If we adjust the start time of the data gathered in Abaqus to that of the PDV gauges, and we plot the average of the time that the hypothesized failure point occurs above, namely 23.5 μs and 28.4 μs, on the plots of position and strain versus time, we see the results shown in Figures 5.22.

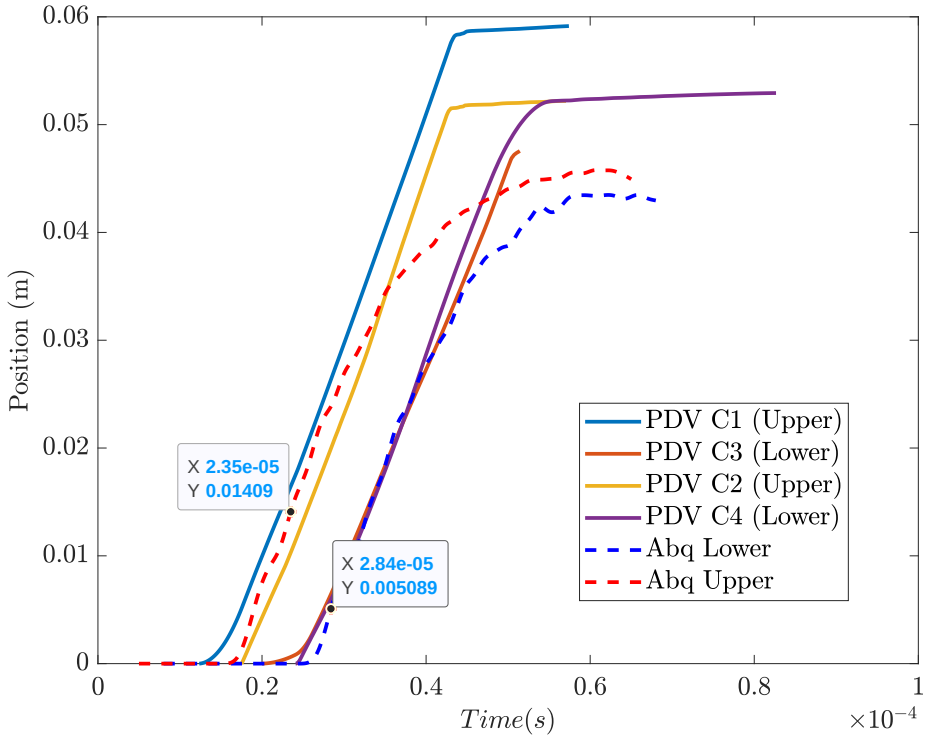


Figure 5.22. PDV and Abaqus generated velocities

These are the points in time at which failure was hypothesized to occur based on the experimental data overlaid on the positions predicted by Abaqus. The slope of the experimental and computational data closely match although there are differences at the outermost positions. This is partly because the validity of the upper limit of experimental data is a subjective measure, influenced by the dispersion in measured velocity, an example of which is shown in Figure 5.18. Had the raw PDV data been truncated sooner, this would have reduced the measured position but not the slope or the temporal difference between the gauges. Similarly, had a failure model been used, the CFC body would have continued expanding radially outward so the combination of these two events would likely have given closer agreement at later times.

Figure 5.23 shows similarly good agreement between computational and experimental results. This is unsurprising since strain is simply a logarithmic transformation of position.

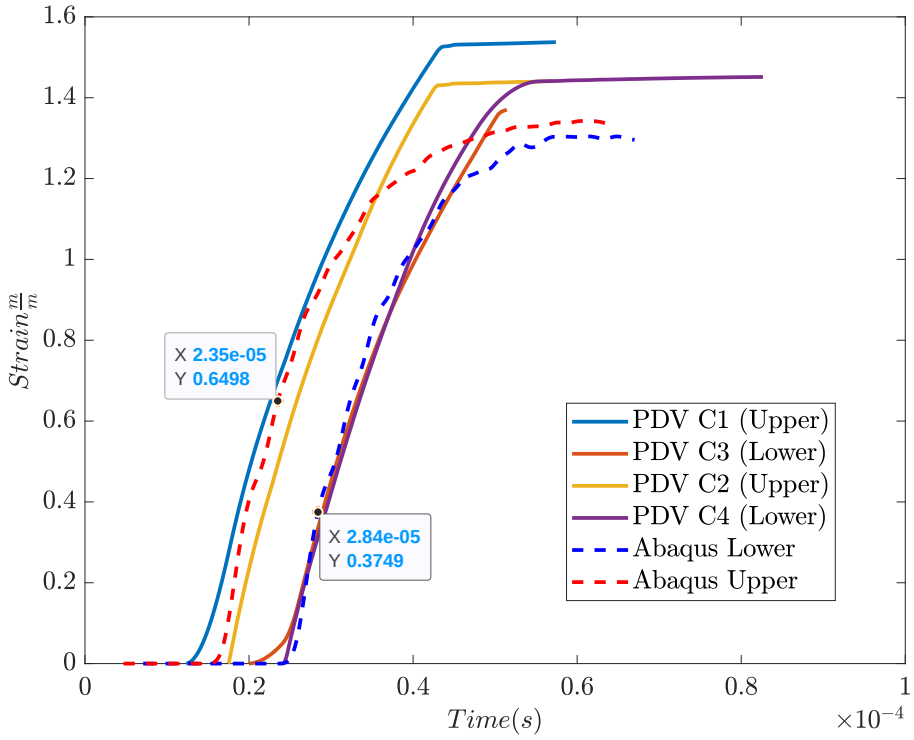


Figure 5.23. PDV and Abaqus strain comparison

Because the qualitative and quantitative agreement between experimental and computational models was determined to be sufficiently close, we calculated failure via the UFC. Unlike during the previous quasi-static testing however this testing occurred at a strain rate varying from $8 * 10^4 s^{-1}$ to $1 * 10^5 s^{-1}$ depending on which PDV probe was used. Because the position as a function of time was modeled and calculated, those values could be used to calculate logarithmic strain and compared with those values predicted computationally to quantify the degree of agreement with the UFC.

A key point is that as Abaqus was used here, it calculates stresses at the *composite* level but the previously proffered hypothesis was that the matrix had spalled and largely separated from the fibers earlier in time. This is supported by both optical and PDV data. Although the stresses calculated by Abaqus were computed at the composite level, because we hypothesized that the actual composite had lost all of the matrix, the only remaining parts that could absorb the stress of the rapid expansion, if that hypothesis is correct, were the fibers. This assumption was key to allowing us to begin to calculate the stresses at the fiber level rather than that of the composite. Before doing so however, the stresses would need to be transformed to the proper direction to that of the fibers.

In order to ensure that the fiber orientation matched the sample which was tested, it was necessary to define a local cylindrical coordinate system with which to reference the fiber orientation and stacking direction of the SC8R elements. Although more complicated than that for implicit analyses, this produced values for stress and strain that could be easily checked by changing the fiber orientation and then visualizing the results and looking at the S11 and S22 components of the stress tensor. Since the fibers bear the majority of any tensile load, whichever stress was greatest in the fiber would manifest itself in a greater stress which could then be used to give the user an idea of whether their directions were aligned with their chosen coordinate system in the manner in which they thought. To some extent, this could be verified via the material ply stack plotting option in Abaqus as seen in Figure 5.24.

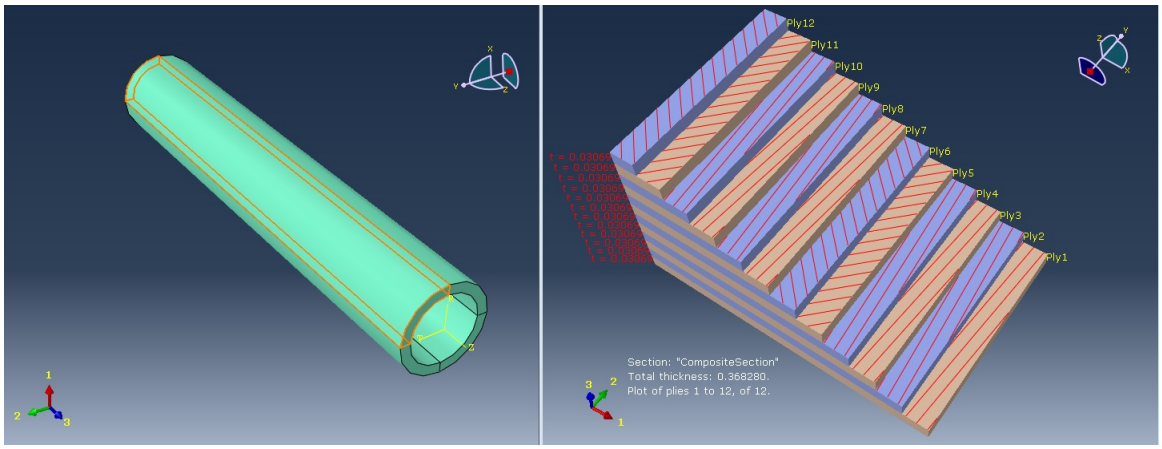


Figure 5.24. CFC cylinder and ply stack plot

Although Abaqus is capable of generating numerous tensor values of interest, in particular the relevant components of stress (S11, S12, and S22) and logarithmic strain (LE11, LE12, and LE22), when shell elements are used, Abaqus outputs tensor quantities with respect to element surface directions. These directions were used to define the fiber orientations but they were not identical to the fiber alignment. As a result, the stresses and strains needed to be transformed to an orientation corresponding to the directions of the fibers. Only the exterior lamina were displayed here although Matlab was used to interrogate the inner lamina. A Matlab script was also used to implement the transformation equations of interest. The transformation equations used to change the various σ_{11}, σ_{12} and $\sigma)22$ values into a coordinate system of interest, i.e. in the fiber directions for the outer $-45°$ lamina are given by Equations 5.3 and 6.1.

$$\begin{aligned} \sigma_{x'} &= \sigma_x cos^2(\theta) + \sigma_y sin^2(\theta) + 2\tau_{xy} sin(\theta) cos(\theta) \\ \sigma_{y'} &= \sigma_x sin^2(\theta) + \sigma_y cos^2(\theta) - 2\tau_{xy} sin(\theta) cos(\theta) \\ \tau_{x'y'} &= (\sigma_y - \sigma_x) sin(\theta) cos(\theta) + \tau_{xy}(cos^2(\theta) - sin^2(\theta)) \end{aligned} \tag{5.1}$$

and

$$\begin{aligned}\epsilon_{x'} &= \epsilon_x cos^2(\theta) + \epsilon_y sin^2(\theta) + \gamma_{xy} sin(\theta) cos(\theta) \\ \epsilon_{y'} &= \epsilon_x sin^2(\theta) + \epsilon_y cos^2(\theta) - \gamma_{xy} sin(\theta) cos(\theta) \\ \gamma_{x'y'} &= 2(\epsilon_y - \epsilon_x) sin(\theta) cos(\theta) + \gamma_{xy}(cos^2(\theta) - sin^2(\theta))\end{aligned} \tag{5.2}$$

to calculate the transformed stresses and strains respectively. In this case θ was the angle of the fibers and σ_x, σ_y, and τ_{xy} corresponded to S11, S22, and S12 while ϵ_x, ϵ_y, and γ_{xy} corresponded to LE11, LE22, and LE12. Plots of the transformed stresses at the top and bottom PDV locations are shown in Figures 5.25 and 5.26.

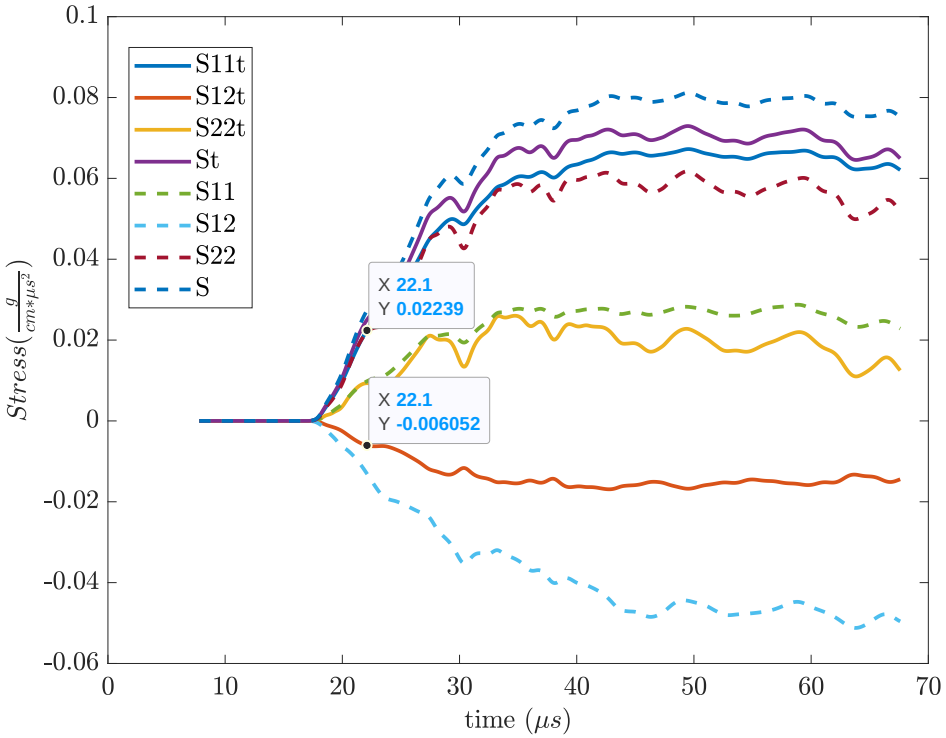


Figure 5.25. Untransformed and transformed stresses for upper PDV location

And at the lower PDV location the transformed and untransformed stresses were similarly plotted in Figure 5.26.

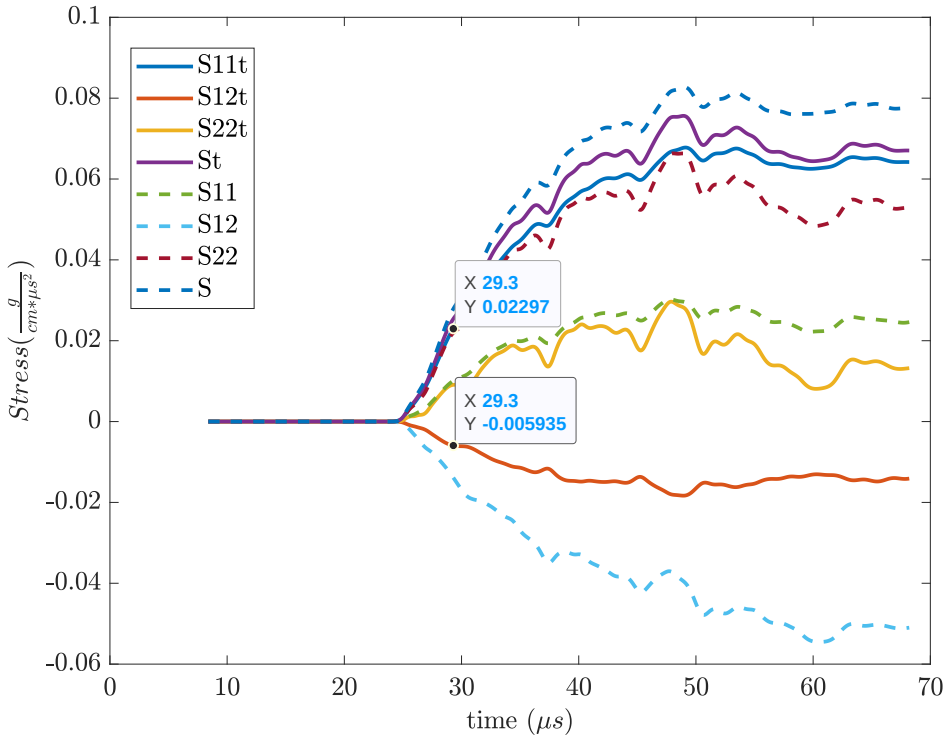


Figure 5.26. Untransformed and transformed stresses for lower PDV location

The values displayed on both plots are critical values calculated based on the times that result from forcing the effective stress, σ^f_{eff} to be equal 4.9 GPa and then marching through time for S11t and S12t values that achieve this value through the use of the down scaling equation. As will be shown, this provided a method to determine failure times that was completely independent of the PDV gauge data.

The down scaling equation from the multi-length scale approach discussed in Section 4.4.2 provided a mechanism to calculate the effective stress at the fiber level using the stresses calculated after they had been transformed to the correct orientation as described previously. Equation 5.3 was used to determine the effective fiber stress.

$$\sigma_{eff}^{f} = \sqrt{(\sigma_{11}^{f})^2 + \frac{E_{11}^{f}}{G_{12}^{f}} * (\sigma_{f,12}^2 + \sigma_{f,13}^2)} \tag{5.3}$$

This equation, previously used by Kwon [48], allowed us to calculate the effective stress at the fiber level. In order to use this equation the values for $\sigma_{f,11}$ and $\sigma_{f,12}$, plotted on Figures 5.25 and 5.26, need to be known. The value of $\sigma_{f,13}$ was zero here so it did not play any role. The theoretical effective stress for the T-700 fibers tested here was 4.9 GPa. That value was used to march through the plots shown in Figures 5.25 and 5.26 to determine at what point the corresponding $\sigma_{f,11}$ and $\sigma_{f,12}$ values resulted in a close approximated for the effective stress. Since the listed fiber and composite strengths are *ideal* they should be considered to be upper bounds on the actual failure values. Searching the transformed stress values, i.e. S11t and S12t for the times that result in a value of σ_{eff} as close to 4.9 GPa as possible for both the upper and lower PDV locations, we generate the values in Table 5.4.

Table 5.4. Fiber failure stresses and times

Location	time (μs)	σ_{11} (GPa)	σ_{12} (GPa)	σ_{eff} (GPa)
Upper PDV	**22.1**	2.239	.6052	4.953
Lower PDV	**29.3**	2.297	.5935	4.903

These times were generated completely independently of the experimental failure times of 23.5 and 28.4 μs shown previously. Such good agreement, within about a microsecond, is a good indication that the previous assumption of failure occurring at the deceleration point shown in Figure 5.21 was correct. But perhaps even more interesting is what we notice when we overlay these theoretical failure times over the predicted position and strain plots shown in Figures 5.22 and 5.23. These plots are shown in Figures 5.27 and 5.28.

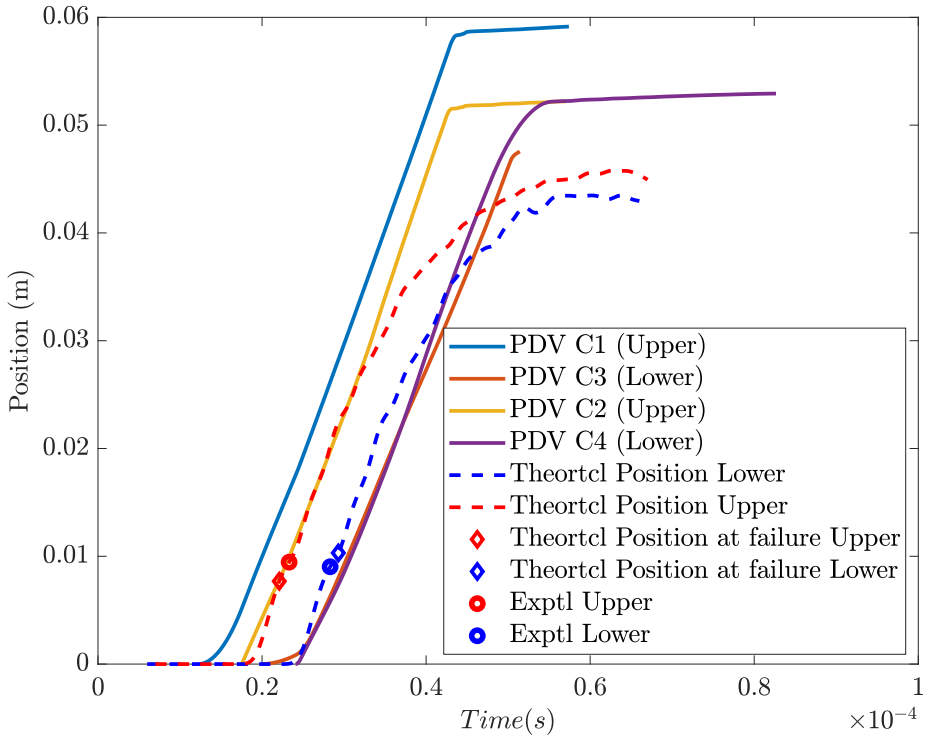


Figure 5.27. Experimental and theoretical failure - position comparison

Here we see both the theoretical and experimental failure times on a single plot and they have close agreement. The estimated difference in position at the upper PDV gauge is a little under 2mm while at the lower PDV it is 1.3mm. Given the potential variation in time and the extreme acceleration and velocity of the CFC wall this is remarkably close agreement. Similarly, when we look at a plot of strain vs time, as shown in Figure 5.28, we see similarly close agreement.

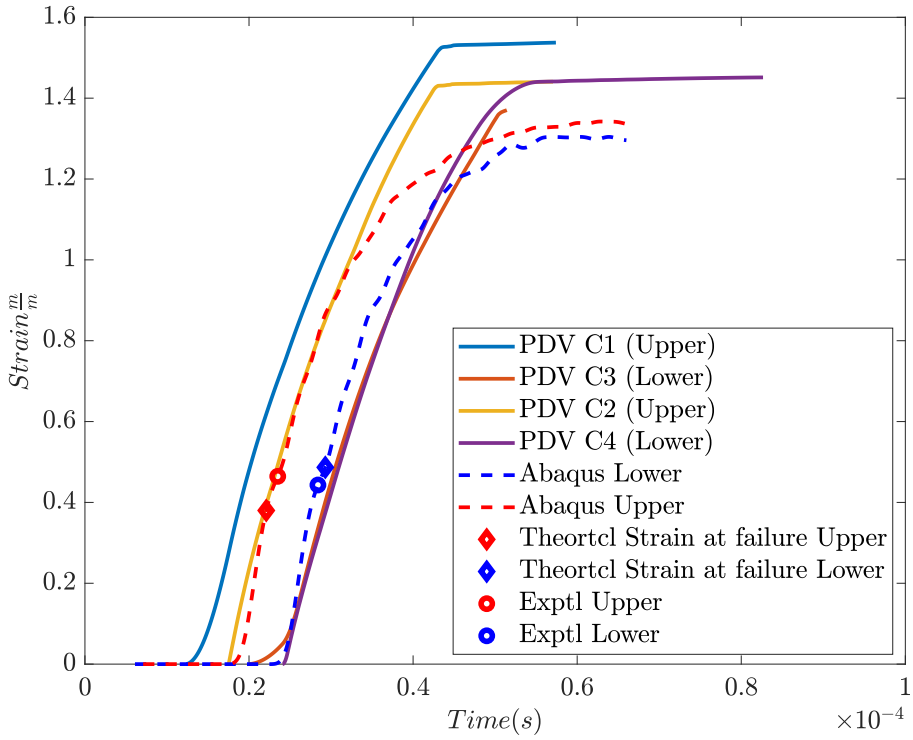


Figure 5.28. Experimental and theoretical failure - strain comparison

In this case there at the upper PDV location we see a difference in strain of about .085 while at the bottom, that difference is a little more than half at about .044. Similar caveats apply but some difference between top and bottom locations might be occurring as a result of the evolution in the detonation wave. At a plane parallel to the upper PDV location, it is possible that because of the small CFC tube size or packing density, that full detonation velocity has not yet been reached. By the time the detonation wave reaches the plane of the bottom set of gauges however, it has likely reached a slightly higher detonating velocity and the curvature due to end effects may also be somewhat changed. Regardless of the exact reason however, the agreement between the theoretical and experimental values here is excellent.

5.5 Conclusions

Two different CFC composites were tested at different strain rates ranging from approximately $800s^{-1}$ to a high of about $1 * 10^5 s^{-1}$. These high strain rates were achieved via dynamic tests using a SHPB and explosive loading. Although these tests tested different loading regimes, namely compressive in the case of the SHPB and tensile in the case of the explosive loading, the UFC predicted incredibly accurate failure stresses at the fiber level in comparison with experimental data.

The unidirectional samples tested on the SHPB were tested with the fibers oriented both parallel and perpendicular to the direction of the wave propagation. No discernible rate effects were observed.

The results generated here rely heavily however, on a key assumption, namely that the matrix quickly and distinctively separates from the fibers as a result of the sweeping detonation and the subsequent shock which propagates through the tube wall. That hypothesis, based on observation of HSV in addition to PDV gauge data needs to be tested to a greater degree to develop a higher level of confidence of its veracity.

CHAPTER 6:
Conclusions and Future Work

6.1 Conclusions

Because of their advantageous properties, composite materials are being used to an ever increasing degree for tasks ranging from the mundane to the strategic. Although their stiffness and high strength to weight ratio make them attractive for a variety of engineering applications, composites in general and CFCs in particular are not without some negative consequences as well. Their brittle nature and our lack of ability to consistently and accurately predict at what point they fail is hampered both by the complexity of their structure as well as the variety of their geometries and loading conditions under which they are employed.

Although the number and type of brittle composite failure models are as varied as composites themselves, there is a clear need for a more unified theory that allows designers to broadly and accurately predict failure for a wide array sample sizes, geometries, and compositions. Having a single model that can accurately predict the failure of a wide range of samples including both those that possess some stress concentrating feature as well as ones that are regular, uniform, and pristine would be invaluable. This is exactly the capability that has been demonstrated here using the newly developed two part UFC. For convenience both parts are restated here.

$$\sigma_{eff} \geq \sigma_{fail} \tag{6.1}$$

and

$$\sigma_{eff} \geq \left(2E \left| \frac{d\sigma_{eff}}{ds} \right| \kappa_{fail} \right)^{\frac{1}{3}} \tag{6.2}$$

In order to predict failure, this analytic model requires the simultaneous satisfaction of both conditions. In doing so it successfully predicts the failure of uniform samples free from

any stress concentrating features such as holes, cracks, or notches but in addition, it also accurately predicts the failure of samples that have a variety of stress concentrations. Several different materials and geometries with stress concentrations were modeled here although all were tested at relatively low strain rates with some a low as $1 * 10^{-4} s^{-1}$. Despite their tremendous differences, the CFC predicted the failure stress for each of these scenarios with almost equal accuracy. These samples ranged from isotropic PMMA to large anisotropic AM PLA dog bones. Both of these materials had stress concentrating holes machined into their centers and the failure of each was predicted with equal accuracy through the use of the new UFC. For the first time, the UFC offered a logical explanation for why tensile test specimens containing small enough holes do not fail in the manner predicted by LEFM alone. The accuracy of the model to designs containing some type of stress concentration did not stop there as it was also applied to scaled samples of a homogeneous HCP subjected to 3-point bending where a crack like feature of defined proportions was created along the test sample central plane. Despite the differences between HCP and the previous polymers, the UFC predicted failure with roughly equivalent accuracy.

In addition to geometric scenarios where the consideration of the stress gradient was critical to accurately predicting failure, the UFC was also successfully applied to predict the failure of brittle specimens without similar features. Although such tests might otherwise be a simple test of a maximum strain or stress criterion, the samples were tested at strain rates orders of magnitude higher than previous ones and failure was predicted at the level of the fibers through the use of the downscaling method of the multi-lengths scale model. Although no holes, cracks, or features caused any gradients of concern during high rate testing, the UFC model accurately predicted failure for strain rates ranging from $4 * 10^{4} s^{-1}$ up to explosively driven extremes reaching a maximum value of $10^{5} s^{-1}$.

Up to this point, a model that accurately predicted failure for such a wide range of geometric features, across such a wide range of material types, across as man orders of magnitude of strain rate had not been demonstrated.

6.2 Future Work

Although preliminary results for the comparison between UFC predicted and experimental failure appear to be extremely promising, this investigation was far from comprehensive.

There were a number of areas that should be interrogated to more definitively determine if a number of the assumptions made here were correct. Better synchronization of the camera with the beginning of the detonation might be accomplished through the use of a make or break switch at the detonator rather than via the fire set used to initiate the camera here. There was too much variability between the time the detonator was operated and the camera began recording so it made precise determination of failure subjected to operator interpretation.

The hypothesis about the matrix spalling away from the fiber might also be supported or refuted by using higher spatial and temporal resolution video better synchronized to the detonation. This might also be further interrogated such that a visible record exists if a conical CFC sample were made and filled with a conical explosive load. If the net explosive weight were reasonably small and the small end of the cone were allowed to drop below the critical diameter of the explosive then it is possible that the CFC sample would not be completely destroyed and some portion of it would remain that might permit visual examination. Although difficult to imagine making a small sample this precise, it might provide a visual record of spall based on where the explosive ceases to detonate. Manufacturing a thicker sample should assist not only with spall but with the ability to see the nature of damage between the fibers and matrix where the explosive ceases to destroy the sample when it is eventually snuffed out.

In addition, there are also a wide range of intermediate strain rates between the bounds of what was tested here that have not been investigated at all. The work of fleshing out these intermediate strain rates, for additional materials both ductile and brittle, to determine the quality of agreement with the UFC model needs to be accomplished. It is possible that the UFC model does not extrapolate in a linear manner between the extremes investigated here. In addition, the second UFC criterion, Equation 2.19 shown above, will likely require modification to incorporate some degree of variation with time if the failure of otherwise pristine samples is to be able to be accurately predicted at high strain rates. In the absence of a gradient the user is left with little beyond needing to overcome the first criterion, 2.18, that might not adequately account for the variation in stress that occurs with many materials as a function of strain rate.

Although the effect of strain rate is believed to be more a function of the matrix than the

fibers, it has not been investigated here and it would be a worthwhile endeavor to attempt to quantify its participation. If it is appreciable enough it might necessitate some alteration of the criterion captured in Equations 2.18 and 2.19.

There is also a need to determine if this model might apply with equal accuracy to the case of multi-axial or combined loading for both brittle as well as ductile materials. Although good agreement was shown here, it was exclusively the case that tensile or compressive failure was interrogated and as a result, no definitive proof has been given that would ensure equal accuracy when applied to more complicated loading scenarios.

Lastly, all of the models applied here were elastic. Even though at least one of the materials plastically deformed far more than it was originally believed, namely PLA printed on the Prusa printers, failure after the initial onset after pronounced plasticity might be of interest. There has been no effort to investigate such behavior to date however so its validity is unknown. It seems likely that owing to numerous differences in these two types of failure that some modification of the UFC might be necessary.

6.2.1 Modeling

The multi-length scale technique successfully applied by Darcy and Kwon to the accurate prediction of numerous experiments including the WWFE among others [24], [25], should be interrogated to determine if extrapolation to higher strain rate scenarios is equally accurate. This will necessitate the porting of previous UMAT models in Abaqus to VUMAT models more appropriate to higher strain rate regimes that must be modeled explicitly.

In addition, no attempt was made to model the SHPB tests, the results of which were used to determine agreement with the UFC here. Although such models have been run before, this will necessitate their recreation within Abaqus and a consideration of the unique aspects of composites including the different sound speeds that result from changing fiber orientation. The use of a purely hydrodynamic model might prove more or less accurate in predicting a qualitative material response although its ability to accurately pinpoint and predict failure is questionable.

6.2.2 Testing

The real world is not often so kind as to isolate the types of loads that composite structures will experience. In order to develop a truly robust capability of predicting failure via the UFC, combined loading representative of that experienced during actual operation should be conducted. Although it was beneficial and even necessary to investigate this theory, all of the testing conducted as part of this effort was either isolated compression or tension testing. Introducing a greater level of loading fidelity will be necessary however, in order to develop more confidence in this model but that will necessitate more complicated testing.

Although SHPB testing was undertaken for at least a preliminary consideration of the accuracy of the UFC to such rates, it warrants a more comprehensive study. For the SHPB testing for example, the fact that the sample needs to be in stress equilibrium means that only condition 1 can be used to predict failure. Doing so begs the question however, of whether or not samples with gradient inducing features can be investigated in order to engage the second part of the UFC. If attempting to induce a gradient violates the fundamental requirement for stress equilibrium for the SHPB test to be valid then an alternative approach will be needed. This might necessitate an alteration of the test or deviation from the way that it is normally run or the assumptions under which it operates in order to be valid however. No such attempts were made here and as a result, this area was left unexamined. In addition, SHPB tensile testing might also be conducted to see if the UFC criteria applies equally well to samples in tension as compression.

The hypothesis that the CFC samples experience matrix to fiber separation that then complicates the remaining data acquisition by being further crushed between the incident and transmission bars should be examined. Although it might not be possible to remove this behavior perhaps the matrix and fibers, in a small enough configuration, could be isolated and tested apart form one another to measure independent failure. This may not be possible owing to the discrete nature of the fiber tows but it might allow the determination of the degree of participation of damaged matrix. Alternatively, perhaps the failure could be interrupted by the use of a stopper of some sort of varying length that when used in conjunction with the CFC specimen, stops the ability of the incident and transmission bars from contacting making it possible to examine interrupted failure that was precluded from reaching a totally destructive level.

A similar but slightly different situation from the discussion of fiber to matrix separation is that of matrix spall upon the composite being subjected to a shock. This behavior was hypothesized to occur during explosive testing but was not verified to as great of a degree of certainty as it should have been. This hypothesis was critical to the accurate prediction of failure and although it appeared to be an accurate one, it should be interrogated much more rigorously. One of the ways that this might be done is through the use of more closely synchronized HSV data. If this data was more accurately synchronized to both the SHPB and the explosively loaded instrumentation, a much more accurate estimation of experimental failure would provide an opportunity to refine the UFC predictions. This is an important task that should be undertaken.

Finally, PMMA samples similar in size and geometry to the large PLA dog bones should be tested for the purposes of generating a more direct comparison between isotropic and anisotropic samples of equivalent size and thickness. The structure of PMMA should provide a good basis for such a comparison and testing of such samples was attempted here but was not discussed due to problems induced by the location and area over which the jaws gripped the samples during testing. Because this occurred to the very end of the sample and the PMMA was relatively brittle, this almost always induced failure from the location that the jaw gripped the sample even when tabs were affixed to both ends. In the event that additional time and resources were available, a set of jaws could be relief cut so that if failure were to occur it would do so farther down the sample although this is no guarantee that it would occur in the central region where desired.

APPENDIX A:
Additional Contributions and Lessons Learned

A.1 CFC Winding Related Issues

A.1.1 Low Angle Winding Problems and Solution

The X-winder carbon fiber filament winding machine was used for the preparation of the larger cylindrical samples discussed in this work. While this is a highly capable machine that minimizes the necessity of having an intimate knowledge of G-code for high quality sample production, it does require at least a minimal level of user expertise in order to produce accurate, quality, CFC samples *over the full translation distance* the carriage head is capable of traversing. When the winding angle is much lower than about 45°, end quality suffered as a result of the delivery head dwelling before beginning a return translation in the opposite direction. When the fiber carriage began on its return journey, this almost always resulted in the fiber either bunching up and overlapping itself, creating gaps, or the fiber would slip which also created gaps. Winding angles above this value did not have any problems but close to 45° when operating the way this XWinder was initially set up almost always resulted in poor end quality.

As a result of experience gained during previous filament winding operations, the intention was to manufacture samples that were overly long and then to section them to produce shorter samples for subsequent explosive testing. The goal of doing so was motivated by the need to minimize the explosive used to load the sections. Since these sections were to be explosively tested, making them shorter would minimize the net explosive weight (NEW) used per shot making it easier and simpler to shield diagnostics from the effects of a near field detonation. The secondary reason for cutting the approximately 2 feet long samples down was because of poor sample end quality.

The primary cause of poor sample end quality was because even though the Xwinder is capable of 4 axes worth of motion, it was generally easiest to operate it in only two, one where the delivery head carriage translates axially and the second where the mandrel on

which the filament is winding rotates. This avoided any complication of having the filament head translate in or out in a radial direction but did nothing to eliminate or even reduce the bunching up or slipping of fibers near the ends. This problem was exacerbated by the fact that the mandrel ends were larger than the mandrel itself. Figure A.1 shows how much larger than the mandrel the ends were.

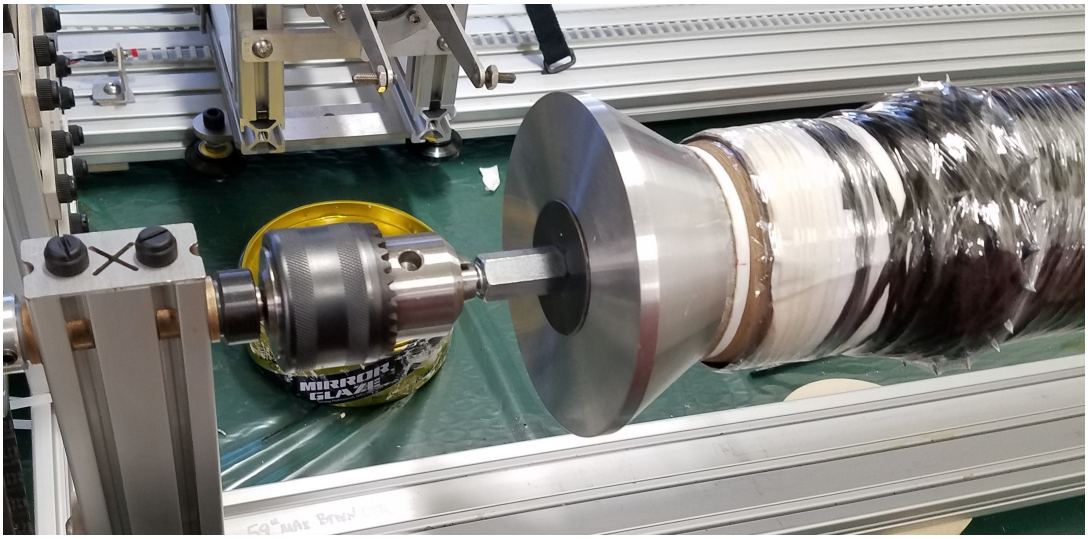


Figure A.1. CFC winding machine mandrel end

Although a configuration like this was fine for preparing samples narrower than the total mandrel length, because it did not eliminate the problem of poor winding end quality it meant that a greater number of samples have to be made since even less of the overall sample length was usable given that samples made in this way still suffered from poor end quality in addition to shorter overall sample length.

Measures were taken to try to overcome this problem, initially with the existing mandrels ends. The first was that the g-code was altered to provide an addition wrap of winding at the ends in the hopes that this would allow the fiber tow to pick up at the proper position before axial translation began without either piling up or leaving gaps. Not only did that not work but it built up the ends in a form of elephant's foot where they were thicker in the radial direction than the sample was in the middle. The quality of the winding was somewhat better but it necessitated radial translation of the winding head in order to not impact the end

tows after the additional wraps caused the sample to become too large here. This eventually caused the tow to go back to overlapping or developing gaps so it was deemed unsuccessful.

The second measure taken to try to reduce poor fiber laydown at the ends of the sample was through the use of a fiber retention or capturing collar comprised of a series of spikes that radiated outward. The hope was that this "dog collar" like fixture, seen in Figure A.2 would provide a site for the fiber to adhere to thus minimizing fiber bunching and slipping.



Figure A.2. CFC Tubes with different fiber capture collars

Unfortunately the irregularity of the collar translated to irregularities in the fiber lay down and it did not correct the problem. There are more commercially available collars that are much more consistent, and we even printed a few collars with much more regular fiber catching protuberances, but none of these worked well.

The solution that ultimately provided the best results was making end caps that were no larger than the mandrels themselves and then operating the machine in true four axis mode.

Although this meant that the operator had to program the radial translation of the filament delivery head, the X-Winder Designer software that came with the machine made it very easy to do so. The primary benefit of this however was that when wound in this way the filament adhered to the ends and after making a revolution before beginning its return axial translation, the fiber always adhered to the end and picked up much more precisely eliminating gaps and bunching in almost all cases. This was the only method in which high quality filament tubes were created without low quality ends.

If this type of winding machine is operated in this manner when the carriage translates to the end and begins translating back in the reverse direction, the fiber tow almost always catches on itself or alternatively, slips as the filament delivery head begins its return journey. This results in either fiber overlap or more commonly fiber slip which generally tends to smooth out and become more regular and consistent but only after the fiber has had time to track back to its original position but even then it does not always even out. This results in samples that consistent and uniform fiber to fiber spacing but only in the middle of the sample whereas the ends experience gaps in the fiber to fiber spacing with a subsequent change in mechanical properties that can not be quantified as a function of wrap quality.

The easiest solution is to manufacture rounded end caps so that the machine can be operated with the fiber tow extending over the ends and around the shaft used to rotate the mandrel. This has been made even easier though the use of modern AM techniques where a rounded end cap of a diameter no greater than the outer diameter of the mandrel can be printed. When used in this manner the previous problems associated with laying down a consistent fiber orientation will no longer plague operators of a winding machine. Because of the wrap that occurs over the end neither fiber slippage nor its bunching up on itself should occur. This will allow the production of high quality samples with low fiber winding angles over the full mandrel length.

A.1.2 Mandrel Separation

Removing a post cured CFC sample from the existing mandrels proved extremely difficult. Most often, the finished samples had to be pressed off of the mandrels. This was an opportunity to damage not only the mandrel but the sample itself and generated at least some risk of obtaining bad results during testing. Visual inspection of opaque CFC makes

inspection and determination of damage impossible so clean and easy removal of any wound specimens is critical to obtaining accurate test results because the strength of a sample can be reduced tremendously as a function of damage. A washout mandrel made from Aquapour, a thick fluid slurry that is water soluble, was attempted but this technique also proved difficult. In particular the material was difficult to mix and cast due to its high viscosity but more importantly, it was not easy to remove intact after curing even after having used a mold release agent. In addition, during casting before the material had cured, it was extremely difficult to remove all of the porosity even when exciting the material on a shaker table under a vacuum bell. Finally after the solidified mandrel was removed from a mold it required heat treatment and sealing to drive off any remaining moisture and seal the surface to eliminate the inner winding porosity which could result if bubbles were present. As a result of the numerous difficulties, no parts were produced using this method. If alternative methods like machined mandrels were unavailable however, with additional effort this technique could likely be used to generate high quality samples although not without difficulty as was discussed here.

To aid in the removal process, a 30 inch aluminum mandrel was machined with a slight taper along the axial direction. It was hoped that this would facilitate removal of the mandrel in a manner that was less likely to damage either it or the sample. The caveat to doing so however, was that any samples manufactured in this way would have a slightly tapered interior finish measuring approximately .001 to .002 inches smaller than the maximum diameter over every 12 inches. In theory this should make mandrel removal far easier if the entire assembly were first cooled down in a refrigerator owing to the differences in the coefficient of thermal expansion between the mandrel and the CFC winding. If smaller sections were cut from the total length of the sample the taper would still exist but would be less pronounced.

THIS PAGE INTENTIONALLY LEFT BLANK

List of References

[1] M. Hinton, A. Kaddour, and P. Soden, "A comparison of the predictive capabilities of current failure theories for composite laminates, judged against experimental evidence," *Comp. Sci. and Tech.*, vol. 62, no. 12, pp. 1725–1797, 2002.

[2] A. Kaddour, M. Hinton, P. Smith, and S. Li, "The background to the third world-wide failure exercise," *J. of Comp. Mat.*, vol. 47, no. 20-21, pp. 2417–2426, 2013.

[3] S. W. Tsai and E. M. Wu, "A general theory of strength for anisotropic materials," *J. of Comp. Mat.*, vol. 5, no. 1, pp. 58–80, Jan. 1971.

[4] Z. Hashin and A. Rotem, "A fatigue failure criterion for fiber reinforced materials," *J. of Comp. Mat.*, vol. 7, no. 4, pp. 448–464, Oct. 1973.

[5] Z. Hashin, "Failure criteria for unidirectional fiber composites," *J. of App. Mech.*, June 1980.

[6] M. Hinton, P. Soden, and A.-S. Kaddour, *Failure criteria in fibre reinforced polymer composites: the world-wide failure exercise*. Elsevier, 2004.

[7] C. Sun, B. Quinn, J. Tao, and D. Oplinger, "Comparative evaluation of failure analysis methods for composite laminates," DOT/FAA/AR-95/109, Purdue University, School of Aeronautics and Astronautics, May 1996.

[8] I. Daniel, "Failure mechanisms in fiber-reinforced composites," *Rev. of Prog. in Quant. Nondest. Eval.*, 1978.

[9] I. M. Daniel, "Failure of composite materials," *Strain*, vol. 43, no. 1, pp. 4–12, 2007.

[10] I. M. Daniel, O. Ishai, I. M. Daniel, and I. Daniel, *Engineering Mechanics of Composite Materials*. Oxford university press New York, 2006, vol. 1994.

[11] P. Soden, M. Hinton, and A. Kaddour, "A comparison of the predictive capabilities of current failure theories for composite laminates," *Comp. Sci. and Tech.*, vol. 58, no. 7, pp. 1225–1254, 1998.

[12] M. Hinton, A. Kaddour, and P. Soden, "Evaluation of failure prediction in composite laminates: background to 'part b'of the exercise," *Comp. Sci. and Tech.*, vol. 62, no. 12-13, pp. 1481–1488, 2002.

[13] M. Hinton, A. Kaddour, and P. Soden, "Predicting failure in fibre composites: Lessons learned from the world-wide failure exercise," *Tech. Papers - Soc. of Man. Eng. - All Series*, 2002.

[14] A. Puck and H. Schürmann, "Failure analysis of frp laminates by means of physically based phenomenological models," in *Failure Criteria in Fibre-Reinforced-Polymer Composites*. Elsevier, 2004, pp. 832–876.

[15] Y. W. Kwon, C. Diaz-Colon, and S. DeFisher, "Failure criteria for brittle notched specimens," *J. of Press. Ves. Tech.*, vol. 144, no. 5, p. 051506, 2022.

[16] M. E. Waddoups, J. R. Eisenmann, and B. E. Kaminski, "Macroscopic fracture mechanics of advanced composite materials," *J. of Comp. Mater*, vol. 5, no. 4, pp. 446–454, 1971.

[17] D. Taylor, *The Theory of Critical Distances: A New Perspective in Fracture Mechanics. 2007*, 1st ed. Elsevier Sci., Oxford.

[18] M. Braun, A. M. Müller, A.-S. Milaković, W. Fricke, and S. Ehlers, "Requirements for stress gradient-based fatigue assessment of notched structures according to theory of critical distance," *Fat. & Frac. of Eng. Mat. & Struc.*, vol. 43, no. 7, pp. 1541–1554, 2020.

[19] J. Whitney and R. Nuismer, "Stress fracture criteria for laminated composites containing stress concentrations," *J. of Comp. Mat.*, vol. 8, no. 3, pp. 253–265, 1974.

[20] S. C. Tan, "Laminated composites containing an elliptical opening. i. approximate stress analyses and fracture models," *J. of Comp. Mat.*, vol. 21, no. 10, pp. 925–948, 1987.

[21] L. Toubal, M. Karama, and B. Lorraine, "Stress concentration in a circular hole in composite plate," *Comp. Struc.*, vol. 68, no. 1, pp. 31–36, 2005.

[22] A. Kumar, A. Agrawal, R. Ghadai, and K. Kalita, "Analysis of stress concentration in orthotropic laminates," *Proc. Tech.*, vol. 23, pp. 156–162, 2016, 3rd International Conference on Innovations in Automation and Mechatronics Engineering 2016, ICIAME 2016 05-06 February, 2016.

[23] Y. Kwon and J. Berner, "Micromechanics model for damage and failure analyses of laminated fibrous composites," *Eng. Frac. Mech.*, vol. 52, no. 2, pp. 231–242, Sept 1995.

[24] Y. Kwon and J. Darcy, "Failure criteria for fibrous composites based on multiscale modeling," *Multisc. and Multidiscp. Model., Exp. and Des.*, vol. 1, no. 1, pp. 3–17, 2018.

[25] J. Darcy, "Failure model for fibrous composites using multiscale modeling," Ph.D. dissertation, Dept. of Mech. and Aero. Engineering, Naval Postgraduate School, Monterey, CA, USA, 2018.

[26] E. Barbero, *Finite Element Analysis of Composite Materials Using Abaqus*, 1st ed. Boca Raton, FL, USA: CRC Press, 2013.

[27] Y. Kwon, *Multiphysics and Multiscale Modeling*, 1st ed. Boca Raton, FL, USA: CRC Press, 2016.

[28] R. Talreja, "A mechanism-based framework for describing failure in composite materials," in *Structural Integrity and Durability of Advanced Composites*, P. Beaumont, C. Soutis, and A. Hodzic, Eds. Woodhead Publishing, 2015, pp. 26–42.

[29] S. Ogin, P. Brondsted, and J. Zangenberg, "Composite materials: constituents, architecture, and generic damage," in *Modeling Damage, Fatigue and Failure of Composite Materials*, R. Talreja and J. Varnat, Eds. Boston, MA, USA: Woodhead Publishing, 2015, pp. 3–23.

[30] R. Talreja, "Physical modelling of failure in composites," *Phil.Trans. of the Roy. Soc. A: Math., Phys. and Eng. Sci.*, vol. 374, no. 2071, p. 20150280, 2016.

[31] Y. Kwon and S. Jung, "Atomic model and coupling with continuum model for static equilibrium problems," *Comp. & Struc.*, vol. 82, no. 23-26, pp. 1993–2000, 2004.

[32] S. Saeb, P. Steinmann, and A. Javili, "Aspects of computational homogenization at finite deformations: a unifying review from reuss' to voigt's bound," *App. Mech. Rev.*, vol. 68, no. 5, 2016.

[33] Z. Hashin, "Analysis of composite materials—a survey," *J. of App. Mech.*, vol. 50, no. 3, pp. 481–505, 09 1983. Available: https://doi.org/10.1115/1.3167081

[34] Y. Rémond, S. Ahzi, M. Baniassadi, and H. Garmestani, *Applied RVE reconstruction and homogenization of heterogeneous materials*. John Wiley & Sons, 2016.

[35] Z. Hashin and S. Shtrikman, "A variational approach to the theory of the elastic behaviour of multiphase materials," *J. of the Mech.and Phys.of Sol.*, vol. 11, no. 2, pp. 127–140, 1963. Available: https://www.sciencedirect.com/science/article/pii/0022509663900607

[36] J. D. Eshelby, "The determination of the elastic field of an ellipsoidal inclusion, and related problems," *Proc. of the Roy. Soc. of Lond. Series A. Math. and Phys. Sci.s*, vol. 241, no. 1226, pp. 376–396, 1957.

[37] L. Ma and A. M. Korsunsky, "The principle of equivalent eigenstrain for inhomogeneous inclusion problems," *Int. J. of Sol. and Struc.*, vol. 51, no. 25-26, pp. 4477–4484, 2014.

[38] T. Mori and K. Tanaka, "Average stress in matrix and average elastic energy of materials with misfitting inclusions," *Act. Met.*, vol. 21, no. 5, pp. 571–574, 1973.

[39] R. Luciano and E. Sacco, "Variational methods for the homogenization of periodic heterogeneous media," *Eu. J. of Mech.-A/Sol.*, vol. 17, no. 4, pp. 599–617, 1998.

[40] A. Caporale, R. Luciano, and R. Penna, "Fourier series expansion in non-orthogonal coordinate system for the homogenization of linear viscoelastic periodic composites," *Comp. Prt. B: Eng.*, vol. 54, pp. 241–245, 2013.

[41] G. Gopinath and R. Batra, "Prediction of elastic moduli and ultimate strength of fiber/yarn-reinforced elastic–plastic matrix using fourier series approach and cuboidal/wedge sub-volumes," *Int. J. of Non-Lin. Mech.*, vol. 125, p. 103539, 2020.

[42] S. Nemat-Nasser and M. Taya, "Effective moduli of an elastic body containing periodically distributed voids," *Quart. of App. Math.*, vol. 39, pp. 43–59, 1981.

[43] W. M. Harris and W. K. Chiu, "Determining the representative volume element size for three-dimensional microstructural material characterization. part 1: Predictive models," *J. of Pow. Sour.*, vol. 282, pp. 552–561, 2015.

[44] B. Stier, B. Bednarcyk, J.-W. Simon, and S. Reese, "Investigation of micro-scale architectural effects on damage of composites," *NASA Technical Memorandum*, vol. NASA/TM—2015-218740, 05 2015.

[45] H. Moussaddy, D. Therriault, and M. Lévesque, "Assessment of existing and introduction of a new and robust efficient definition of the representative volume element," *Int. J. of Sol. and Struct.*, vol. 50, no. 24, pp. 3817–3828, 2013.

[46] Y. W. Kwon, "Revisiting Failure of Brittle Materials," *J. of Press. Ves. Tech.*, vol. 143, no. 6, 05 2021.

[47] Y. W. Kwon and S. DeFisher, "New failure criteria for composite materials and structures," in *Proc. of the Amer. Soc. for Comp. Thirty-Seventh Tech. Conf.*, 2022.

[48] Y. W. Kwon, "Failure prediction of notched composites using multiscale approach," *Poly.*, vol. 14, no. 12, p. 2481, 2022.

[49] E. Ashkenazi, "Problems of the anisotropy of strength," *Poly. Mech.*, vol. 1, no. 2, pp. 60–70, 1965.

[50] H. G. Franklin, "Classic theories of failure of anisotropic materials," *Fib. Sci. and Tech.*, vol. 1, no. 2, pp. 137–150, 1968.

[51] S. W. Tsai and N. J. Pagano, "Invariant properties of composite materials," Air Force Materials Lab Wright-Patterson AFB, Tech. Rep., 1968.

[52] I. Gol'denblat and V. Kopnov, "Strength of glass-reinforced plastics in the complex stress state," *Poly. Mechs.*, vol. 1, no. 2, pp. 54–59, 1965.

[53] M. A. Meyers and K. K. Chawla, *Mechanical Behavior of Materials*. Cambridge university press, 2008.

[54] T. H. Courtney, *Mechanical Behavior of Materials*. Waveland Press, 2005.

[55] C.-T. Sun and Z. Jin, *Fracture Mechanics*. Academic press, 2011.

[56] C. E. Inglis, "Stresses in a plate due to the presence of cracks and sharp corners," *Tran. Inst. Nav. Arch.*, vol. 55, pp. 219–241, 1913.

[57] A. A. Griffith, "Vi. the phenomena of rupture and flow in solids," *Phil. Tran. of the Roy. Soc. of Lon. Series A, Cont. Papers of a Math. or Phys. Char.*, vol. 221, no. 582-593, pp. 163–198, 1921.

[58] G. R. Irwin, "Analysis of stresses and strains near the end of a crack traversing a plate," 1957.

[59] D. S. Dugdale, "Yielding of steel sheets containing slits," *J. of the Mech. and Phy. of Sol.*, vol. 8, no. 2, pp. 100–104, 1960.

[60] G. I. Barenblatt, "The mathematical theory of equilibrium cracks in brittle fracture," *Adv.in App. Mech.*, vol. 7, pp. 55–129, 1962.

[61] F. Shang, Y. Yan, and J. Yang, "Recent advances in cohesive zone modelling of fracture," *Int. J. Aero. Aerosp. Eng.*, vol. 1, pp. 19–26, 2019.

[62] M. Elices, G. Guinea, J. Gomez, and J. Planas, "The cohesive zone model: Advantages, limitations and challenges," *Engin. Frac. Mech.*, vol. 69, no. 2, pp. 137–163, 2002.

[63] J. T. Wang, "Relating cohesive zone model to linear elastic fracture mechanics," Tech. Rep., 2010.

[64] K. Park and G. H. Paulino, "Cohesive zone models: a critical review of traction-separation relationships across fracture surfaces," *App. Mech. Rev.*, vol. 64, no. 6, p. 060802, 2011.

[65] E. T. Bowman and L. Susmel, "The theory of critical distances to model the short- to long-crack transition in geological materials subjected to mode i static loading," *Proc. Mat. Sci.*, vol. 3, pp. 562–567, 2014.

[66] D. Morgan, S. Quinlan, and D. Taylor, "Using the theory of critical distances to predict notch effects in fibre composites," *Theo. and App. Frac. Mech.*, vol. 118, p. 103285, 2022.

[67] D. Taylor, "The theory of critical distances applied to the prediction of brittle fracture in metallic materials," *Struc. Dur. & Hea. Mon.*, vol. 1, no. 2, p. 145, 2005.

[68] D. Taylor, "Applications of the theory of critical distances to the prediction of brittle fracture in metals and non-metals," in *15th European Conference of Fracture-ECF15, Stockholm*. Citeseer, 2004.

[69] D. Taylor, "The theory of critical distances applied to multiscale toughening mechanisms," *Eng. Frac. Mechs.*, vol. 209, pp. 392–403, 2019.

[70] D. Taylor, P. Cornetti, and N. Pugno, "The fracture mechanics of finite crack extension," *Eng. Frac. Mech.*, vol. 72, no. 7, pp. 1021–1038, 2005.

[71] D. Taylor, "Chapter 3 - the theory of critical distances in detail," in *The Theory of Critical Distances*, D. Taylor, Ed. Oxford: Elsevier Sci. Ltd, 2007, pp. 33–49.

[72] Y. Kwon and C. Panick, "Strain rate dependent failure criteria for fibrous composites using multiscale approach," *Multisc. and Multidis. Model., Exper. and Des.*, vol. 3, no. 1, pp. 11–22, 2020.

[73] A. Ugural and S. Fenster, *Advanced Strength and Applied Elasticity*, 4th ed. Upper Saddle River, NJ, USA: Prentice Hall, 2003.

[74] A. Durelli and W. Riley, "Stress distribution on the boundary of a circular hole in a large plate during passage of a stress pulse of long duration," 1961.

[75] V. I. Andreev and N. Y. Cybin, "The inhomogeneous plate with a hole: Kirsch's problem," *Proc. Eng.*, vol. 91, pp. 26–31, 2014.

[76] J. Hennig, "Anisotropy and structure in uniaxially stretched amorphous high polymers," in *J. of Poly. Sci. Part C: Poly. Symp.*, no. 5. Wiley Online Library, 1967, vol. 16, pp. 2751–2761.

[77] I. Ward, "Optical and mechanical anisotropy in crystalline polymers," *Proc. of the Phys. Soc.*, vol. 80, no. 5, p. 1176, 1962.

[78] N. Zohdi and R. Yang, "Material anisotropy in additively manufactured polymers and polymer composites: a review," *Poly.*, vol. 13, no. 19, p. 3368, 2021.

[79] B. L. Karihaloo, H. Abdalla, and Q. Xiao, "Size effect in concrete beams," *Eng. Frac. Mech.*, vol. 70, no. 7-8, pp. 979–993, 2003.

[80] B. L. Karihaloo, I. Milne, and R. Ritchie, *Comprehensive Structural Integrity: 10 Volume Set*. Elsevier, 2003, vol. 1.

[81] ASTM, "D638-10: Standard test method for tensile properties of plastics." American Society for Testing and Materials, 2010.

[82] D. Roylance, "Introduction to fracture mechanics," 2001.

[83] E. Rezvani Ghomi, F. Khosravi, A. Saedi Ardahaei, Y. Dai, R. E. Neisiany, F. Foroughi, M. Wu, O. Das, and S. Ramakrishna, "The life cycle assessment for polylactic acid (pla) to make it a low-carbon material," *Poly.*, vol. 13, no. 11, p. 1854, 2021.

[84] E. T. Vink, K. R. Rabago, D. A. Glassner, and P. R. Gruber, "Applications of life cycle assessment to natureworks™ polylactide (pla) production," *Poly. Deg. and Stab.*, vol. 80, no. 3, pp. 403–419, 2003.

[85] S. Muniyasamy, O. Ofosu, M. J. John, and R. D. Anandjiwala, "Mineralization of poly (lactic acid)(pla), poly (3-hydroxybutyrate-co-valerate)(phbv) and pla/phbv blend in compost and soil environments," *J. of Ren. Mat.*, vol. 4, no. 2, p. 133, 2016.

[86] Y. Liao, C. Liu, B. Coppola, G. Barra, L. Di Maio, L. Incarnato, and K. Lafdi, "Effect of porosity and crystallinity on 3d printed pla properties," *Poly.*, vol. 11, no. 9, p. 1487, 2019.

[87] S. Gradinaru, D. Tabaras, D. Gheorghe, D. Gheorghita, R. Zamfir, M. Vasilescu, M. Dobrescu, G. Grigorescu, and I. Cristescu, "Analysis of the anisotropy for 3d printed pla parts usable in medicine," *UPB Sci. Bul.*, vol. 81, 2019.

[88] H. Agu, A. Hameed, G. J. Appleby-Thomas, and D. Wood, "The dynamic response of dense 3 dimensionally printed polylactic acid," *J. of Dyn. Behav. of Mat.*, vol. 5, pp. 377–386, 2019.

[89] J. Slapnik, R. Bobovnik, M. Mešl, and S. Bolka, "Modified polylactide filaments for 3d printing with improved mechanical properties," *Cont. Mat.*, vol. 7, no. 2, pp. 142–150, 2016.

[90] N. Likittanaprasong, M. Seadan, and S. Suttiruengwong, "Impact property enhancement of poly (lactic acid) with different flexible copolymers," in *IOP Conference Series: Materials Science and Engineering*, no. 1. IOP Publishing, 2015, vol. 87, p. 012069.

[91] J. Kiendl and C. Gao, "Controlling toughness and strength of fdm 3d-printed pla components through the raster layup," *Comp. Prt B: Eng.*, vol. 180, p. 107562, 2020.

[92] G. E. C. Schmeier, C. Tröger, Y. W. Kwon, and D. Sachau, "Predicting failure of additively manufactured specimens with holes," *Mat.*, vol. 16, no. 6, p. 2293, 2023.

[93] N. Parker, M. Mather, S. Morgan, and M. Povey, "Longitudinal acoustic properties of poly (lactic acid) and poly (lactic-co-glycolic acid)," *Bio. Mat.*, vol. 5, no. 5, p. 055004, 2010.

[94] D. Ma, R. Gao, M. Li, and J. Qiu, "Mechanical and medical imaging properties of 3d-printed materials as tissue equivalent materials," *J. of App. Clin. Med. Phy.*, vol. 23, no. 2, p. e13495, 2022.

[95] Y. Kwon, A. Gonzalez, and S. DeFisher, "Failure of specimens with holes subjected to remote or inserted pin loading," *Awaiting publication in ASME J. of App. Mech.*, 2023.

[96] M. R. Khosravani, S. Rezaei, H. Ruan, and T. Reinicke, "Fracture behavior of anisotropic 3d-printed parts: Experiments and numerical simulations," *J. of Mat. Res. and Tech.*, vol. 19, pp. 1260–1270, 2022.

[97] M. M. Hanon, R. Marczis, and L. Zsidai, "Influence of the 3d printing process settings on tensile strength of pla and ht-pla," *Period. Polytec. Mech. Eng*, vol. 65, no. 1, pp. 38–46, 2021.

[98] *ABAQUS/Standard User's Manual, Version 2022*. United States: Dassault Systèmes Simulia Corp, 2022.

[99] Y. Kwon and M. Park, "Versatile micromechanics model for multiscale analysis of composite structures," *App. Comp. Mat.*, vol. 20, no. 4, pp. 673–692, 2013.

[100] S. Nemat-Nasser, "Introduction to high strain rate testing," in *ASM Handbook, Volume 8: Mechanical Testing and Evaluation*. ASM International, 2000. Available: https://app.knovel.com/hotlink/khtml/id:kt007ONKF1/asm-handbook-volume-08/introduction-high-strain

[101] D. Dattelbaum and J. Coe, "The dynamic loading response of carbon-fiber-filled polymer composites," in *Dynamic Deformation Damage and Fracture in Composite Materials and Structures*, V. Silberschmidt, Ed. Boston, MA, USA: Woodhead Publishing, 2016, pp. 225–275.

[102] I. W. Hall, A. Taşdemirci, and A. Kara, "Off-axis properties of cross-ply metal matrix composites at quasi-static and high strain rates," *Proc. Eng.*, 2011.

[103] R. Ochola, K. Marcus, G. Nurick, and T. Franz, "Mechanical behaviour of glass and carbon fibre reinforced composites at varying strain rates," *Comp. Struc.*, vol. 63, no. 3-4, pp. 455–467, 2004.

[104] V. Singh, "Literature survey of strain rate effects on composites," *TR18-001 (open), Swerea (now RISE) SICOMP, Mölndal, Sweden*, 2018.

[105] G. C. Jacob, J. M. Starbuck, J. F. Fellers, S. Simunovic, and R. G. Boeman, "Strain rate effects on the mechanical properties of polymer composite materials," *J. of App. Poly. Sci.*, vol. 94, no. 1, pp. 296–301, 2004.

[106] S. V. Thiruppukuzhi and C. Sun, "Models for the strain-rate-dependent behavior of polymer composites," *Comp. Sci. and Tech.*, vol. 61, no. 1, pp. 1–12, 2001.

[107] O. Okoli and G. Smith, "Failure modes of fibre reinforced composites: The effects of strain rate and fibre content," *J. of Mat. Sci.*, vol. 33, no. 22, pp. 5415–5422, 1998.

[108] O. I. Okoli, "The effects of strain rate and failure modes on the failure energy of fibre reinforced composites," *Comp. Struc.*, vol. 54, no. 2-3, pp. 299–303, 2001.

[109] R. Sierakowski, "Strain rate effects in composites," 1997.

[110] G. Gray III and W. R. Blumenthal, "Split-hopkinson pressure bar testing of soft materials," *ASM handbook*, vol. 8, pp. 488–496, 2000.

[111] W. W. Chen and B. Song, *Split Hopkinson (Kolsky) Bar: Design, Testing and Applications*. Springer Sci. & Business Media, 2010.

[112] B. A. Gama, S. L. Lopatnikov, and J. W. Gillespie Jr, "Hopkinson bar experimental technique: a critical review," *Appl. Mech. Rev.*, vol. 57, no. 4, pp. 223–250, 2004.

[113] U. Lindholm and L. Yeakley, "High strain-rate testing: Tension and compression: In this paper, the authors present a split-pressure-bar method for obtaining complete stress-strain curves at strain rates in the order of 1000 sec- 1 in either tension or compression," *Exp. Mech.*, vol. 8, no. 1, pp. 1–9, 1968.

[114] M. Pankow, C. Attard, and A. Waas, "Specimen size and shape effect in split hopkinson pressure bar testing," *The J. of Str. Anal. for Engin. Des.*, vol. 44, no. 8, pp. 689–698, 2009.

[115] D. J. Frew, M. J. Forrestal, and W. Chen, "Pulse shaping techniques for testing brittle materials with a split hopkinson pressure bar," *Exp. Mech.*, vol. 42, pp. 93–106, 2002.

[116] Y. Lu and Q. Li, "Appraisal of pulse-shaping technique in split hopkinson pressure bar tests for brittle materials," *Int. J. of Prot. Struc.*, vol. 1, no. 3, pp. 363–390, 2010.

[117] R. Naghdabadi, M. J. Ashrafi, and J. Arghavani, "Experimental and numerical investigation of pulse-shaped split hopkinson pressure bar test," *Mat. Sci. and Engin.*, vol. 539, pp. 285–293, 2012.

[118] O. Sen, S. Tekalur, and P. Maity, "On the use of non-cylindrical specimens in a split-hopkinson pressure bar," *The J. of Str. Anal. for Eng. Des.*, vol. 46, no. 8, pp. 866–878, 2011.

[119] D. Gao, Z. Bao, W. Han, X. Wang, S. Huang, L. Huang, Q. Chen, H. Zhao, and Y. Xu, "Effect of strain rate on tensile properties of carbon fiber-reinforced epoxy laminates with different stacking sequences and ply orientations," *Poly.*, vol. 15, no. 12, p. 2711, 2023.

[120] T. Schmack, T. Filipe, G. Deinzer, C. Kassapoglou, and F. Walther, "Experimental and numerical investigation of the strain rate-dependent compression behaviour of a carbon-epoxy structure," *Comp. Struc.*, vol. 189, pp. 256–262, 2018.

[121] E. Lee, M. Finger, and W. Collins, "Jwl equation of state coefficients for high explosives," Lawrence Livermore National Lab.(LLNL), Livermore, CA (United States), Tech. Rep., 1973.

[122] O. T. Strand, L. V. Berzins, D. R. Goosman, W. W. Kuhlow, P. D. Sargis, and T. L. Whitworth, "Velocimetry using heterodyne techniques," in *26th International Congress on High-Speed Photography and Photonics*. SPIE, 2005, vol. 5580, pp. 593–599.

[123] D. Dolan, "Extreme measurements with photonic doppler velocimetry (pdv)," *Rev. of Sci. Instr.*, vol. 91, no. 5, 2020.

[124] B. Jilek, "History of velocimetry technology," 2012.

[125] P. Mercier, J. Benier, A. Azzolina, J. Lagrange, and D. Partouche, "Photonic doppler velocimetry in shock physics experiments," in *J. de Phys. IV (Proc.)*. EDP sciences, 2006, vol. 134, pp. 805–812.

[126] W. Walters and J. Zukas, *Fundamentals of Shaped Charges*. New York, NY, USA: John Wiley Sons, 1989.

THIS PAGE INTENTIONALLY LEFT BLANK

Initial Distribution List

1. Defense Technical Information Center
   Ft. Belvoir, Virginia

2. Dudley Knox Library
   Naval Postgraduate School
   Monterey, California

3. Picatinny Arsenal Technical Library
   Picatinny Arsenal, New Jersey



DUDLEY KNOX LIBRARY

NAVAL POSTGRADUATE SCHOOL

WWW.NPS.EDU

WHERE SCIENCE MEETS THE ART OF WARFARE